

Southern Illinois University Carbondale

OpenSIUC

Dissertations

Theses and Dissertations

8-1-2024

NEW ELECTROCHEMICAL PLATFORMS FOR THE DETECTION OF NEURODEGENERATIVE DISEASE BIOMARKERS

Omair Adil

Southern Illinois University Carbondale, omairadilchem@gmail.com

Follow this and additional works at: <https://opensiuc.lib.siu.edu/dissertations>

Recommended Citation

Adil, Omair, "NEW ELECTROCHEMICAL PLATFORMS FOR THE DETECTION OF NEURODEGENERATIVE DISEASE BIOMARKERS" (2024). *Dissertations*. 2232.

<https://opensiuc.lib.siu.edu/dissertations/2232>

This Open Access Dissertation is brought to you for free and open access by the Theses and Dissertations at OpenSIUC. It has been accepted for inclusion in Dissertations by an authorized administrator of OpenSIUC. For more information, please contact opensiuc@lib.siu.edu.

NEW ELECTROCHEMICAL PLATFORMS FOR THE DETECTION OF
NEURODEGENERATIVE DISEASE BIOMARKERS

by

Omar Adil

M.Sc., Federal Urdu University of Arts, Sciences and Technology, Karachi, Pakistan, 2010
M.S., National University of Science and Technology, Islamabad, Pakistan, 2017

A Dissertation

Submitted in Partial Fulfillment of the Requirements for the
Doctor of Philosophy Degree

School of Chemical and Biomolecular Sciences
in the Graduate School
Southern Illinois University Carbondale
May 2024

Copyright by Omair Adil, 2024
All Rights Reserved

DISSERTATION APPROVAL

NEW ELECTROCHEMICAL PLATFORMS FOR THE DETECTION OF
NEURODEGENERATIVE DISEASE BIOMARKERS

by

Omair Adil

A Dissertation Submitted in Partial

Fulfillment of the Requirements

for the Degree of

Doctor of Philosophy

in the field of Chemistry

Approved by:

Dr. Mohtashim H. Shamsi, Chair

Dr. Gary R. Kinsel

Dr. Lichang Wang

Dr. Divya Prakash

Dr. Poopalasingam Sivakumar

Graduate School
Southern Illinois University Carbondale
March 28, 2024

AN ABSTRACT OF THE DISSERTATION OF

Omar Adil, for the Doctor of Philosophy degree in Chemistry, presented on March 28, 2024, at Southern Illinois University Carbondale.

TITLE: NEW ELECTROCHEMICAL PLATFORMS FOR THE DETECTION OF NEURODEGENERATIVE DISEASE BIOMARKERS

MAJOR PROFESSOR: Dr. Mohtashim Hassan Shamsi

Neurodegenerative disease (ND) is a collection of progressive disorders which is marked by gradual degeneration of the central nervous system (CNS). The damage of brain and nervous system causes diminishing of brain and nerve cell which lead to body dysfunction, organ failure, paralysis and ultimately death of a patient. Neurodegenerative diseases affect more than 50 million people worldwide. United States of America is among highest ND prevailing disease countries. Yet the number of cases is underreported because of the complexity of disease diagnosis. With the increase in aging population the rate of ND cases is also increasing. Another important concern is that viral pandemic like COVID-19 may additionally contribute to rise in ND affected population. Currently there is no cure available for ND except a few treatments which decrease some symptoms and decrease disease progression. Early-stage diagnosis of ND is therefore an important and immediate area of research which can improve the quality of life of affected people and help in health management.

Many ND has been associated with abnormal expansion of tandem repeat sequence of nucleic acid and other associated protein biomarkers. The discovery of these biomarkers holds promise for improving diagnosis, treatment, and efficacy monitoring. Current detection methods such as neuroimaging techniques, Real-Time quantitative Polymerase Chain Reaction (RT-qPCR) and Enzyme-Linked Immunosorbent Assay (ELISA) are complex, expensive, require laboratory setup and/or trained operator. Electrochemical biosensing offers a promising portable, inexpensive, and sensitive platform for early stage diagnosis and healthcare management.

In this dissertation a label free electrochemical method is developed to investigate the effect of complex targets for potential genosensing applications and effect of complex biomatrix for immunosensing applications.

We first prepare sensing surfaces with three different backbone microprobe nucleic acids to detect length- and sequence-dependent complex secondary structures containing RNA linked to Huntington's disease, based on the charge transfer resistance of the interface. Then we reported an immunosensing surface using commercially available screen-printed electrode to detect ALS associated biomarker neurofilament light chain in serum samples. Finally, we establish an in-house and cost effective electrochemical immunosensing platform for the detection of ALS biomarker poly-glycine-proline dipeptide repeat in cerebrospinal fluid.

ACKNOWLEDGEMENTS

I am deeply grateful to Almighty Allah for granting me the strength and blessing to reach this significant milestone in my life. My heartfelt appreciation goes to my advisor, Dr. Mohtashim Shamsi, whose unwavering support and guidance were instrumental throughout my PhD journey. His invaluable technical insights and assistance played a pivotal role in the completion of my dissertation. I am also indebted to my dissertation committee members, Dr. Gary R. Kinsel, Dr. Lichang Wang, Dr. Divya Prakash, and Dr. Poopalasingam Sivakumar, for their guidance and support throughout my doctoral program. Special thanks to former committee members Dr. Ian I. Suni, Dr. Keith T. Gagnon, and Dr. Farhan Chowdhury for their valuable contributions.

My heartfelt thanks extend to all the teachers who imparted their knowledge and expertise during my PhD coursework. I am particularly thankful to Dr. Qingfeng Ge, the chair of the department of chemistry, and my collaborators, Dr. Poopalasingam Sivakumar, and Seth B. Eddington, for their contributions to my journey. I am grateful to Dr. Keith Gagnon for his invaluable advice and discussions. Special thanks to staff members Brandon Luster, Chris Kraft and Deborah Sawyer for their help in my graduate assistantship.

I am also grateful to my colleagues who supported me along the way, including Dr. Hannah Giang, Dr. Narges Asefifeyzabadi, Prabhangshu Kumer Das, Mohammad Asad, Mahmudun Noby, Avoke Onorimuo, Hannah Hubbard, Will Almy, and my undergraduate mentees Comfort Adeyeye, Ryan Wang, Moez Alam, Nezar Abunnur, and Mariah Harned. I extend my sincere appreciation to my friends Dr. Ahmad Z. Qamar, Dr. Zaheer Masood, Zahid Siraj, Abdulbasit Tobi Gafar, Ishani M. Senanayake, Awais Ayub, Adeel Zia, and Dr. Ain Uddin for their assistance and encouragement.

I am thankful to the department of chemistry and biochemistry at SIUC for providing graduate assistantships and supporting me during my PhD program. I also acknowledge the Gower research fellowship for their support during the summers. I am grateful to the people of Carbondale, there are many wonderful individuals here, without them the journey would be difficult. Lastly, I extend my gratitude to SIUC for their support through scholarships, which facilitated my research endeavors.

DEDICATION

I dedicate this dissertation to my late mother, Amna, whose dream I am living and fulfilling through this work.

To my sister Warda.

To my wife Ayesha and my daughter Sarah.

To my father, Dilshad Adil, and my siblings, Naushad, Faraz, Fahad, Sehreen, and sister-in-law, Anum.

To all my teachers, including my PhD research advisor, Dr. Mohtashim Hassan Shamsi, MS research advisor, Dr. Habib Nasir, and undergraduate research advisor, Dr. Iftikhar Ahmad Tahiri.

TABLE OF CONTENTS

<u>CHAPTER</u>	<u>PAGE</u>
ABSTRACT.....	i
ACKNOWLEDGMENTS	iii
DEDICATION.....	iv
LIST OF TABLES.....	vi
LIST OF SCHEMES.....	vii
LIST OF FIGURES	vii
CHAPTERS	
CHAPTER 1 – Introduction.....	1
CHAPTER 2 – Microprobes for Label-Free Detection of Short Tandem Repeats: An Insight on Alleviating Secondary Structure Effects.....	20
CHAPTER 3 – Electrochemical Impedance Immunoassay for ALS-Associated Neurofilament Protein: Matrix Effect on the Immunoplatfrom.....	43
CHAPTER 4 – Electrografted Laser Induced Graphene: Sensitive Detection of Neurodegenerative Disease Biomarker in Cerebrospinal Fluid.....	56
CHAPTER 5 – Conclusion.....	78
REFERENCES	82
APPENDICES	
APPENDIX A – Figure Permissions for Chapter 1.....	118
VITA	129

LIST OF TABLES

<u>TABLE</u>	<u>PAGE</u>
Table 1.1 - ND disorders and their link to normal sequence length and pathogenic gene length mutation	12
Table 1.2 - Biomarkers present in different biological matrix and their link with different NDs	13
Table 2.1 - RNA target and control sequences with potential binding sites and flanking regions. CAG and CUG complementary sites are italicized and highlighted	24
Table 2.2 - CAG repeat RNA information and simulated sequence structures based on their lowest free energy ΔG	28
Table 3.1 - Charge transfer resistance (R_{CT} signals) of ALS serum samples and the concentration of Nf-L obtained in serum-based and PBS buffer-based calibration ...	53
Table 4.1 - Real ALS patients sample information with sample ID, gender, age range at the time of death, EIS signal and polyGP concentration calculated.....	76

LIST OF SCHEMES

<u>SCHEMES</u>	<u>PAGE</u>
Scheme 2.1 - General illustration of DNA, PNA, and LNA nucleotide. Depicting microprobe platforms comprised DNA, PNA, and LNA backbones.....	21
Scheme 3.1 - Depicting step by step preparation of the electrochemical immunosensing platform on rGO screen-printed electrodes and the detection of ALS	46
Scheme 4.1 - A single step formation of LIG by rastering CO ₂ laser over Polyimide film. A vinyl passive film was pasted.....	58

LIST OF FIGURES

<u>FIGURE</u>	<u>PAGE</u>
Figure 1.1 - General diagram of process and physical elements of biosensor.....	1
Figure 1.2 - Different types of biosensors and their transducing methods	3
Figure 1.3 - Nix hydration biosensor is based on electrical impedance spectroscopy is a wearable biosensor which determines the ionic potential of the sweat	4
Figure 1.4 - Basic process and elements of electrochemical biosensing	6
Figure 1.5 - Input waveforms and put signals of different electrochemical techniques	7
Figure 1.6 - An amperometric wearable biosensor FreeStyle Libre by Abbott	10
Figure 1.7 - Some known factors causing neurodegenerative disease	11
Figure 1.8 - G4C2 repeat expansion that causes loss of C9ORF72 function	15
Figure 1.9 - Elements of EIS representing electrode, transducer surface	19
Figure 2.1 - PCR products resolved on an agarose gel after PCR amplification	25
Figure 2.2 - CAG17-152 and CAG68-306 RNA products resolved by denaturing	26
Figure 2.3 - Positive control CAG17-158(PC), Specificity control CUG17-158(SC)	27
Figure 2.4 - Representative Nyquist form of impedance plots and bar graphs	31
Figure 2.5 - Representative Nyquist form of EIS plots of the targets at concentration	33
Figure 2.6 - Box and whisker plots comparing the R_{CT} of the targets containing 17	34
Figure 2.7 - Box and whisker plots comparing the R_{CT} of the targets	35
Figure 2.8 - Representative Nyquist form of EIS plots comparing the target	36
Figure 2.9 - Box and whisker plots comparing the performances of the PNA	38
Figure 2.10 - Representative Nyquist form of EIS plots comparing the target	39
Figure 2.11 - Representative Nyquist form of EIS plots comparing the control	40
Figure 2.12 - Box and whisker plots comparing the performances of the PNA	41
Figure 3.1 - EIS plots for biolayer formation including unmodified rGO surface	49
Figure 3.2 - EIS signals of the synthetic Nf-L target captured at the immunoplatform	51
Figure 3.3 - Correlation plot between R_{CT} of synthetic Nf-L targets in commercial	52

Figure 3.4 - Plot of target Nf-L concentration in ALS serum samples	54
Figure 4.1 - Optical images of the LIG electrodes made at different combinations	64
Figure 4.2 - Electrochemical performance of prepared LIG electrode	66
Figure 4.3 - Electrografting of LIG and SPE b) CV response of E-LIG and E-SPE	67
Figure 4.4 - Comparison of LIG before and after electrografting. a) FTIR-ATR	68
Figure 4.5 - SEM micrographs of SPE before and after electrografting	69
Figure 4.6 - Response of biorecognition layer formation on E-LIG surface	70
Figure 4.7 - Modified Randle equivalent circuit to fit experimentally determined	71
Figure 4.8 - Response of biorecognition layer formation on E-SPE surface	71
Figure 4.9 - Synthetic polyGP target in buffer medium was prepared at different	72
Figure 4.10 - Selectivity of synthetic polyGP target in PBS buffer at 1 ng/mL	74
Figure 4.11 - EIS response of polyGP target in undiluted commercial CSF	75

CHAPTER 1

INTRODUCTION

1.0. Biosensors

Biosensing is an interdisciplinary field which is defined by IUPAC gold book¹⁵ as “A device that uses specific biochemical reactions mediated by isolated enzymes, immunosystems, tissues, organelles or whole cells to detect chemical compounds usually by electrical, thermal or optical signals.” The device includes biosensing elements, a transducer, and a signal readout unit. A biosensing element is a bioreceptor that is immobilized on the sensing surface to selectively capture the target analyte in biological samples.¹⁶ A transducer is used to convert (bio)chemical signal, resulting from the interaction between the analyte and bioreceptor, into visual, optical, or electrical signal as shown in **Figure 1.1**.

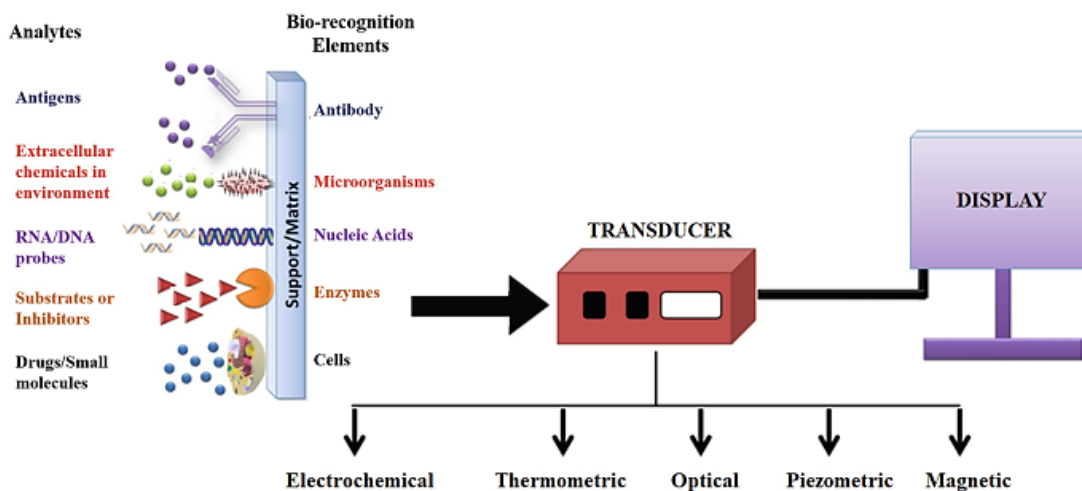


Figure 1.1. General diagram of process and physical elements of biosensor.⁷ Adopted from 103 with the permission from Springer Nature.

On the basis of signal transduction and biorecognition elements, biosensors are placed in different categories.¹⁷ According to transduction elements biosensors can be classified as optical, magnetic, thermal, or electrochemical sensors. Biosensors are also classified according to

biorecognition elements such as immunosensor, genosensor, aptasensor and enzymatic or nonenzymatic biosensor. The basis of bioreceptor and transduction further classifies the sensor into affinity-based biosensor or catalytic biosensor.¹⁸ In affinity biosensor, binding affinity is responsible to associate bioreceptors (antibody, nucleic acid, aptamer etc.) with analyte (nucleic acid, antigen, cells etc.).¹⁹ While catalytic biosensor involves an enzyme labeled probe with biorecognition element or surface, that involves conversion of either analyte, or a substrate present in the solution into a signaling product for signal transduction. Sometime biosensor uses a label to generate and/or to amplify signal.²⁰ Because some biomolecules or organic analytes are difficult to detect, labeling the biorecognition elements using fluorescence, or radioactive markers has been used. The label detection strategy may involve a biorecognition element as capture probe and a label element as detection probe. On the other hand, more recently due to the emergence of sensitive techniques, label free detection techniques are increasingly reported.^{21, 22} Label free detection strategy involves binding of analyte with biorecognition element which brings physical change on the sensing surface such as resistance, optical quenching, resonance frequency and plasmon resonance (**Figure 1.2.**).

1.1. Significance of biosensors

Biosensors are used in applications such as disease diagnosis and monitoring, drug metabolite and efficacy monitoring, pollutants detection and monitoring, disease causing virus, microorganisms and biomarkers detection in different media including human, plants, animals and environment.^{23, 24} Specifically in medical diagnosis of human beings, biosensors show great potential as they can be cost effective, user friendly, and miniaturized devices.^{25, 26}

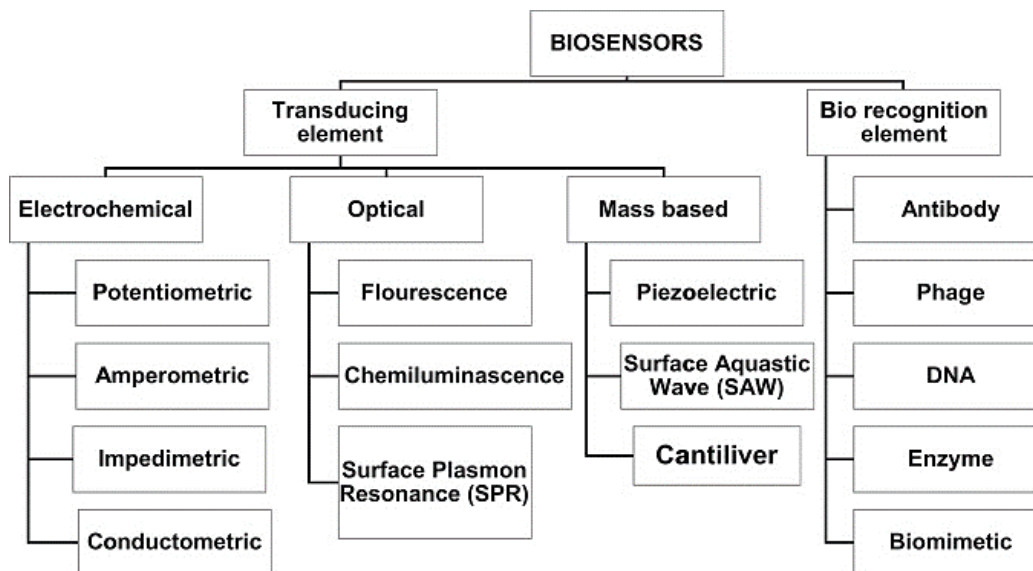


Figure 1.2. Different types of biosensors and their transducing methods.³
Adapted from 6 with the permission from Talanta.

With the advancement in computer, bio and nano technology, biosensors research area has also shown improved performance to meet commercial purposes including selectivity, sensitivity, shelf life and antifouling capability.^{27, 28} Additionally with the potential use of artificial intelligence, internet of things, cloud-based computing and electronic medical records in the healthcare industry are also the driving factor in growth of biosensor research.^{29, 30} Furthermore, the demand for biosensors is increasing due to high demand of compact and economical diagnostic and point of care devices.^{31, 32} Wearable biosensors also promise continuous health monitoring for better health management.³³ The COVID-19 pandemic emphasized the usefulness of self-testing through biosensor development which gave rise to the medical device industry.³⁴ There are well over 500 companies worldwide presently working in the field of biosensors and bioelectronics. The biosensors market was valued at \$25.5 billion in 2021 and is expected to increase to USD 36.7 billion by 2026.²⁵

1.2. Electrochemical Biosensors

In electrochemical biosensors detection observed by the use of electrodes modified with a biorecognition element.³⁵ The biorecognition element specifically binds target analyte and physical, chemical, or biological changes is converted into electrochemical measurement which is recorded before and after introduction of target analyte.³⁶ **Figure 1.3** shows elements and basic function of electrochemical biosensor.

Electrochemical biosensing involves a redox active species which undergoes an electron transfer reaction at the sensing surface.³⁷ Many target analytes are redox active species; however for non-electroactive species either the surface is decorated with enzymes for catalytic reaction, or another electroactive redox species is used to observe the signal.^{38, 39} (**Figure 1.4 c & d**). In broader perspective, electrochemical biosensors can be categorized into catalytic and affinity biosensors (**Figure 1.4 a & b**).

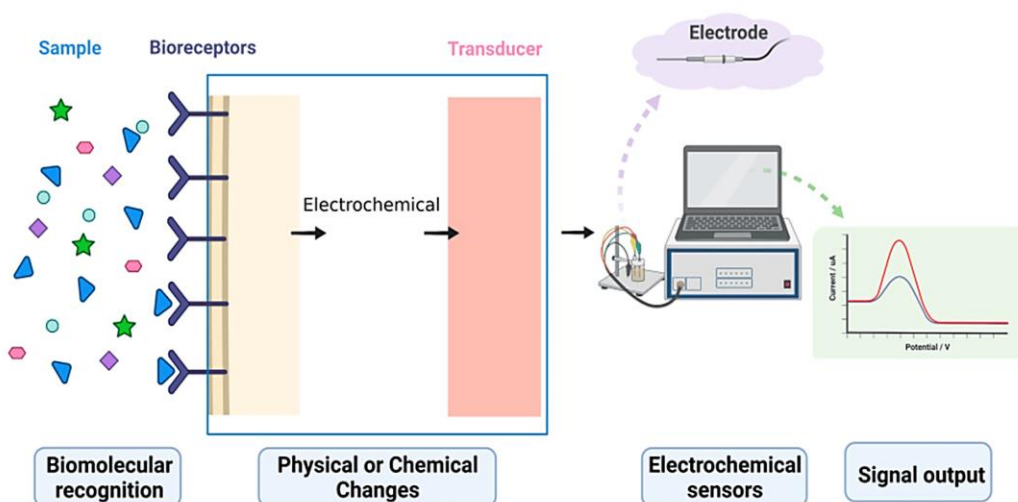


Figure 1.3. Basic process and elements of electrochemical biosensing.²
Adapted from 2 with the Creative Commons Attribution (CC BY 4.0 DEED) from Biosensors.

Catalytic biosensors are further classified into enzymatic and nonenzymatic biosensors. In enzymatic biosensing, the electrode surface is modified with target specific enzyme which not only captures the target but also converts the target products into redox active species.⁴⁰ Nonenzymatic biosensors utilize catalytic properties of nanomaterial to convert targets into electroactive species.⁴¹ Unfortunately, catalytic biosensors fall into poor stability and repeatability which therefore limit their utility in real applications. Affinity biosensing involves the affinity of a biorecognition element to selectively capture analyte to form stable complex.⁴² A redox active species observes the surface change after the complex formation and yields an electrochemical signal. The high specificity and reproducibility of affinity biosensors has promising application in biosensing. Affinity biosensors can be subcategorized into labeled and label free biosensors (**Figure 1.4 e & f**). Labelled biosensors use labels such as fluorescence and redox tagged with biorecognition or signaling element usually to enhance sensitivity of target detection.^{43, 44} However, use of label involves time consuming molecular tagging, surface preparation and/or complex detection mechanism. Furthermore, labeling can negatively impact analyte-receptor interaction. Therefore, biosensors that avoid labels are gaining popularity due to their simplicity and effective detection of analyte.^{45, 46} With the development in biotechnology more different and efficient label free biosensors are emerging.

On the basis of biorecognition element or bioreceptor, biosensors are classified as immunosensors, genosensors and aptasensors.⁴⁷ Immuosensors involve use of antibody or its fragments while genosensors involve nucleic acids as bioreceptor. Aptamers are referred to nucleic acids or peptides that specifically bind to target analytes.⁴⁸ More recently molecularly imprinted polymer has emerged which uses target specific cavity to capture analyte.⁴⁹

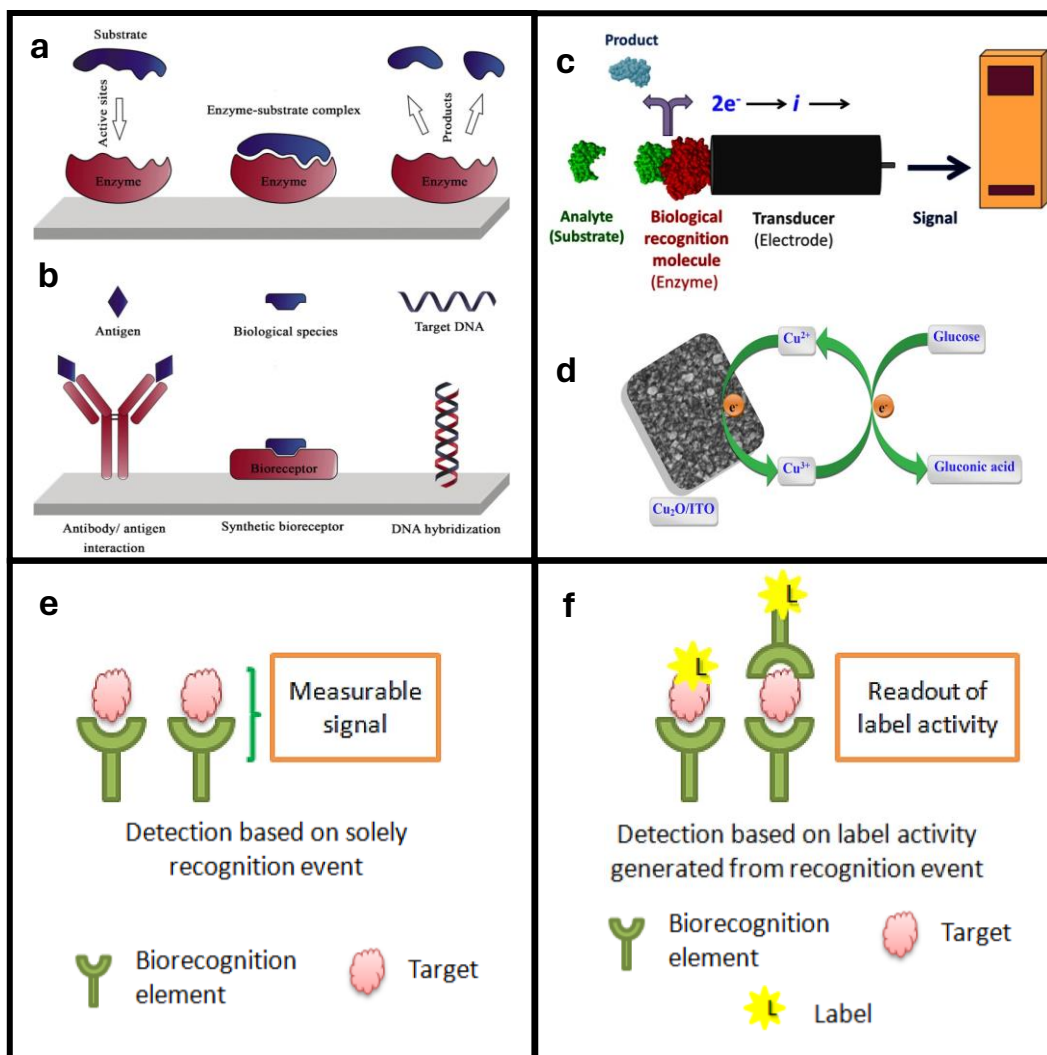


Figure 1.4. Electrochemical biosensors of different types. **a)** Catalytic biosensor **b)** Affinity biosensor⁴ **c)** Enzymatic biosensor¹⁰ **d)** Nonenzymatic biosensor¹³ **e)** Label free biosensor¹⁴ and **e)** Labeled biosensor. Adapted from 6 with the permission from Microchimica Acta, adapted from 4812 with the Creative Commons Attribution (CC BY 3.0 DEED) from Sensors, adapted from 6 with the permission from Applied Physics A and adapted from 2 with the Creative Commons Attribution (CC BY 4.0 DEED) from Sensors.

Electrochemical setup usually involves an electrochemical cell which contains three (working, reference, and counter) electrodes placed in electrolyte solution containing electrochemical redox active species. Electrochemical biosensors are used to detect analytes using a variety of techniques such as voltammetry, amperometry, coulometry and

electrochemical impedance spectroscopy etc.⁵⁰⁻⁵² In voltammetry technique a voltage is applied with respect to reference electrode and current response of chemical in electrochemical cell is measured. Some of the commonly used voltammetric techniques are linear scan voltammetry (LSV), cyclic voltammetry (CV), differential pulsed voltammetry (DPV) and square wave voltammetry (SWV). The different waveforms of these techniques are given in **figure 1.5**.⁸

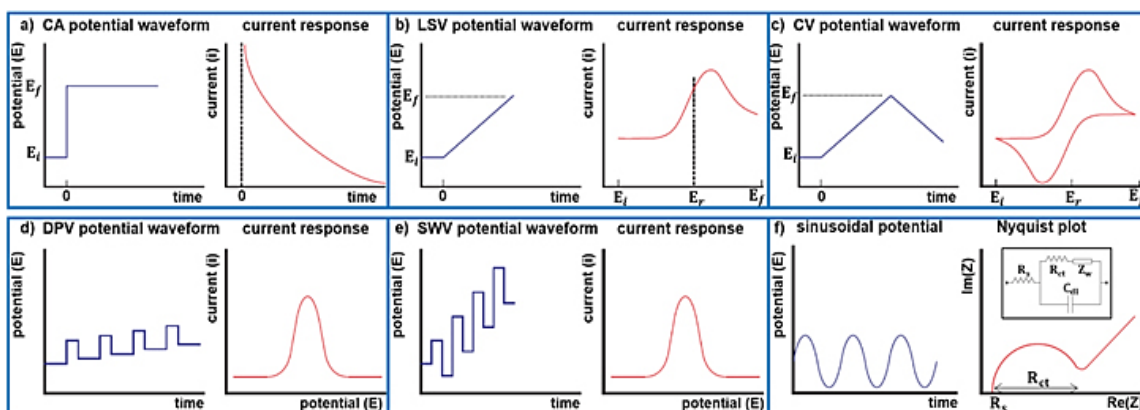


Figure 1.5. Input waveforms and put signals of different electrochemical techniques **a)** Chronoamperometry (CA) **b)** Linear scan voltammetry (LSV) **c)** Cyclic voltammetry (CV) **d)** Differential pulse voltammetry (DPV) **e)** Square wave voltammetry (SWV) and **f)** Electrochemical impedance spectroscopy (EIS).⁸ Adapted from 167 with the Creative Commons Attribution (CC BY 4.0 DEED) from Journal of The Electrochemical Society.

The graph obtained from the result of voltammetry experiment is called voltammogram. In a LSV experiment the potential between working and reference electrodes is swept linearly with time and the current response is measured. The current response peaks at specific response potential representing oxidation or reduction of chemical species. In cyclic voltammetry experiment voltage is swept between working and reference electrode to a given value and then reverse in the opposite direction. A plot of response current from both forward and reverse sweep is obtained as a function of applied voltage. Different input parameters are used in CV

experiments to extract many useful information such as voltage range or potential window, number of potential cycles and scan rate.⁵³

CV is one of the most widely used electrochemical techniques due to simplicity, sensitivity, speed, and its wide range applicability in wide range biosensing applications. In differential pulse voltammetry, a pulse of fixed amplitude is superimposed on a step potential and the current is sampled before and at the end of the pulse. Since in DPV the charging current is separated by the background therefore low limit of detection can be achieved useful for biosensing application.⁵⁴ Square Wave voltammetry is emerging as a more powerful electrochemical technique in biosensing application.⁵⁵ It applies superimposed staircase wave with square wave and net current signal is obtained by the difference between the forward and reverse current at each sampling point as a result better signal to noise ratio is achieved. SWV shows similar sensitivities as DPV however has advantage of faster detection.

Amperometry is an important technique in the development of biosensors. The first amperometric biosensor was developed in 1956 to measure dissolved oxygen in blood.⁵⁶ In amperometry a constant voltage is applied, and response current is measured as a function of time. An important advantage of using amperometry is that the response current is proportional to the concentration of analyte and therefore used in quantitative biosensing measurement.

Electrochemical Impedance Spectroscopy (EIS) is an important and rapidly emerging electrochemical technique because unlike other electrochemical techniques EIS is a steady state technique which use small signal analysis and probes signal relaxation over a very wide range of applied voltage frequency.⁵⁷ Due to the small perturbation of signal, it is considered a more suitable and sensitive technique for biosensing analysis.

Due to the potential of user-friendly point of care device formation, electrochemical devices are emerging in the market. Some of the commercially available devices are given in **figure 1.6**. The FreeStyle Libre sensor from Abbott is a wearable continuous glucose monitoring device which was recently approved by FDA. The biosensor is an enzymatic amperometric 3-electrode sensor system. Glucose from interstitial fluid (ISF) diffuses into polymer matrix which contains osmium complex mediator and glucose oxidase enzyme which oxidizes the glucose. The resulting electrochemical signal is then transduced and converted into readable signal. Another electrochemical biosensor has been introduced in the market for point of care diagnostic of Lactate and Hemoglobin/Hematocrit is StatStrip LAC/Hb/Hct by Nova Biomedical. The biosensor is handheld easy-to-use device which measure lactate and Hemoglobin/Hematocrit separately from blood sampled on given test strips. The biosensor takes 0.6 to 1.6 μL of blood and provides lab-like accuracy in just 13 seconds. Accu-Chek Sensor by Roche is one of the famous handheld biosensors available in the market. The biosensor is based on amperometry that measures glucose from whole blood.

Compared to glucose biosensors which have dominated the biosensor market since last 50 years, electrochemical biosensors for other biomarkers have not reached their success in the commercial market as POC devices.^{58, 59} One of the main challenges to the market availability of these biosensors is the unavailability of a single or set of biomarkers that are specific to one type of disease. However, with the progress in proteomics and molecular biology research it will be possible to develop electrochemical biosensors for specific diseases.

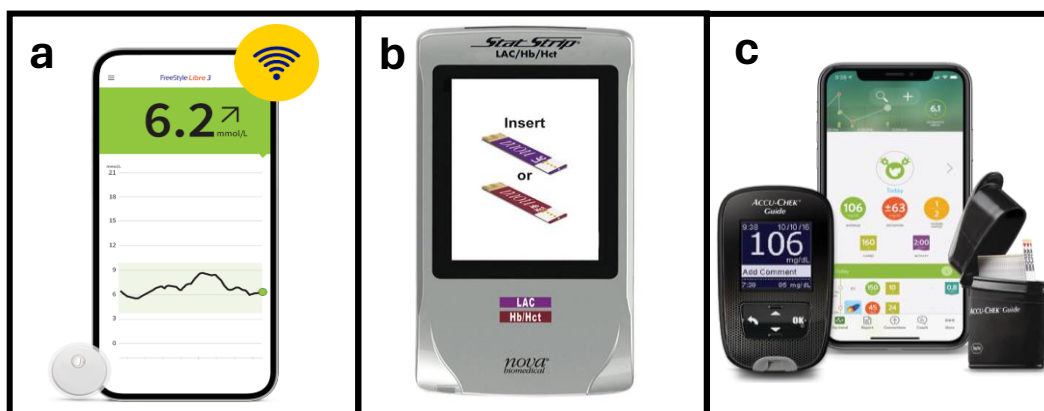


Figure 1.6. a) An amperometric wearable biosensor FreeStyle Libre by Abbott that monitor glucose from interstitial fluid is recently approved by FDA.⁶ b) StatStrip LAC/Hb/Hct by Nova Biomedical is an electrochemical biosensor which measure lactate and Hemoglobin/Hematocrit separately from blood sampled on given test strips.⁹ c) Accu-Chek Sensor by Roche is handheld electrochemical biosensor that measure blood glucose level using disposable test strips.¹² Adapted with the universal commons (CC0 1.0 Universal).

1.3. Neurodegenerative disease

Neurodegenerative disease (ND) causes brain and nervous system damage which results in dysfunction of the nervous system and death of nerve cells.⁶⁰ Currently no cure is available for neurodegenerative disease except a few treatments that relieve some symptoms and slow down their progression. There are more than 50 neurodegenerative diseases. Some of the common ND are Alzheimer disease (AD), Parkinson disease (PD), Amyotrophic Lateral Sclerosis (ALS), Huntington disease (HD), Frontotemporal Dementia (FTD) and Spinal Muscular Atrophy (SMA).⁶¹ Neurodegenerative disorders affect millions globally, with AD and PD are the most common causes. In United States, about 6.2 million and one million individuals may have AD and PD respectively.⁶² According to a study sampled 34% of world population, ALS cases are expected to grow from 80 thousand in 2015 to 105 thousand in 2040.^{63, 64} The study report that United States is among the highest ALS prevalence countries. For Huntington disease there are currently 41 thousand symptomatic Americans and more than 200 thousand may inherit the

disease, because every child has 50% chance of inheriting the HD mutated gene from affected parents.⁶⁵ Studies show that global prevalence of HD was 2.7 per 100 thousand persons in 2010 which increase to 4.88 per 100 thousand people.⁶⁶ The rise in the number of ND population is a matter of concern. Especially viral pandemic may potentially trigger the rise in the number of ND populations.⁶⁷

Neurodegenerative is caused by several factors including genetic factors, deposition of amyloid fibrils, exposure to reactive oxygen species (ROS) and metals (especially aluminum, copper and zinc), mitochondrial dysfunction and production of neurotoxin oligomers (**figure 1.7**).⁶⁸

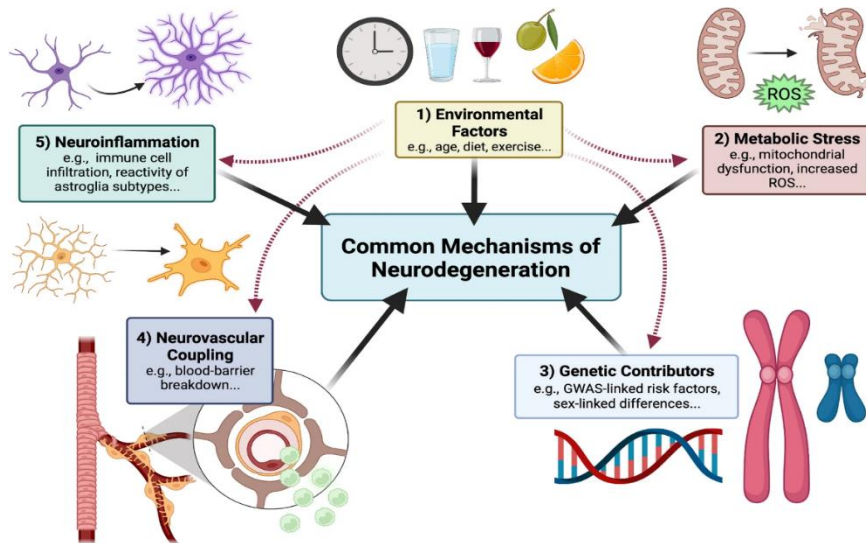


Figure 1.7. Some known factors causing neurodegenerative disease.¹ Adapted from 4 with the Creative Commons Attribution (CC BY 4.0 DEED) from Molecular Neurodegeneration.

For most of the ND, aging is considered as the main risk factor. Recent studies found that certain viruses including influenza virus and SARS-COV virus are linked to neurodegenerative diseases in the years following infection.⁶⁹ The findings indicate that the onset of certain neurodegenerative diseases could potentially be averted through the prevention of influenza and

other viral infections.⁷⁰ To improve the life quality of the ND population, different methods have been developed for diagnosis and treatment. The discovery of ND linked biomarkers not only promises to improve the diagnostic method but also exhibits potential in the development and monitoring of ND therapies.⁷¹ Many ND has been found to linked with abnormal expansion of tandem repeat sequences. Discovery of these genetic repeat sequence offers possibility of diagnosis and therapy of ND disease and therefore consider as biomarkers of the disease. **Table 1.1** shows the normal tandem repeat sequence and their pathogenic expansion linked to some common ND.⁷²

Table 1.1. ND disorders and their link to normal sequence length and pathogenic gene length mutation.

Disorder	Repeating units	Normal length	Pathogenic length	Reference
PD	ATTCT	10-32	280-4500	⁷³
C9ALS	GGGGCC	2-25	>25	⁷⁴
HD	CAG	10-35	>35	⁷⁵
C9FTD	GGGGCC	2-25	>25	⁷⁴
FXS	CGG	6-55	>200	⁷⁶
SBMA	CAG	9-36	38-62	⁷⁷
SCA1	CAG	6-35	49-88	⁷⁸
FRAXE	CCG	4-39	200-900	⁷⁹
FRDA	GAA	8-33	>90	⁸⁰
FXTAS	CGG	6-35	55-200	⁸¹

PD = Parkinson disease, C9FTD = C9ORF linked Fronto temporal Dementia, FXS = Fragile X syndrome, SBMA = spinal bulbar muscular atrophy, SCA1 = spinocerebellar ataxia 1, FRAXE = Fragile XE, FRDA = Friedreich ataxia, FXTAS = Fragile X-associated tremor

Biomarkers are important tools that help identify abnormal processes caused by ND dysfunctions. Biomarkers are seen as having` significant potential in predicting disease risk, facilitating early detection, and guiding the development of new treatments. ND population is increasing worldwide, and their early-stage diagnosis remains difficult. Therefore, the need of dependable and consistent biomarkers to diagnose these diseases is increasingly crucial. Advances in technology have empowered scientists to pinpoint biomarkers for various

neurodegenerative diseases. **Table 1.2** shows the biomarkers related to ND and their presence in biomatrix. These biomarkers can be classified as invasive and noninvasive due to their sampling in different biological areas. Invasive samples include Cerebrospinal fluid (CSF), whole blood, serum or plasma, brain or neuron cells.⁸² Noninvasive samples include urine, sweat, tear and saliva etc.⁸³⁻⁸⁶ Although sampling of CSF is highly invasive, testing of CSF might be useful as biomarkers arising from the central nervous system (CNS) are found in higher concentrations in cerebrospinal fluid (CSF) and at much lower levels in the blood.⁸⁷ On the other hand, noninvasive sampling such as urine is easy to sample however urine may not provide as high concentration and informative biomarker profile due to its anatomical distance from the central nervous system (CNS).

Table 1.2. Biomarkers present in different biological matrix and their link with different NDs.			
Biomarker	Medium	Associated disease	Reference
SOD1	blood	ALS,	88
NfH, NfM, NfL	CSF, blood plasma and serum	All NDs	89
A β 42	CSF, blood plasma,	AD	90, 91
PolyGP, PolyGR, PolyGA, PolyPA, PolyPR	CSF, PBMC	ALS, FTD	92
CHI3L1/YKL40	CSF	All NDs	93
pTau181	CSF, blood plasma and serum	AD	94
IL-6 TNF- α	CSF, blood	All NDs	95, 96
HTT	blood	HD	97
mHTT	CSF, blood	HD	98, 99
pTau:tTau	CSF	ALS	100
YKL40	CSF	ALS	93
GFAP	CSF, blood plasma	MS, FTD	101, 102
Neurogranin	CSF	AD	103
α -synuclein	CSF, blood plasma and serum	PD	104
VCP = Valosin-Containing Protein, TDP-43 = Transactive response DNA-binding Protein 43, SOD1 = Superoxidase Dismutase 1, FUS = Fused in Sarcoma, HTT = Huntingtin, NfH, Neurofilament High chain, NfM = Neurofilament Medium chain, NfL = Neurofilament Light chain, A β = Amyloid- β peptides, PolyGP = Poly Glycine Proline, PolyGA = Poly Glycine Alanine, PolyGR = Poly Glycine Arginine, PolyPA = Poly Proline Alanine, PolyPR = Poly Proline Arginine, PBMC = Peripheral Blood Mononuclear Cells, TNF α = Tumor Necrosis Factor alpha, CHI3L1/YKL40 = Chitinase 3 Like 1, GFAP = Glial Fibrillary Acidic Protein, MS = Multiple Sclerosis, pTau:tTau = ratio of phosphorylated to total tau; YKL-39, chitinase-3-like protein 2, mHTT = mutant Huntingtin			

ALS and HD are also diseases of concern because of the projected increase in the number of cases in United states and worldwide. ALS was first reported by Charcot and Joffroy in 1869.¹⁰⁵ It is characterized by degeneration of motor neurons in the brain and spinal cord which cause muscular atrophy and paralysis. The disease is incurable and lead to death within 5 years of onset. Almost 50% familial cases, and 20% sporadic ALS and Fronto- Temporal Dementia (FTD) cases arise from GGGGCC hexanucleotide expansions in the Open Reading Framework gene 72 localized in Chromosome 9 (C9ORF72). C9ORF72 related ALS, discovered in 2011, can be observed by different biomarkers including clinical, neuroimaging and circulating biomarkers in serum and CSF.¹⁰⁶ G4C2 repeat expansion in the C9ORF72 gene is the most common genetic cause of ALS called c9ALS. Pathogenic repeat expansion of G4C2 results in loss of C9ORF72 function and gain in toxic function which form sense and antisense RNA transcripts of the expanded repeats (**Figure 1.8**). These RNA transcripts are then used in the production of five different dipeptide repeats (DPRs) including poly Glycine-Alanine (poly-GA), poly Glycine-Arginine (poly-GR), poly Proline-Alanine (poly-PA), poly Proline-Arginine (poly-PR) and poly Glycine-Proline (poly-GP). PolyGP is considered an important pharmacodynamic biomarker for c9ALS as it is present in C9orf72 expansion carriers and absent in noncarriers. Its concentration in cerebrospinal fluids and in peripheral blood mononuclear cells was found almost same in both symptomatic and asymptomatic c9ALS patients.^{107, 108} Other ALS associated biomarkers found in both CSF and in blood are neurofilaments (Neurofilament Heavy Chain (Nf-H), Neurofilament medium Chain (Nf-M), Neurofilament light Chain (Nf-L)).

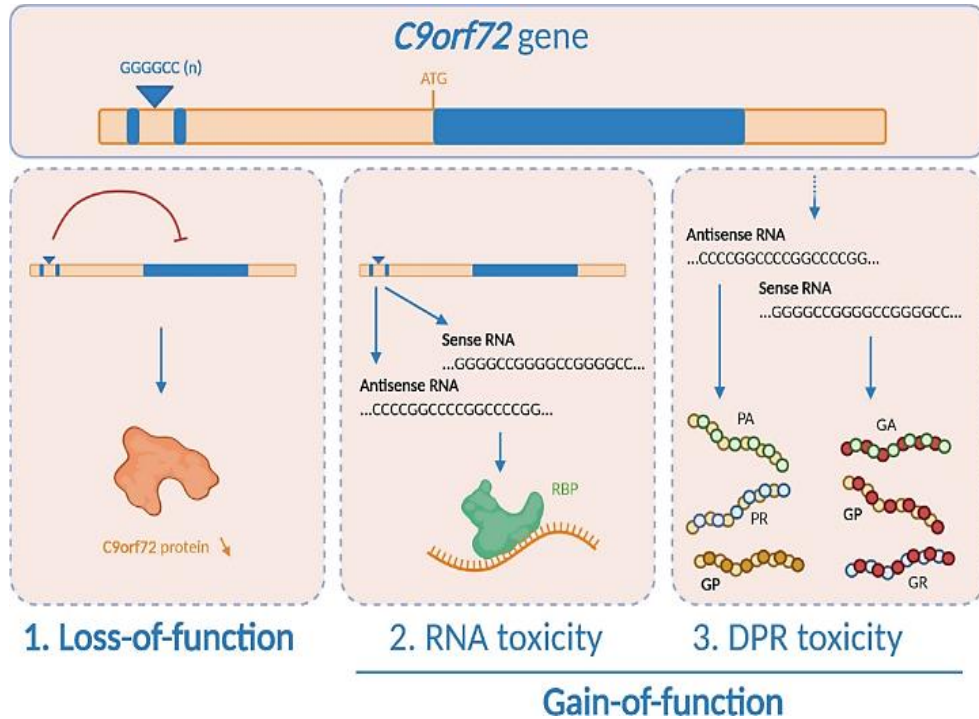


Figure 1.8. G4C2 repeat expansion that causes loss of C9ORF72 function and gain of abnormal function that form sense and antisense RNA transcripts of the expanded repeats which serves as a template for the synthesis of proteins of five different dipeptide repeats (DPRs).⁵ Adopted from Creative Commons Attribution (CC DEED) from Acta Neuropathologica.

Huntington's disease (HD) is a ND which affects the CNS. It is determined by involuntary choreatic movements, as well as behavioral and psychiatric disturbances, often leading to dementia.¹⁰⁹ In 1872 George Huntington identified symptoms and provide early description of what is now recognized as HD.¹¹⁰ HD typically emerges in adulthood and symptoms appear between 30-50 years of age. However, in case of Juvenile Huntington's disease (JHD) the symptoms can appear even before the age of 20.

Patients with HD may show cognitive decline and psychiatric symptoms. The disease arises from the mutation in a protein gene called huntingtin (Htt) which was discovered in 1993.¹¹¹ This mutation is autosomal inherited mutation i.e., CAG repeats present in chromosome 4p16.3 in the Huntingtin gene exceed 36 or more repeats. This mutation causes expanded stretch

of the amino acid glutamine within huntingtin protein and lead to abnormal interaction with other cell proteins and therefore cause functional changes.¹¹² The length of CAG repeat can correlate with the age of disease onset. The longer the repeats, the earlier will be the disease onset. Other biomarkers of HD have been emerging these includes neurotransmitters upregulation (dopamine, serotonin) and downregulation (GABA, acetylcholine).¹¹³

ALS diagnoses rely on methods including Electrophysiological, neuroimaging, neuropathological and muscle biopsy studies. For the detection of ALS biomarkers, many methods have been reported which include immunoassay,¹¹⁴ microarray analysis,¹¹⁵ RNA-sequencing,¹¹⁶ Real-Time quantitative Polymerase Chain Reaction (RT-qPCR),¹¹⁷ Enzyme-Linked Immunosorbent Assay (ELISA),¹¹⁸ Magnetic Resonance Imaging (MRI),^{119, 120} Positron Emission Tomography (PET),¹²¹ Total reflection X-Ray Fluorescence (TXRF),¹²² fluorescence microscopy,¹²³ fluorescence spectroscopy,¹²⁴ microfluidics¹²⁵ and electrochemical analysis.¹²⁶⁻¹²⁹

The challenges linked to ALS and Huntington and other NDs are their early detection, treatment and therapeutic monitoring.¹³⁰ Until now there has been no cure for these diseases. However, the discovery of their biomarkers offers the possibility of developing methods for early-stage diagnosis and treatment. Currently both ALS and HD are clinically assessed by signs and symptoms and cognitive measurement, correlation with familial cases and confirmed through DNA testing.¹³¹ Until now, clinically no imaging, general blood tests or other diagnostic tools are helpful and therefore required multiple testing before conclusion.¹⁰⁹ The conventional clinical diagnostics methods are expensive and require instruments in laboratory with trained personnel. Some of the methods require delicate procedures and the patients suffer painful experiences. The availability of these instruments is also a challenge, especially in far-flung areas and lower- and middle-income countries.¹³²

1.4. Challenges in real sample detection

Electrochemical biosensors have several advantages over other analytical techniques as they have potential in the development of point of care (POC) devices because of their high sensitivity, low detection limit, high specificity with accuracy. Compared to other lab-oriented methods electrochemical methods promise cost effective, portable, user-friendly, and onsite operating capabilities. The method usually requires small sample volumes in microliter range. Moreover, they can be integrated into wearable devices and interfaced with digital readout tools like smartphones. Rapid analysis of real samples makes them a valuable option for developing commercial electrochemical detection methods. These attributes present a promising platform for early and reliable diagnosis and healthcare management.

Despite the promising features of electrochemical method to develop practically feasible biosensors, yet these sensors often encounter challenges due to matrix effect present in clinical samples and it's uncommon to find biosensors that maintain their promising performance when applied to actual clinical samples.¹³³ Achieving the lowest limit of detection under pristine laboratory conditions doesn't guarantee success when dealing with real clinical samples.¹³⁴ Matrix molecules present in these samples can interact with analytes, raising questions about whether the sensitivity observed in a clean environment can be maintained. In some cases, especially with mass or size-sensitive sensors, the sensitivity may increase due to analyte binding with matrix molecules.¹³⁵ For instance, in the detection of antibodies in serum, albumin readily binds to the constant fragment of antibodies, potentially enhancing sensitivity.

Furthermore, matrix molecules can interact with the sensor surface, leading to nonspecific adsorption and alterations in sensor response, often resulting in drift.¹³⁶ In electrochemical sensors, this nonspecific adsorption can limit access to the sensor surface,

reducing sensitivity and detection thresholds. Strategies to mitigate nonspecific adsorption, such as surface antifouling, are crucial for enhancing sensor performance.¹³⁷ Additionally, in biological matrix environments, biorecognition elements may exhibit different selectivity compared to controlled conditions, potentially leading to cross-reactivity and nonspecific interactions. Assessing interference at concentrations typical of biological matrices is critical for ensuring sensor specificity and precision.

1.5. Electrochemical Impedance spectroscopy (EIS)

Electrochemical Impedance Spectroscopy (EIS) is an emerging technique in the field of electrochemical (bio)sensing. The technique involves generation of electrochemical signal from the charge transfer resistance of redox chemical species or changes in capacitance at electrode solution interface. The change in charge transfer resistance or R_{CT} is caused by physical steric hindrance from biolayer on the surface and increment of analyte concentration captured by the biolayer (**Figure 1.9 a**). The more the transducer surface blocked by the biolayer more hindrance in the diffusion of redox active probe occur which cause increase in R_{CT} . Surface charge of the transducing surface can also cause electrostatic attraction or repulsion to the redox probe which alter the diffusion and therefore the R_{CT} values. The experiment of EIS involves AC potential sweeping from high frequency to low frequency overlapping on fixed DC potential as input signal. The output signal is a complex graph of imaginary impedance as a function of real impedance typically called Nyquist form of EIS plot (**Figure 1.9b**). Bode plot is another form of EIS plot however Nyquist plot is used more frequently as it is easier to interpret and provide same information as Bode plot. The experimental data is simulated using so called modified Randle equivalent circuit to extract the circuit elements values including R_{CT} and capacitance (**Figure 1.9c**). Compared to other electrochemical techniques, EIS offers advantages, such as it's

a steady state technique which utilizes small signal analysis over a wide range of applied frequency. EIS offers label free detection as it exhibits signal change with high sensitivity toward the change in analyte concentration (**Figure 1.9d**). Utilizing antibody-antigen interaction-based platform is advantageous as it offers high specificity and low limit of detection and therefore can be utilized to build biosensing platform for several applications especially in bioanalysis fields.

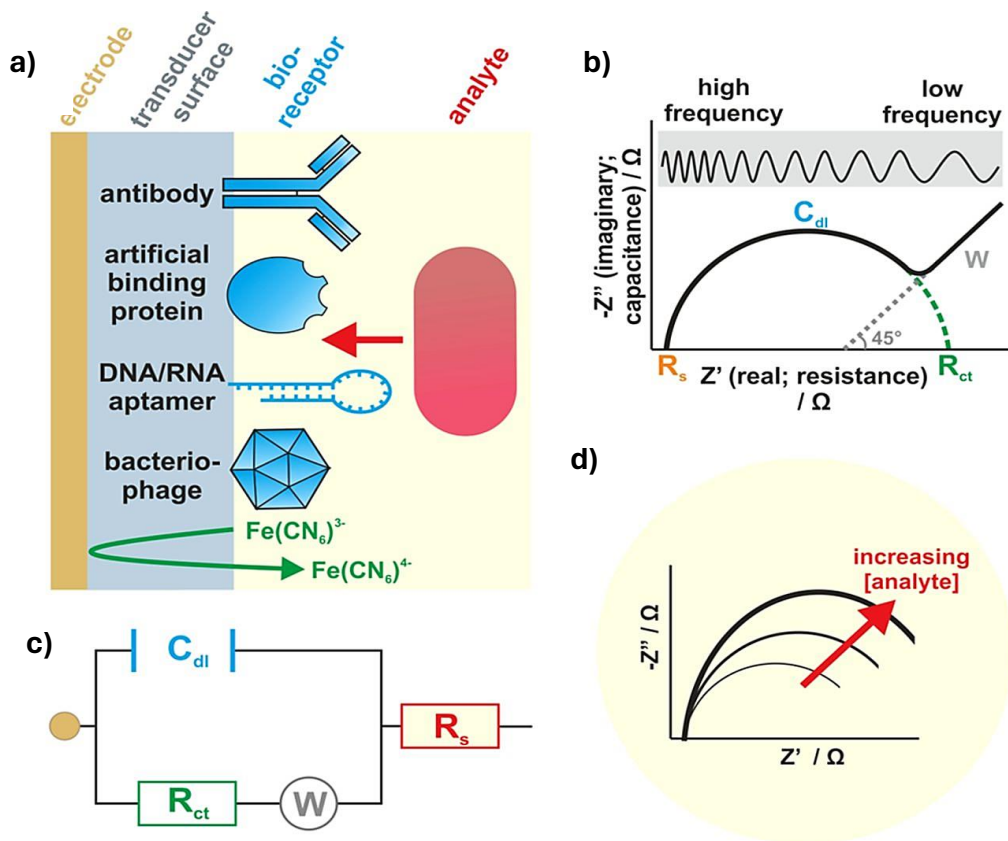


Figure 1.9. a) Elements of EIS representing electrode, transducer surface, biorecognition element and analyte. b) Input voltage wave and output signal as Nyquist form of EIS plot c) Randle equivalent circuit to fit and extract circuit element values from experimental data d) Change in signal response with analyte concentration.¹¹ Adapted from 638 with the permission from Clinical Microbiology Reviews.

Note: Part of this chapter has been published.^{138, 139}

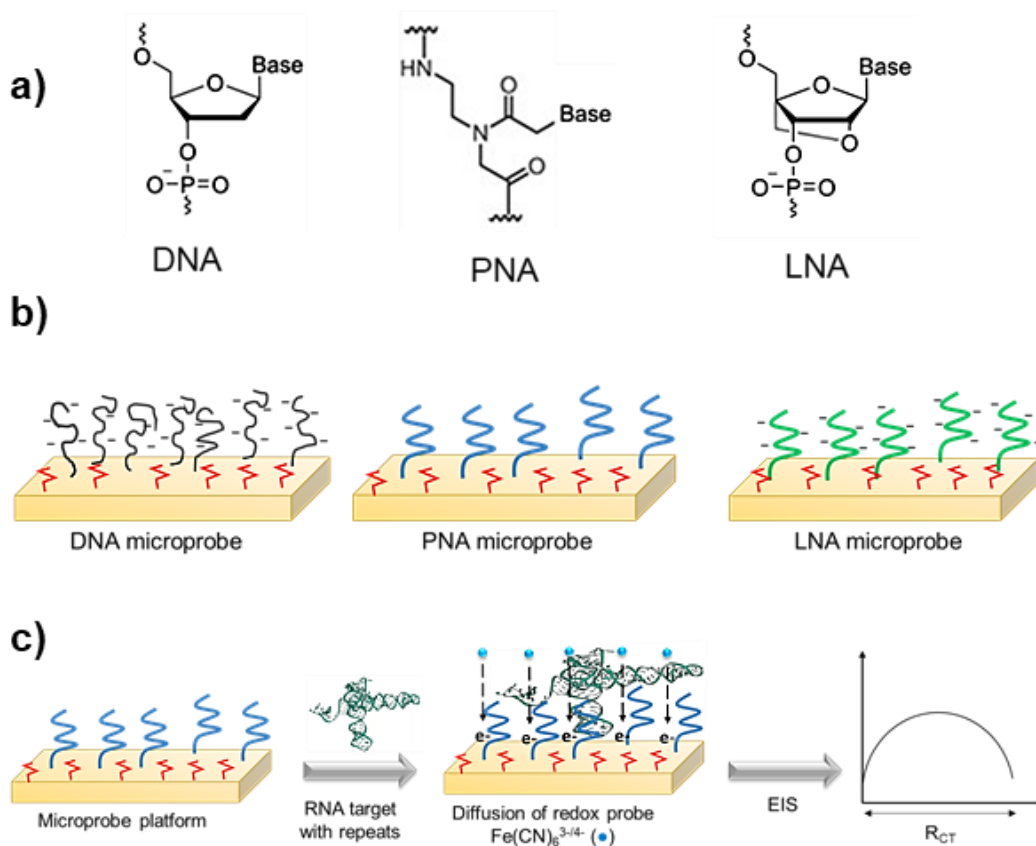
CHAPTER 2

MICROPROBES FOR LABEL-FREE DETECTION OF SHORT TANDEM REPEATS: AN INSIGHT ON ALLEVIATING SECONDARY STRUCTURE EFFECTS

2.0. Abstract

Overgrowth of short tandem repeat sequences in our genes can cause various neurodegenerative disorders. Such repeat sequences are ideal targets for label-free electrochemical detection of such potential expansions. However, their length- and sequence-dependent secondary structures may interfere with the interfacial charge transfer of a detection platform, making them complex targets. In addition, the gene contains sporadic repeats that may result in false-positive signals. Therefore, it is necessary to design a platform capable of mitigating these effects and ultimately enhancing the specificity of tandem repeats. Here, we analyzed three different backbones of nucleic acid microprobes [deoxyribonucleic acid, peptide nucleic acid, and lock-nucleic acid (LNA)] to detect *in vitro* transcribed RNA carrying CAG repeats, which are associated with Huntington's disease, based on the charge transfer resistance of the interface. We found that the LNA microprobe can distinguish lengths down to the attomolar concentration level and alleviate the effect of secondary structures and sporadic repeats in the sequence, thus distinguishing the "tandem repeats" specifically. Additionally, the control experiments conducted with and without Mg^{2+} demonstrated the LNA microprobe to perform better in the presence of the divalent cation. The results suggest that the LNA-based platform may eventually lead to development of a reliable and straightforward biosensor for genetic neurodegenerative disorders.

2.1. Introduction



Scheme 2.1. a) General illustration of a DNA, PNA, and LNA nucleotide. **b)** Depicting microprobe platforms comprised DNA, PNA, and LNA backbones where the microprobes are immobilized on a gold surface through $(\text{CH}_2)_6\text{-S}$ -linker and a mercaptahexanol layer blocks empty spaces around the probe. **c)** Illustration depicts the charge transfer resistance (R_{CT}) of the microprobe platform after capturing the RNA target with repeats using EIS in soluble redox probe $\text{Fe}(\text{CN})_6^{3-/4-}$.

Short tandem repeat expansions are length-dependent mutations in naturally occurring 2–10 nucleotide repeat combinations, leading to an increasing number of neurodegenerative disorders.¹⁴⁰ Electrochemical strategies have been widely applied to detect various genetic biomarkers due to their high sensitivity, miniaturizability, and potential integration with lab-on-a-chip platforms.^{141, 142} However, there have been limited efforts in developing electrochemical strategies to detect repeat biomarkers, and the proposed strategies depend on chemical labeling,

sample amplification, or detecting short target lengths.¹⁴³⁻¹⁵⁰ The concept of label-free electrochemical detection of lengthy repeat targets in cell-derived RNA was previously validated using deoxyribonucleic acid (DNA) and peptide nucleic acid (PNA) microprobes (<20-mer);^{151,}¹⁵² however, it has not been determined how the microprobes can alleviate the effect of sequence- and length-dependent secondary structures of the target, which limits development of a rapid, low-cost, and simple biosensor for repeat mutations.

Through interfacial impedance signaling of the microprobe platforms, we investigated here three backbones of nucleic acid microprobes [DNA, PNA, and lock-nucleic acid (LNA)] shown in **Scheme 2.1a** to answer this question. The targets were *in vitro* transcribed RNA containing CAG repeats, as presented in **Table 2.1**. These targets consist of 17 and 68 CAG repeat units, a 17 CUG repeat sequence, a “scrambled” sequence with the same CAG composition, and a nontargeting sequence derived from a GFP-encoding gene fragment. In addition, the target sequences possessed flanking regions on both ends derived from the naturally occurring exon 1 of the huntingtin (HTT) messenger RNA, contributing to the overall secondary structures of the RNA. Furthermore, these sequences have sequence- and length-dependent secondary structures and distinct free energy ΔG (**Table 2.2**). The detection strategy in this study involved the immobilization of an 18-mer microprobe containing six complementary CTG repeat units onto gold electrodes in conjunction with a blocking layer of 6-mercapto-hexanol (MCH), as depicted in **Scheme 2.1b**. The CTG repeats in the microprobe should form Watson–Crick base pairs with complementary CAG units in the RNA target. **Scheme 2.1c** depicts how such complex targets likely unzip at different locations in the presence of complementary microprobes, resulting in changes to the charge transfer resistance (R_{CT}) of the interface. The impedance signal

was compared to concentrations, lengths, nonspecific sequences, secondary structures, tandem vs. sporadic repeat, and divalent Mg^{2+} to evaluate the performance of the microprobes.

2.2. Experimental

2.2.1. Materials

The microprobe sequence with different backbones used for this study was 5'→3' HS- C_6H_{12} -CTG CTG CTG CTG CTG CTG. Synthetic PNA microprobe with hexane thiol modification at the 5'-end was purchased from PNA Bio (USA), while the DNA and LNA microprobes were procured from Integrated DNA Technologies (USA). All the nucleotides in the LNA microprobe were locked, i.e., the extra methylene group between 2'-O- and 4'-positions locks the ribofuranosyl-ring in its 3'-endoconformation. All RNA target and control sequences (**Table 2.1**) were synthesized via *in vitro* transcription from synthetic or PCR-generated DNA templates as described previously,¹⁵³ and below. Gold-coated silicon substrates with a 100-nm gold layer were obtained from Platypus (USA). ACS grade MCH, sulfuric acid (95%–98%), hydrogen peroxide solution (30 wt.%), ethylene diamine tetraacetic acid (EDTA) disodium salt, and molecular biology grade magnesium chloride solution (1.0 M) were purchased from Sigma-Aldrich. Molecular biology grade Tris buffer (1.0 M, pH 8) was purchased from EMD Millipore Corp. Sodium chloride (99.0%) was procured from Fisher Scientific. Potassium ferricyanide (>99%) and potassium ferrocyanide trihydrate (>99%) were purchased from Acros Organic, while phosphate-buffered saline (PBS) 10× was obtained from Sigma life science. Silver/silver chloride in 3 M potassium chloride reference electrode was purchased from Basi Inc. (USA), and platinum wire counter electrode was purchased from CH Instrument (TX, USA). All electrochemical measurements were performed using a Metrohm Autolab PGSTAT204 FRA32M (USA) electrochemical workstation within a Metrohm Autolab Faraday cage.

2.2.2. Synthesis and PCR amplification of RNA targets.

Plasmids containing 17 or 68 CAG repeats with upstream and downstream HTT gene flanking sequences were prepared following methods described previously.¹⁵⁴ The CAG repeats and flanking sequence were PCR-amplified with a forward primer incorporating a T7 promoter sequence (Htt rep up 3_T7; TAATACGACTCACTATAGGGATGGCGACCCTGGAAAAG) and a reverse primer (Htt rep dn; GGCTGAGGAAGCTGAGGAG). PCR was performed with Phusion Hi-Fidelity DNA Polymerase (Thermo Scientific) following the manufacturer's recommended protocol at 64 °C annealing temperature, 30 sec extension time, and 34 cycles. This product was gel-extracted and used in a second round of PCR as a template to reduce the occurrence of nonspecific products and increase yield. The size of the products was confirmed by running them on an agarose gel, with CAG17 being 176 base pairs and CAG68 being 342 base pairs in length (**figure 2.1**). The products were gel-extracted once more before T7 transcription to ensure purity.

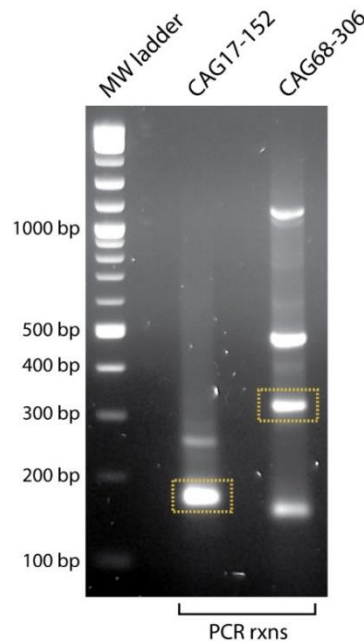


Figure 2.1. PCR products resolved on an agarose gel after PCR amplification from CAG repeat-containing plasmid. Indicated bands were gel extracted for *in vitro* transcription.

2.2.3. T7 Transcription of CAG Repeat Expansions

We prepared DNA templates for *in vitro* transcription via PCR amplification of plasmids containing the 5' end of the first exon of the *HTT* mRNA cloned from cells derived from Huntington's disease patients.¹⁵⁴ As described previously, T7 RNA polymerase was used to carry out *in vitro* transcription.¹⁵³ To remove the DNA template, reactions were incubated at 37 °C for 3 h and then treated with DNase I for 20 min at 37 °C. A final concentration of 20 mM EDTA was added to stop DNase I digestion. The transcribed RNA was extracted with phenol/chloroform, precipitated with ethanol, and resuspended in denaturing loading buffer (1× TBE, 90% formamide). The sample was incubated at 95 °C for 5 min, cooled, and gel-purified by resolving on a 10% denaturing urea-PAGE gel (**Figures 2.2 and 2.3**), as described previously.¹⁵³ The concentration of the purified RNA was calculated with an absorbance at 260 nm and a calculated extinction coefficient using Beer's Law. All synthetic DNA, RNA, LNA, and PNA sample solutions were prepared in 100 μM Tris-HCl buffer (pH 8.5) containing 200 mM sodium chloride and 20 mM magnesium chloride.

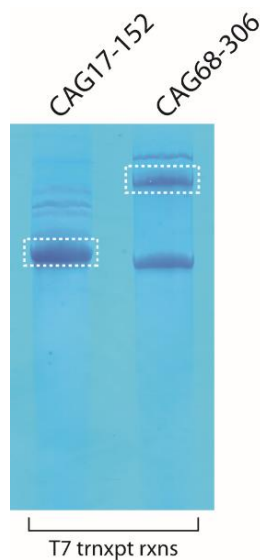


Figure 2.2. CAG17-152 and CAG68-306 RNA products resolved by denaturing urea-PAGE after *in vitro* transcription with T7 RNA polymerase. Indicated bands were cut out and gel-purified.

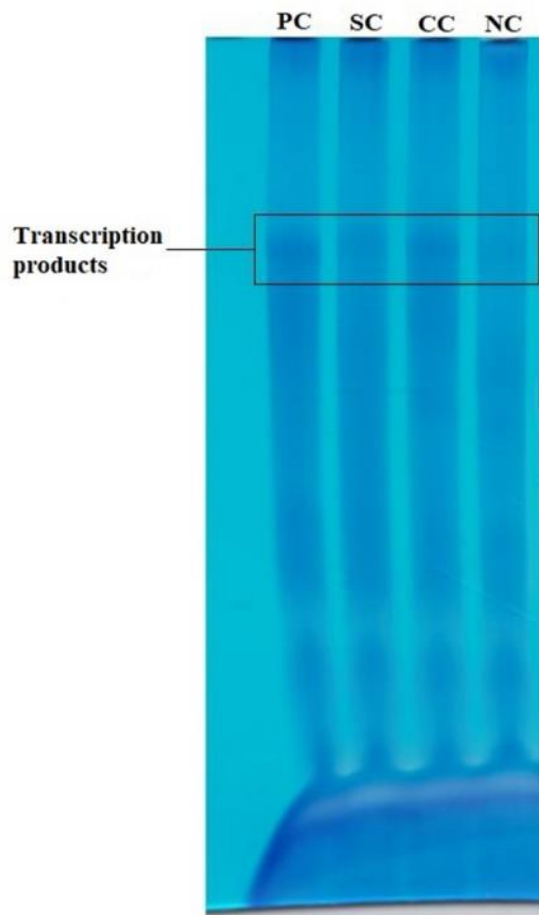
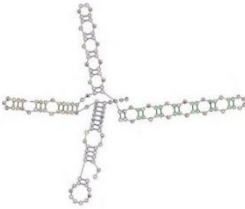
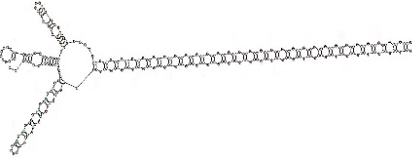
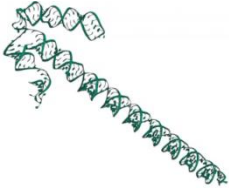
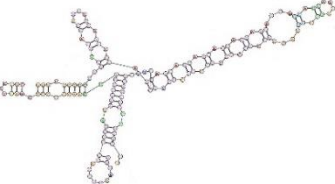
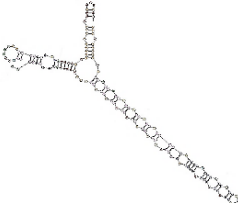
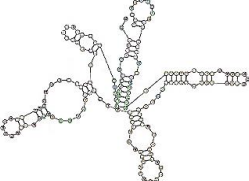
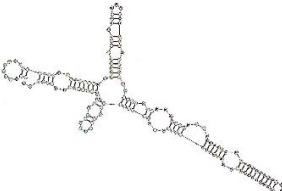


Figure 2.3. Positive control CAG17-158(PC), Specificity control CUG17-158(SC), Composition control CAG17-158(CC), and Non-target control GFP-158(NC) RNA products resolved by denaturing urea-PAGE after *in vitro* transcription with T7 RNA polymerase. Indicated bands were cut out and gel-purified.

2.2.4. RNA secondary structure prediction

The secondary structures of RNA listed in **Table 2.2** were obtained from open-source software of molecular modeling.^{155, 156} The parameters were kept at default, and secondary structures with the lowest free energy were used in this study.

Table 2.2. CAG repeat RNA information and simulated sequence structures based on their lowest free energy ΔG .

RNA Information	Secondary Structure	3D model
CAG17-152 %GC: 68.4 ΔG : -53.2 kcal/mol		
CAG68-306 %GC: 67.7 ΔG : -115.7 kcal/mol		
CAG17-158(PC) %GC: 67.7 ΔG : -52.6 kcal/mol		
CUG17-158(SC) %GC: 67.7 ΔG : -58.5 kcal/mol		
CAG17-158(CC) %GC: 67.7 ΔG : -49.1 kcal/mol		
GFP-158(NC) %GC: 67.1 ΔG : -65.7 kcal/mol		

Note: Although several secondary structures may exist for each of these sequences, we considered the structures with the highest stability indicated by their minimum free energy for the interpretation of results.

2.2.5. Preparation of a microprobe platform on gold electrodes

Gold electrodes (2 mm dia.) were prepared by cutting 1 cm² pieces from a 100-nm gold-coated silicon substrate. The small substrates were immersed for 10 s in acid piranha H₂SO₄:H₂O₂ (3:1) before being washed with DI water, 100 μM Tris buffer, and dried with N₂. On top of the gold substrate, a vinyl sheet with a 2-mm diameter circular hole was adhered to define the sensing electrode area. As described previously, the side edges and back of the substrate were coated with a resin to insulate the exposed silicon.¹⁵¹ By measuring the charge of a stripping peak in 0.5 M sulfuric acid obtained at ~0.9 V during a cyclic voltage sweep from 0 to 1.6 V at a scan rate of 0.5 V/s, the electroactive area of the gold electrode was determined. The measured electroactive area of individual electrodes was used to normalize the subsequent electrochemical measurements. Next, a 5-μL aliquot of 1 μM microprobe was applied to the gold electrode surface to form a surface-assembled film in a sealed humid container at 8 °C for 4 h. The modified electrodes were washed 3× with a wash buffer (100 μM Tris buffer without magnesium chloride and sodium chloride) and incubated for 30 min with 1 mM MCH solution to block any unmodified surface. Before being exposed to RNA targets, the DNA + MCH, PNA + MCH, and LNA + MCH-modified electrodes were washed 3× with the washing buffer and dried with nitrogen. The microprobe platform was incubated for 30 min at 8 °C with 5 μL of these sequences for surface hybridization with the target and control sequences. To conduct measurements without Mg²⁺, the platforms were washed 3× with 20 mM EDTA in 100 μM Tris buffer.

2.2.6. Detection of repeats

All electrochemical experiments were conducted in a three-electrode cell system at room temperature. Electrochemical impedance spectroscopy (EIS) was performed using 1 mM

$\text{K}_4[\text{Fe}(\text{CN})_6]/\text{K}_3[\text{Fe}(\text{CN})_6]$ (1:1) prepared in $5\times$ PBS (pH 7.4). The following parameters were used to run the EIS: Frequency range of 100 kHz to 100 mHz, applied DC potential at open circuit potential versus silver/silver chloride, and AC pulse of 5 mV amplitude. For simulations, Z-view version 3.5 h was used to fit the EIS data into a modified Randles equivalent circuit, and the values were extracted for fitting elements by normalizing the fitting data with the electroactive area of each working electrode. For the significance test, the student's t-test was conducted in the Microsoft Excel to confirm statistical differences indicated by probability (p values). Before the t-test, the F-test was performed to compare the variances of the data sets that were to be used in the t-test.

2.3. Results and Discussion

2.3.1. Generation of microprobe-based platforms

DNA microprobes (~25-mer) are structurally flexible, carry a negative charge, and have been extensively studied for DNA biosensing applications over the past two decades.¹⁵⁷⁻¹⁶³ Owing to its neutral and rigid peptide backbone, an artificial PNA-based microprobe introduced simultaneously demonstrated enhanced hybridization efficiency and duplex stability.¹⁶⁴ In contrast, in the late 1990s, an artificial analog (LNA) with a negative charge like DNA and backbone stiffness like PNA was synthesized.^{165, 166} LNA was demonstrated to have even greater binding affinity and duplex stability for its DNA and RNA complementary sequences than PNA does for its complementary strands later.¹⁶⁷ LNA spontaneously forms A-type duplexes with complementary targets via Watson–Crick base pairing. Here, we investigated the potential of these three types of nucleic acid to address the sequence- and length-dependent structure effects on label-free impedance-based detection of CAG repeat sequences in RNA. We compared their performances against concentrations, lengths, nonspecific sequences, secondary structures, tandem vs. sporadic repeat, and divalent Mg^{2+} .

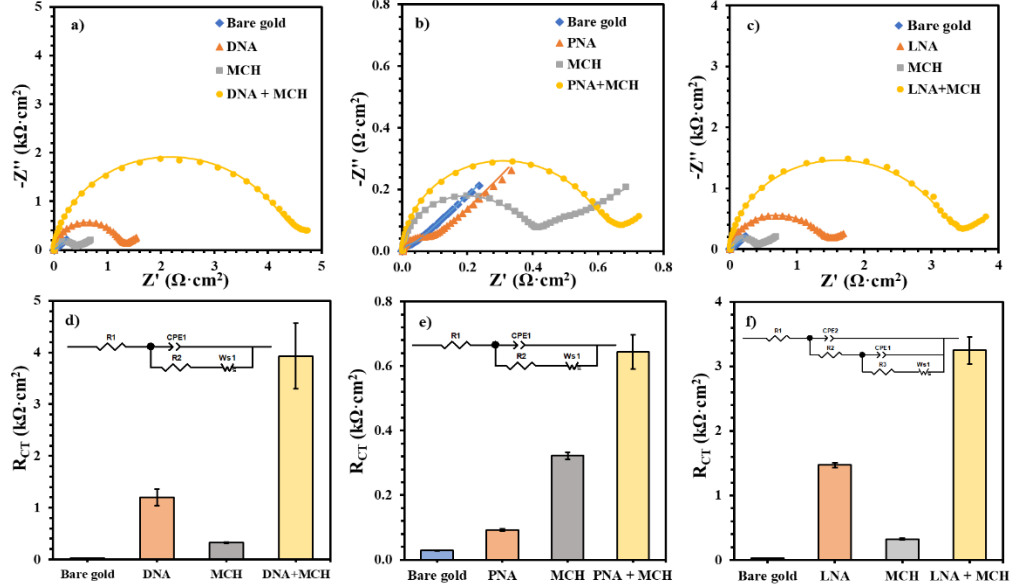


Figure 2.4. Representative Nyquist form of impedance plots and bar graphs for charge transfer resistance (R_{CT}). **a and d)** DNA microprobe, **b and e)** PNA microprobe, and **c and f)** LNA microprobe platforms. The R_{CT} for each layer of the platforms were extracted after fitting the data into the modified Randles equivalent circuit shown in the inset of bar graphs. The error bars represent the standard deviation for $N \geq 5$ distinct measurements. All measurements were normalized with the electroactive area of the

Additionally, we measured the interfacial charge transfer in the presence of a soluble redox probe, $\text{Fe}(\text{CN})_6^{3-/4-}$, using EIS. The negatively charged redox probe diffuses through the film on the electrode surface to transfer an electron, which can be inhibited at the biosensing interface by physical and electrostatic barriers.¹⁶⁸ Due to the incomparable size difference between the microprobe and long repeat targets, perfect hybridization is impossible. We hypothesized that the backbone of the microprobe could improve the distinction between lengthy and complex sequences.

Figure 2.4 shows the EIS signal and extracted R_{CT} for each layer of the microprobe platforms, i.e., DNA (**a and d**), PNA (**b and e**), and LNA (**c and f**). The R_{CT} emerged from the physical and electrostatic barriers to the diffusion of the redox probe to exchange electrons with

the electrode. The R_{CT} of DNA and LNA layers are in a similar range in the absence of the mercaptohexanol (MCH) blocking layer, i.e., 1.2 and 1.5 $k\Omega \cdot cm^2$, respectively, while after the deposition of MCH, the R_{CT} is 3.9 and 3.2 $k\Omega \cdot cm^2$ respectively. Relative standard deviation (RSD) (LNA) = 8% vs. RSD (DNA) = 16% demonstrates that the LNA microprobe performs significantly better than DNA microprobe. The enhanced precision of the LNA microprobe is attributed to its rigid backbone and higher hybridization efficiency. In contrast, the R_{CT} of the PNA-based microprobe without MCH (0.092 $k\Omega \cdot cm^2$) and with MCH (0.64 $k\Omega \cdot cm^2$) is significantly lower. The significantly lower R_{CT} of the PNA microprobe is attributable to its neutral backbone, which poses no electrostatic repulsion to the redox probe. However, both PNA and LNA microprobes exhibit RSD ~8%, indicating that the stiffness of the LNA and PNA microprobes plays a critical role in the relatively precise bilayer formation. It is important to note that the surface coverage of the microprobes may vary and play a role in the sensitivity of the platform; nevertheless, the probes were subjected to identical experimental conditions to compare their performance in this study.

2.3.2. Detecting Huntington's CAG repeats in RNA.

First, the normal and pathological lengths of *in vitro* transcribed RNA sequences were examined (**Table 2.1**). Due to the 3'- and 5'-flanking regions, the normal CAG repeat target contains 17 repeats with a total length of 152 nucleotides. The expanded pathological target length contained 306 nucleotides and 68 CAG repeats. These CAG repeat RNAs were exposed to the microprobe platforms at concentrations ranging from 100 μM to 100 nM, followed by measuring the interfacial resistance of the platform using EIS. Accordingly, the representative EIS signals of all concentrations are shown in **Figures 2.5a–2.5f**.

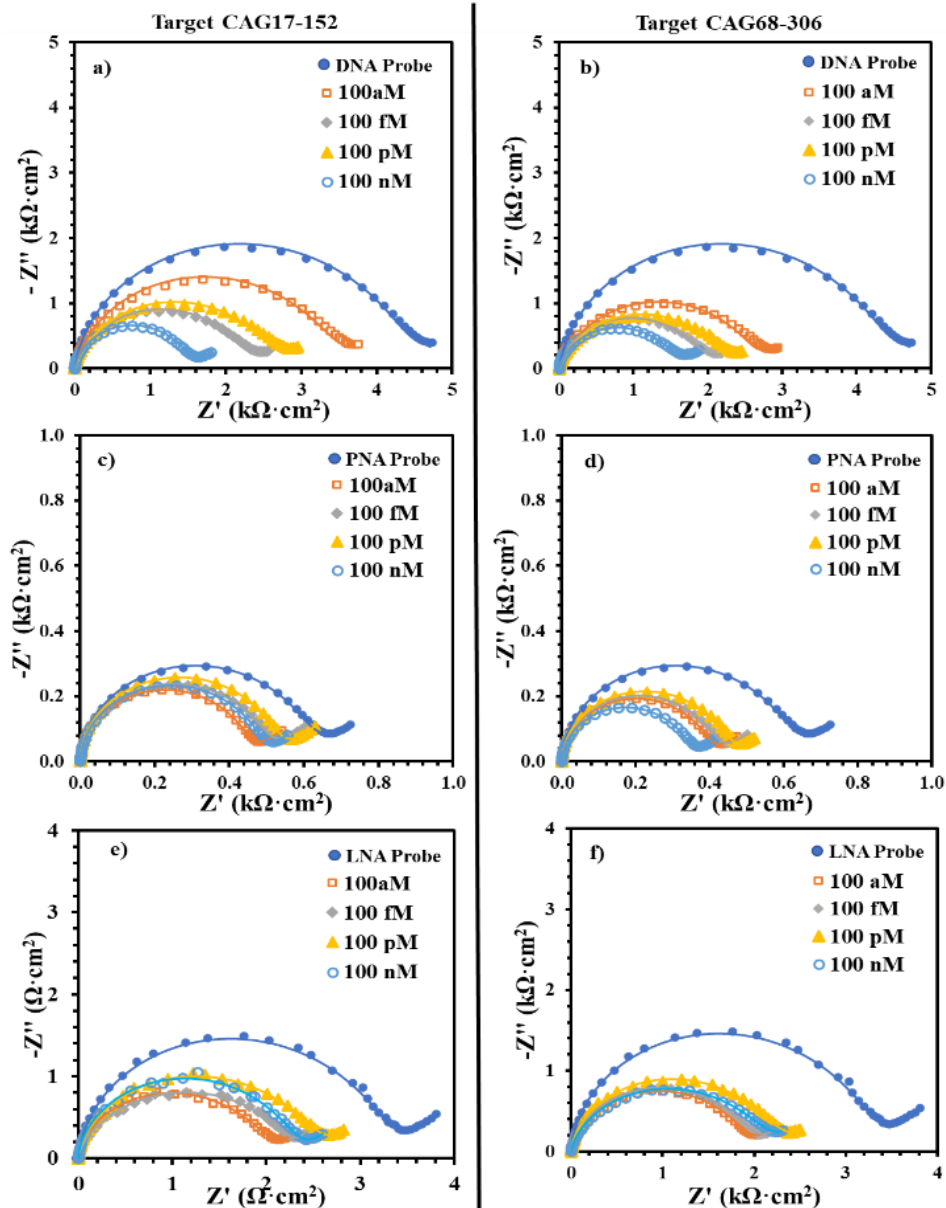


Figure 2.5. Representative Nyquist form of EIS plots of the targets at concentration range 100 aM – 100 nM. CAG17-152 (**left**) and CAG68-306 (**right**) targets were tested on DNA microprobe (**a & b**), PNA microprobe (**c & d**), and LNA microprobe (**e & f**). The data was collected in the presence of Mg^{2+} . All measurements were electroactive area normalized.

The box and whisker plots in **Figure 2.6** compare the R_{CT} signals of the CAG lengths over the concentration range measured by each microprobe platform. From these plots, several interesting observations were made. First, both targets show significantly lower R_{CT} than the

respective microprobes ($p < 0.0001$). The decrease in resistance following the target binding can be attributed to the accumulation of Mg^{2+} , which is electrostatically bound to the target, making the interfaces positively charged, facilitating the diffusion of the redox probe. Several studies have demonstrated the role of divalent cations in lowering the interfacial R_{CT} of surface-assembled DNA and PNA films.^{151, 169-172}

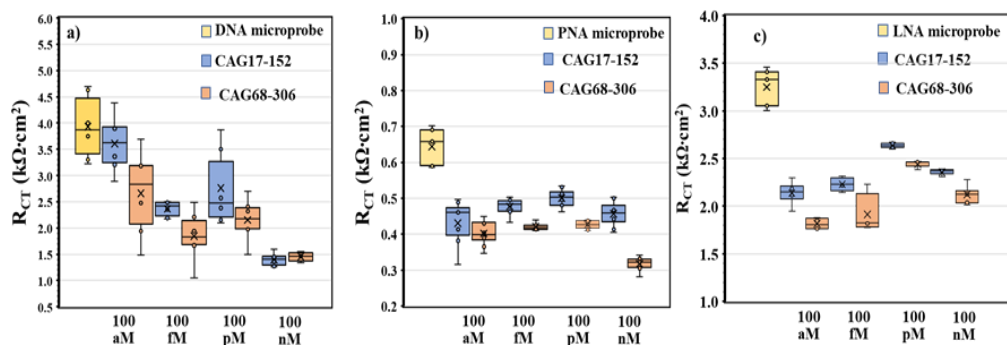


Figure 2.6. Box and whisker plots comparing the R_{CT} of the targets containing 17 and 68 CAG repeats on the **a)** DNA microprobe, **b)** the PNA microprobe, and **c)** the LNA microprobe. These platforms were exposed to the targets at 100 aM–100 nM concentrations. The data were collected in the presence of 20 mM Mg^{2+} . All the measurements were normalized with electroactive area of the working electrodes and each box plot carries $N \geq 5$ replicate measurements.

In addition, control experiments conducted in the absence of Mg^{2+} (discussed later) confirm the effect and corroborate the literature. Secondly, the longer target (68 repeats) shows an even lower resistance than the shorter target (17 repeats). We hypothesize that the lengthy target incorporates more divalent cations, thereby facilitating the diffusion of the redox probe and decreasing the R_{CT} signal. Third, the PNA and LNA microprobes resolve the target sizes better at most concentrations ($p < 0.0001$). These results suggest that PNA and LNA microprobes can invade intrastrand base pairs of the target and bind the complementary repeats more effectively than the DNA microprobe. This is due to the enhanced hybridization efficiency and duplex stability of these artificial microprobes, which are a result of their rigid backbones.^{167, 173-}

¹⁷⁶ However, the lower sensitivity of the flexible DNA microprobe may be due to its propensity to form self-hybridized secondary structures that are incapable of invading the complex target structures. **Figure 2.6** illustrates the quantitative measurements performed for each microprobe where the LNA microprobe is the most sensitive because it can distinguish target lengths at 100 aM level with $p < 0.01$ (**Figure 2.6c**). The target sample size was 5 μL , indicating that there were ~ 300 copies of the target to detect. The lack of a linear response for concentration may be due to the surface saturation caused by the length of the target. Thus, the convolution of length and concentration-dependent response is prevented.

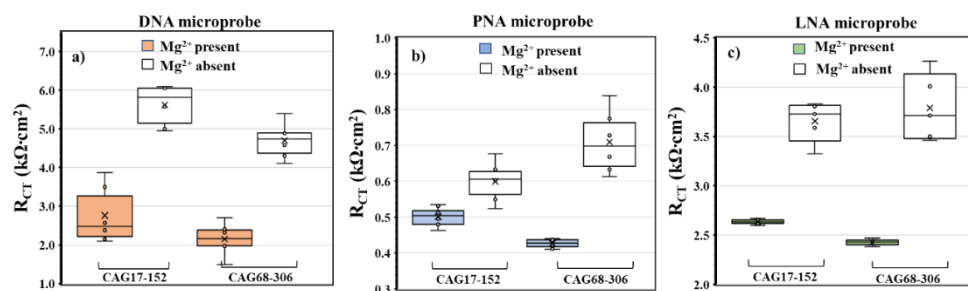


Figure 2.7. Box and whisker plots comparing the R_{CT} of the targets containing 17 and 68 CAG repeats in the presence and absence of Mg^{2+} . The responses of the **a)** DNA microprobe, **b)** the PNA microprobe, and **c)** the LNA microprobe following the exposure of the targets at 100 pM concentrations. The Mg^{2+} was removed from the interface by washing with 20 mM EDTA. All the measurements were electroactive area normalized and each box carries $N \geq 5$ replicate measurements.

Repeat expansions are known to form secondary structures,¹⁷⁷⁻¹⁸² and Mg^{2+} may facilitate folding by screening the negative charge between the phosphate groups at a lower entropic cost.¹⁸³ As the interaction with Mg^{2+} is electrostatic, the folded structure is primarily sequence- and length-driven. To confirm the effect of the divalent positive charge on the interfacial resistance of the platform, we washed the Mg^{2+} from the microenvironment of the interface with an EDTA solution following target binding. Experiments were performed at 100 pM target concentration, where PNA and LNA microprobes distinguished the lengths with a significant

difference ($p < 0.00001$ and $p < 0.05$, respectively), whereas the DNA microprobe, which does not fully resolve the lengths, performs relatively better. **Figure 2.7** compares the R_{CT} signals of the target lengths in the presence and absence of Mg^{2+} , while **Figures 2.8a–2.8c** provide representative Nyquist plots.

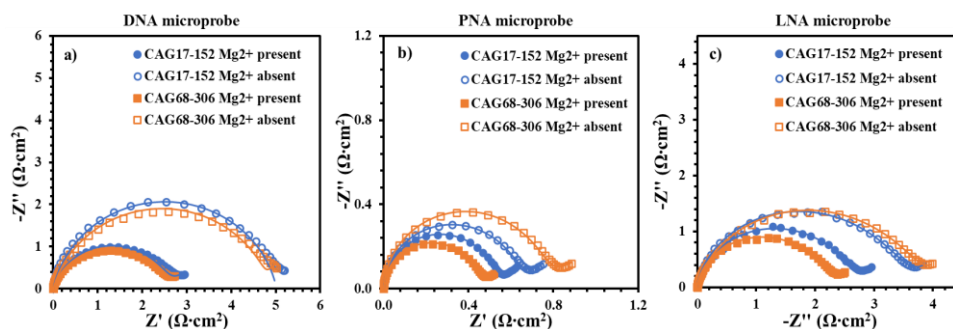


Figure 2.8. Representative Nyquist form of EIS plots comparing the target CAG17-152 and CAG68-306 in the presence and absence of Mg^{2+} . The responses of **a)** DNA microprobe, **b)** PNA microprobe, and **c)** LNA microprobe following exposure to the targets with 100 pM concentrations. The Mg^{2+} was removed from the interface by washing with 20 mM EDTA. All the measurements were electroactive area normalized.

After removing Mg^{2+} , resistance increased significantly ($p \leq 0.001$) in each of these instances. The R_{CT} after Mg^{2+} removal reflects the physical and electrostatic resistance of the targets. Furthermore, the length of the DNA microprobe (**Figure 2.7a**) was resolved in the absence of Mg^{2+} ($p < 0.01$). For the PNA microprobe (**Figure 2.7b**), the lengths were resolved in the presence and absence of Mg^{2+} ($p < 0.00001$) and ($p < 0.05$), respectively. For the LNA microprobe (**Figure 2.7c**), the lengths were more resolved in the presence of Mg^{2+} ($p < 0.05$) than in its absence. The contrasting performances of the DNA vs. LNA and PNA vs. LNA can be rationalized based on the difference in backbone stiffness in the former and the charge difference in the latter case. Based on the performance in the presence of Mg^{2+} , we further investigated the

PNA and LNA microprobes to uncouple sequence vs. structure effects in the following experiments.

We used different controls on the PNA and LNA microprobes, as detailed in **Table 2.1 and 2.2**, against the CAG17-152 target. In the presence of Mg^{2+} , **Figure 2.9** compares CAG17-152 to multiple controls on PNA (**a–d**) and LNA (**e–h**) platforms. **Figures 2.10a–2.10h** illustrate the EIS plots for these control experiments.

Initially, we evaluated a positive control (PC) sequence, CAG17-158, which is essentially the same sequence but transcribed from a "synthetic DNA template" instead of the target sequence, which was transcribed from plasmid DNA. Structurally, CAG17-152 is predicted to fold into four hairpins of nearly identical length, whereas the PC sequence is predicted to fold into one hairpin longer than the others (**Table 2.2**). **Figures 2.9a and 2.9e** demonstrate that both microprobes cannot distinguish between the target and the PC sequences because both sequences contain the same number of tandem CAG repeats. **Figures 2.9b and 2.9f** show the results of the specificity control (SC) sequence CUG17-158. CUG17-158 is not expected to bind efficiently with the microprobes because of the U–T (pyrimidine–pyrimidine) mismatches in the binding region. Notably, single-stranded CNG RNAs, in which N can be A, C, G, or U, tend to form semistable A-form-like helical and hairpin structures with common mismatches, as observed in the structure of the SC.^{181, 184, 185} The results demonstrate that both microprobes can distinguish between the target and the SC sequences. The lack of specificity led to significantly increased resistance in the control sequence, indicating a weaker or nonexistent binding between the control sequence and the microprobes. Interestingly, PNA and LNA microprobes differ in composition control (CC) sequence CAG17-158, as shown in **Figures 2.9c and 2.9g**. This CC

sequence comprises the same C, A, and G nucleotides, but in a scrambled fashion, resulting in a few “sporadic” CAG repeats.

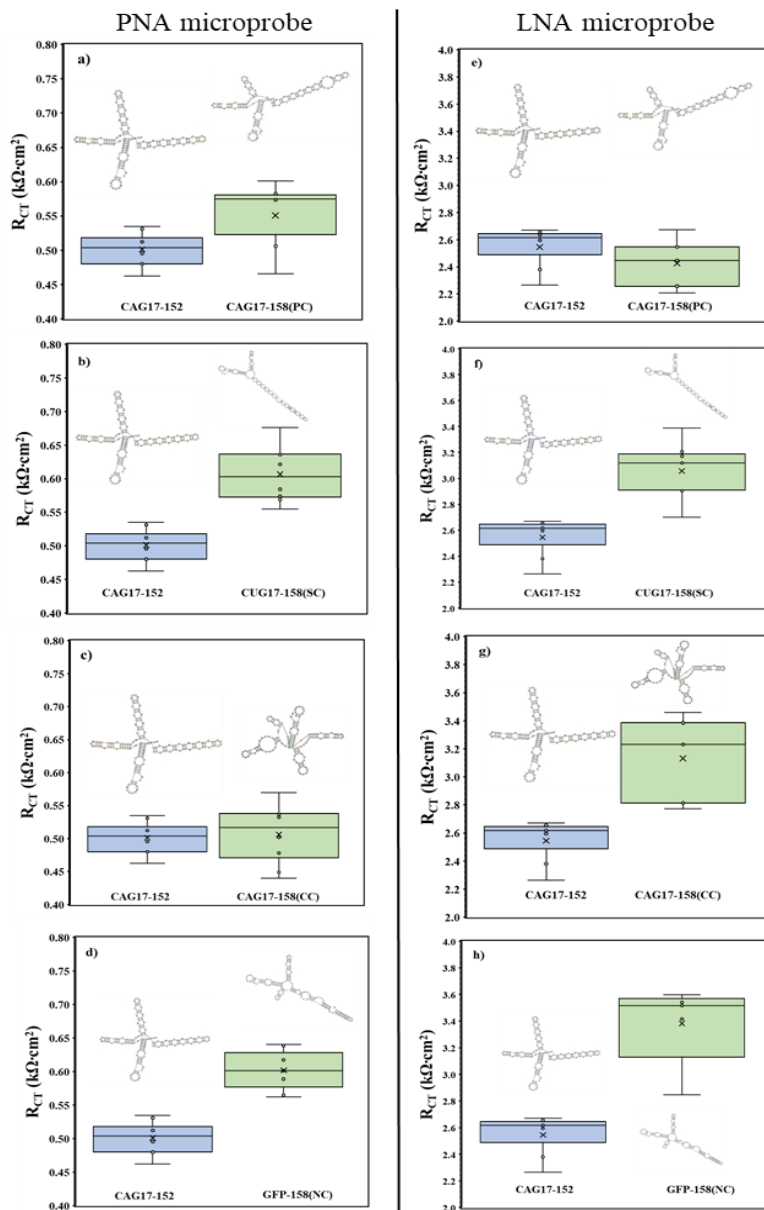


Figure 2.9. Box and whisker plots comparing the performances of the PNA microprobe (**a–d**) and LNA microprobe (**e–h**) by testing control sequences against the target CAG17-152: (**a and e**) Positive control CAG17-158, (**b and f**) Specificity control CUG17-158, (**c and g**) Composition control CAG17-158, and (**d and h**) Nontarget control GFP-158. All the measurements were performed in the presence of Mg^{2+} at 100 μM target concentration. All the measurements were electroactive area normalized and each data point carries $N \geq 6$ replicate measurements.

The absence of “tandem” CAG repeats should theoretically prevent this CC sequence from binding to the microprobes. Consequently, the R_{CT} signals show that the LNA microprobe does not bind the CC sequence and can differentiate between the target and the CC sequence. Nevertheless, the PNA microprobe detects the CC sequence and does not distinguish between the target and the control sequence. Perhaps the charge neutrality of the PNA makes it possible for the microprobe to hybridize with the sporadic CAG repeats. Although it is a strength of PNA to detect randomly dispersed complementary repeats, it is undesirable for detecting the short tandem repeats. Finally, we evaluated the nontarget control (NC), GFP-158, which has no complementarity with the microprobe but is structurally similar to the PC. **Figures 2.9d and 2.9h** show that the resistance of the NC is similar to the probe ($p > 0.05$), indicating that neither probe binds to its target. Notably, despite the structural similarity with the PC, GFP-158 does not bind to PNA or LNA microprobes, whereas the PC binds to these microprobes via its complementary binding region.

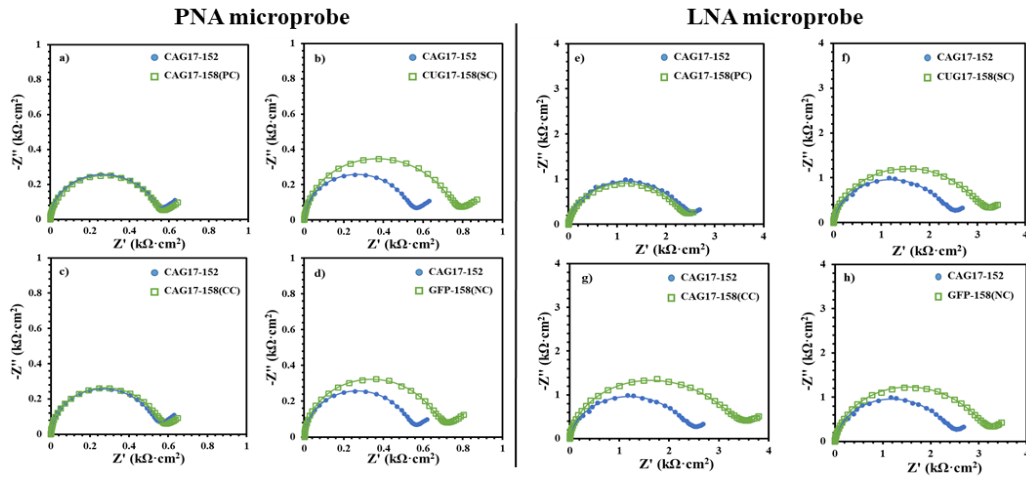


Figure 2.10. Representative Nyquist form of EIS plots comparing the target CAG17-152 with control sequences on PNA and LNA platforms in presence of Mg^{2+} . **(a&e)** Positive control CAG17-158(PC), **(b&f)** Specificity control CUG17-158(SC), **(c&g)** Composition control, and **(d&h)** non-target control GFP-158(NC). Target concentrations are 100 pM. All the measurements were electroactive area normalized.

The results presented in **Figure 2.9** required additional evidence to confirm the binding of the different controls with the microprobe. Accordingly, the binding was confirmed by removing Mg^{2+} from the biosensing interface, assuming that removing Mg^{2+} should not affect the signal of the microprobe if it had not bound a target. The EIS signals are illustrated in **Figures 2.11a–2.11h**.

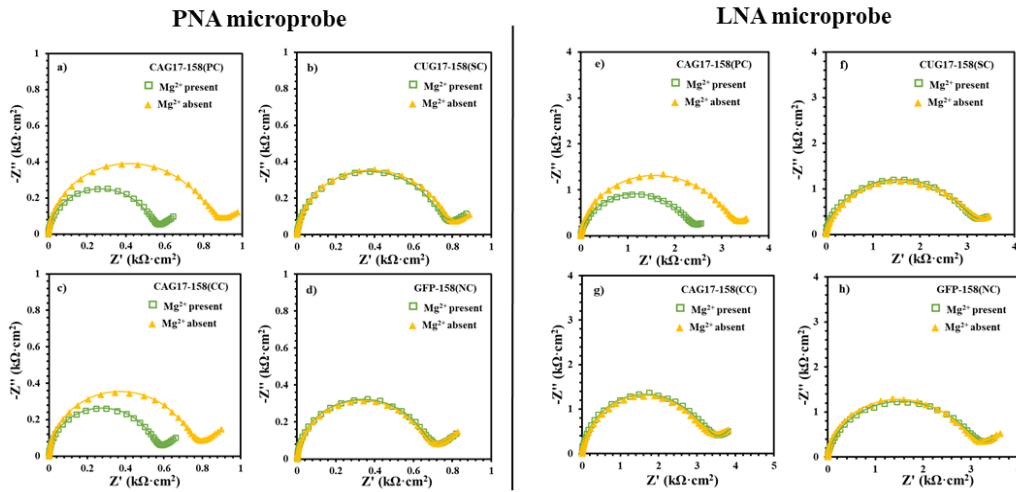


Figure 2.11. Representative Nyquist form of EIS plots comparing the control sequences in presence and absence of divalent cation Mg^{2+} on PNA (**left**) and LNA (**right**) platforms. (**a&e**) Positive control CAG17-158(PC), (**b&f**) Specificity control CUG17-158(SC), (**c&g**) Composition control, and (**d&h**) non-target control GFP-158(NC). Target concentrations are 100 pM. All the measurements were electroactive area normalized.

For both PNA and LNA microprobes, the PC produces the greatest change in resistance upon removal of Mg^{2+} ($p < 0.001$), as shown in **Figures 2.12a and 2.12e**. Moreover, there was no difference between the R_{CT} response in the presence and absence of Mg^{2+} compared to the SC ($p > 0.05$), as shown in **Figures 2.12b and 2.12f**. This confirms that none of these microprobes hybridize with the SC sequence. Interestingly, with CC, PNA shows a significant increase in resistance following the removal of Mg^{2+} ($p < 0.005$), indicating that it detected the sporadic CAG repeats (**Figure 2.12c**). However, LNA showed no change in resistance with and without

Mg^{2+} due to the absence of binding with the CC sequence (**Figure 2.12g**). Both PNA and LNA microprobes failed to bind the nontarget GFP sequence; therefore, resistance was unaffected by the removal of Mg^{2+} (**Figures 2.12d and 2.12h**).

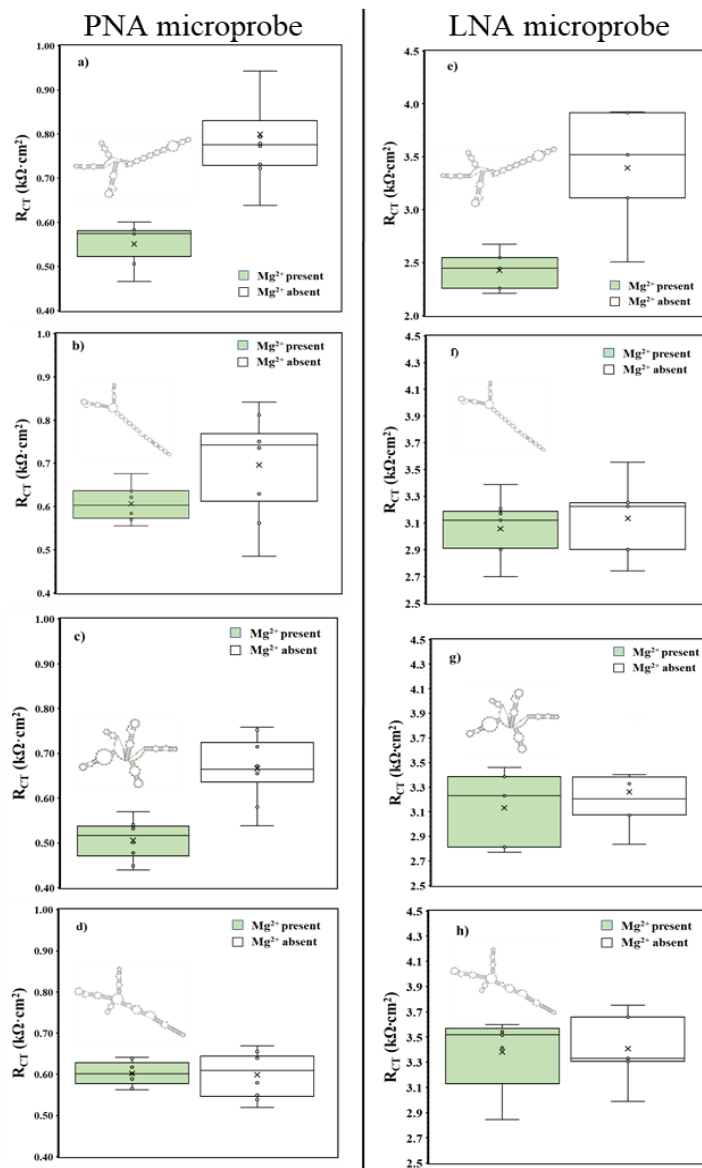


Figure 2.12. Box and whisker plots comparing the performances of the PNA microprobe platform (**a–d**) and LNA microprobe platform (**e–h**) in the presence and absence of Mg^{2+} for the control sequences: (**a and e**) Positive control CAG17-158, (**b and f**) Specificity control CUG17-158, and (**c and g**) Composition control CAG17-158, and (**d and h**) Nontarget control GFP-158. Target concentrations are 100 pM. All the measurements were area normalized, and each data point carries $N \geq 6$ replicate measurements.

2.4. Conclusion

The effect of secondary structures and sporadic repeats on the label-free detection of short tandem repeat sequences was investigated in this study. We designed three biosensing platforms with different nucleic acid microprobe backbones (DNA, PNA, and LNA) and detected Huntington's CAG repeats in *in vitro* transcribed RNA sequences. We found that pathogenic lengthy repeats show lower signal than the normal sequence, more distinctly, on PNA and LNA platforms than DNA microprobes. LNA distinguished lengths at concentrations as low as 100 aM and sequences in the presence of Mg^{2+} . Furthermore, PNA and LNA microprobes were unaffected by the secondary structure of the control sequences and detected tandem CAG repeats with high specificity. However, unlike PNA, LNA did not detect sporadic repeats, which rectifies the false-positive signaling caused by sporadic repeats in real samples.

CHAPTER 3

ELECTROCHEMICAL IMPEDANCE IMMUNOASSAY FOR ALS-ASSOCIATED NEUROFILAMENT PROTEIN: MATRIX EFFECT ON THE IMMUNOPLATFORM

3.0. Abstract

Amyotrophic Lateral Sclerosis (ALS) is a neurodegenerative disorder, which has complex diagnostic steps. Electrochemical immunoassays may make the diagnosis simpler and faster. Here, we present the detection of ALS-associated neurofilament light chain (Nf-L) protein through an electrochemical impedance immunoassay on reduced graphene oxide (rGO) screen-printed electrodes. The immunoassay was developed in two different media, i.e. buffer and human serum, to compare the effect of the media on their figures of merit and calibration models. The label-free charge transfer resistance (R_{CT}) of the immunoplatfrom was used as a signal response to develop the calibration models. We found that exposure of the biorecognition layer to human serum improved the impedance response of the biorecognition element with significantly lower relative error. Moreover, the calibration model obtained in the human serum environment has higher sensitivity and a better limit of detection (0.087 ng/mL) than the buffer medium (0.39 ng/mL). The analyses of the ALS patient samples show that concentrations obtained from the buffer-based regression model was higher than the serum-based model. However, a high Pearson correlation ($r = 1.00$) between the media suggests that concentration in one medium may be useful to predict the concentration in the other medium. Moreover, the Nf-L concentration appears to increase with age in both male and female groups, while overall higher Nf-L was found in the male group than the female group.

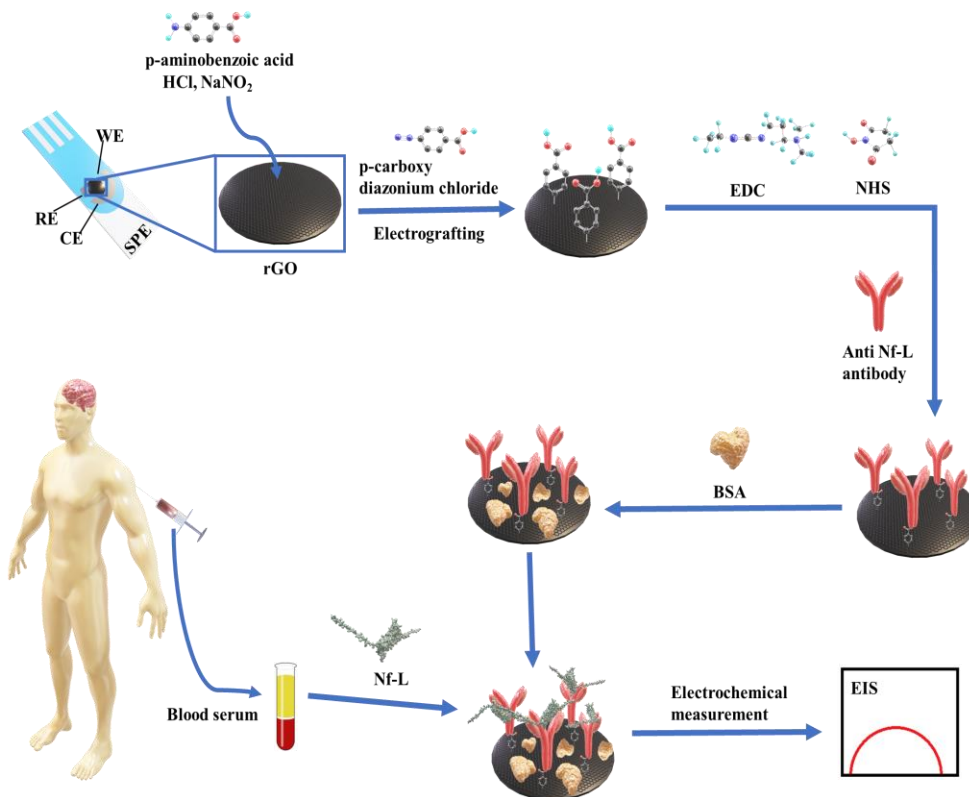
3.1. Introduction

Amyotrophic lateral sclerosis (ALS) is a fatal neuromuscular disease that causes death within five years of onset of symptoms.¹⁰⁵ Diagnosis for ALS relies on a detailed history of the symptoms, a series of muscle testing to rule out other diseases, and imaging tests.¹⁸⁶ The availability of a range of sensitive tools to diagnose the disease is difficult in a resource-limited region.¹³² However, recent progress in the identification of ALS-associated biomarkers present in biological fluids is promising for developing sensitive and inexpensive electroanalytical diagnostic protocols.^{88, 187-189} In contrast to current ALS diagnostics methods, electrochemical detection methods¹⁹⁰ have emerged as a promising alternative due to their simplicity, quick process¹⁹¹ affordability, and sensitivity.¹⁹² These methods can be integrated into miniaturized platforms, such as screen-printed electrodes and microfluidic chips,¹⁹³ to detect a wide range of analytes in different biological samples, including blood,¹⁹⁴ urine,¹⁹⁵ sweat,¹⁹⁶ and saliva.¹⁹⁷ The electrochemical detection platform incorporates a diverse range of surfaces, harnessing the unique properties of nanomaterials to enhance its sensing capability.^{198, 199} One such material is reduced graphene oxide, a class of two-dimensional nanomaterial, which is utilized for its convenient functionalization in immobilizing biorecognition elements.²⁰⁰ The material shows remarkable electrochemical conductivity, high surface area, biocompatibility, and hydrophilic characteristics, resulting in improved sensitivity and detection limits in the electrochemical detection process.²⁰¹

In past 25 years,²⁰² a number of protein biomarkers have been linked to ALS such as polydipeptide repeats (DPRs), Neurofilament Heavy Chain (Nf-H), Neurofilament light Chain (Nf-L), and phosphorylated neurofilament heavy (pNfH) and light chain (pNfL).¹⁰⁶ Currently, these biomarkers were detected in cerebrospinal fluid (CSF) due to their high concentration in

the biological fluid,^{203, 204} while obtaining a CSF sample is highly invasive. Recently, Nf-L received a significant attention as a biomarker for early-stage diagnosis,²⁰⁵ which can be detected in serum.^{205, 206} We expect that the detection of Nf-L in serum using a rapid, label-free, and sensitive detection method will make the diagnosis procedure less invasive, thus less painful, for ALS patients.

Detection of diagnostic biomarkers in a complex biological medium (e.g., serum) usually requires tedious sample preparation to enrich the biological sample with a desired biomarker. In contrast, testing enriched and complex target samples via highly sensitive techniques, such as impedance, may fall beyond the dynamic range of the calibration model. Therefore, dilution of such samples might be necessary but also at risk of compromising accuracy and precision. In this work, we have detected the ALS-associated Nf-L protein in patients sera using impedance-based electrochemical immunoassay. **Scheme 3.1** depicts the detection strategy where an antibody biorecognition layer was formed on a reduced graphene oxide (rGO) screen-printed electrode through an electrografting method where anti-Nf-L antibody is immobilized on the rGO surface through a 4-carboxyphenyl linker.^{207, 208} Then, Nf-L was detected using the immunoplatfrom by monitoring the label-free impedance signal of the detection platform. The immunoassay was employed in buffer and serum to compare the effects of the media on the figures of merit and regression model of the assay and to observe the effect on the analysis of real samples. This detection strategy is simple, label-free, and less invasive compared to other electrochemical methods that used brain tissues and various signal amplification methods.^{127, 128, 209}



Scheme 3.1. Depicting step by step preparation of the electrochemical immunosensing platform on rGO screen-printed electrodes and the detection of ALS-associated Nf-L biomarker in patients sera using the developed immunosensing platform.

3.2. Experimental

3.2.1. Materials

Synthetic neurofilament light chain (Nf-L)—a human recombinant protein (P01)—with theoretical molecular weight 87.9 kDa, was purchased from Abnova corporation. Anti-Nf-L monoclonal antibody (DA2) was procured from Invitrogen, Thermo Fisher Scientific. Commercial human serum (from human male AB plasma, USA origin, sterile-filtered), bovine serum albumin (BSA) lyophilized powder ($\geq 96\%$), sodium nitrite ($\geq 99.0\%$) and 4-aminobenzoic acid ($\geq 99\%$) were purchased from Sigma-Aldrich. ALS patient serum samples were acquired from National ALS Biorepository, obtained, and stored at $-80\text{ }^{\circ}\text{C}$. 1-ethyl-3-(3-

dimethylaminopropyl)carbodiimide (EDC) hydrochloride, *N*-hydroxysuccinimide (NHS) and [2-(*N*-morpholino)ethanesulfonic acid] (MES) 0.1 M, with 0.9% sodium chloride were purchased from ThermoFisher Scientific. Potassium ferricyanide (99+%) and potassium ferrocyanide trihydrate (99+%) were purchased from Acros Organic while phosphate buffer saline 10× were obtained from Sigma life science. All the solutions were prepared in ultrapure water (18.2 MΩ·cm) from Barnstead Smart2Pure 3LPH, Thermo Scientific. Reduced graphene oxide modified screen printed carbon electrode (DRP-110RGPHOX) were purchased from Metrohm USA. All electrochemical measurements were performed employing Metrohm Autolab PGSTAT204 FRA32M (USA) electrochemical workstation connected with Metrohm Dropsens adapter (DRP-DSC4MM70734) inside Metrohm Autolab Faraday cage.

3.2.2. Preparation of Immunoplatfrom.

A biorecognition layer was prepared on the reduced graphene oxide (rGO) screen-printed electrode (SPE). The SPE comprised of an rGO working electrode with 4 mm diameter, a carbon counter electrode, and a silver pseudoreference electrode. The rGO working electrode was first modified with carboxyphenyl group using electrografting method.^{207, 208} First, 2 mM of NaNO₂ was added into 2 mM of 4-aminobezoic acid prepared in 0.5 M HCl to generate diazonium cation. After 5 minutes of reaction, 150 μL of the solution was dropped onto the rGO surface. Covalent immobilization of 4-carboxyphenyl group was obtained by electrografting using cyclic voltammtery (CV) from 0.4 to -0.6V for 3 cycles at 200 mV/s scan rate. For anti-Nf-L antibody immobilization, 10 μL of 100 mM EDC and 20 mM NHS prepared in 100 mM MES buffer (pH 5) was dropped on carboxy phenyl modified rGO surface and the electrode was incubated around 8 °C for 1 h. The surface was carefully washed with MES buffer followed by incubation of 10 μL of 20 ng/mL anti-Nf-L antibodies, prepared in 1× PBS buffer (pH 7.4) for 3 h at 8 °C. Then, the

surface was washed with PBS buffer and exposed to 10 μL of 1% BSA as a blocking layer for 1 h followed by washing with PBS buffer. The biolayer was also exposed to 10 μL undiluted serum for 15 minutes followed by washing with PBS buffer. Synthetic Nf-L targets in the concentration range 0.01 to 1.5 ng/mL were prepared in $1\times$ PBS and in serum separately and were immobilized in respective biorecognition layer for 15 minutes followed by washing with PBS buffer.

3.2.3. Nf-L detection by EIS.

Each of the biolayer preparation steps and target immobilization steps were electrochemically characterized to confirm the modification. EIS was performed using 1 mM $\text{K}_4[\text{Fe}(\text{CN})_6]/\text{K}_3[\text{Fe}(\text{CN})_6]$ (1:1) prepared in $1\times$ PBS (pH 7.4) as a soluble redox active probe. The EIS measurements were performed in frequency range of 100 kHz to 0.150 Hz with an applied DC potential (open circuit potential), and AC pulse of 5 mV amplitude. For simulations, Z-view version 3.5h was used to fit the EIS data into a modified Randles equivalent circuits. The experimental and extracted values of fitting elements were normalized by electroactive area at each step. For real samples, serum samples from ALS patients were obtained National ALS biorepository and stored in $-80\text{ }^\circ\text{C}$ freezer. Aliquots of samples were taken out in small Eppendorf tube and diluted with $1\times$ PBS (pH 7.4) and then around 150 μL of sample was incubated for 15 minutes in closed container with humid environment at room temperature. The electrodes were then washed with 10 μL of $1\times$ PBS for three times before EIS measurements.

3.3. Results and discussion

3.3.1. Preparation of immunoplatfrom.

The immunoplatfrom on rGO screen-printed electrode was prepared by immobilizing anti-Nf-L antibody on the electrodes using electrografting method.^{207, 208} **Figure 3.1** presents the

formation of the biorecognition layer comprising bare rGO, antibody (anti-Nf-L) onto rGO, and BSA treatment of the immobilized antibody.

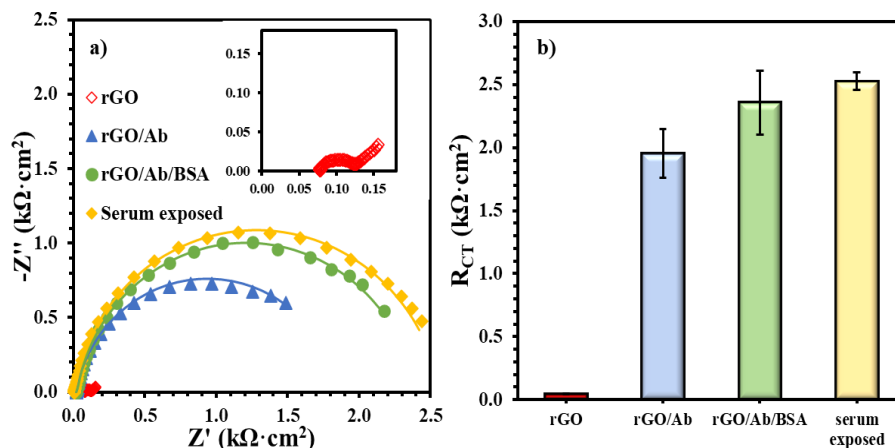


Figure 3.1. a) EIS plots for biolayer formation including unmodified rGO surface (inset), anti-Nf-L antibody rGO/Ab, after 1% BSA treatment rGO/Ab/BSA, and after the human serum exposure. b) Comparing R_{CT} values after modifying the rGO electrode with each successive layer. The error bars represent $n \geq 4$ distinct replicates.

Figure 3.1a shows the Nyquist form of the EIS plots of main layers, i.e., electrode (rGO), antibody (G/Ab), complete biolayer (rGO/Ab/BSA), and human serum exposed biolayer. **Figure 3.1b** summarizes the impedance of each layer, i.e., charge transfer resistance (R_{CT}), emerged from steric hindrance to the soluble redox probe. The unmodified rGO surface has extremely low resistance ($0.040 \pm 0.003 \text{ k}\Omega \cdot \text{cm}^2$), which increased almost two orders of magnitude ($1.95 \pm 0.20 \text{ k}\Omega \cdot \text{cm}^2$) after covalent immobilization of the anti-Nf-L on the electrografted rGO surface. After the exposure of rGO/Ab to 1% BSA, the resulting rGO/Ab/BSA biolayer had impedance of $2.4 \pm 0.25 \text{ k}\Omega \cdot \text{cm}^2$ with RSD $\sim 10\%$. The purpose of BSA in preparing such platforms is to reduce non-specific adsorption. However, the 10% relative error indicates that the platform is prone to high false-positive signal. Then, we exposed the rGO/Ab/BSA biolayer to an undiluted commercial human serum followed by washing with the buffer. The exposure to human serum

significantly improved the precision of the bilayer response, i.e. $2.5 \pm 0.07 \text{ k}\Omega \cdot \text{cm}^2$ and RSD $\sim 3\%$. Rationally, human serum is more biologically relevant toward biorecognition layer and the serum exposure may have covered some exposed rGO surface left after the adsorption of BSA.²¹⁰

3.3.2. Nf-L detection in buffer and serum media.

The Nf-L concentration in human serum has been reported in the range 0.05 – 0.879 ng/mL for early-stage ALS and 0.02 – 4.2 ng/mL for late-stage ALS patients.^{211,212} Despite the wide and varied ranges of Nf-L concentration in human serum, the median values for both stages are very similar, i.e. 0.26 ng/mL and 0.2 ng/mL respectively. Clinical serum has a complex matrix, which makes it highly challenging to detect the target biomarker. Protein enrichment is needed for the detection of low abundant target in serum. However, sample preparation may result in quantitative loss of molecule of interest.²¹³ It is critical to know that buffer-based calibration model usually do not relate with real sample matrix, such as serum samples. To better understand the matrix effect on the immunoplatfrom, it is important to compare a buffer-based calibration with a serum-based calibration. It was assumed that an appropriate regression model may be around the reported median value of the Nf-L in serum. Therefore, we prepared and analyzed the synthetic Nf-L target in concentration range of 0.01 - 1.5 ng/mL prepared in PBS buffer and filtered human serum. **Figure 3.2a** shows EIS signals of the synthetic Nf-L target in PBS buffer. The increase in R_{CT} signal with the concentration confirms the immobilization of the target on the immunoplatfrom. The dynamic response was observed in the concentration range that can be observed in the calibration curve shown in inset of **Figure 3.2a**. The limit of detection (LOD) was calculated as 0.39 ng/mL (S/N =3) from linear regression equation ($y = 1.9x + 2.9$) obtained in the buffer medium. **Figure 3.2b** represents EIS response of the synthetic

Nf-L protein prepared in human serum along with the regression curve in the inset. The response of the concentrations were higher in the serum medium, which was expected due to the complexity of the medium. Nevertheless, the sensitivity (slope) of the curve was higher ($y = 2.4x + 3.0$) and LOD was calculated as 0.087 ng/mL (S/N =3), which is one order of magnitude better than that of the buffer medium. We assume that the better precision of the serum-exposed biolayer improved the LOD from serum-based calibration plot due to similar matrix. We performed comparative analysis of R_{CT} signals of two data sets obtained from serum and buffer calibration media and found no significant difference in variance ($p > 0.08$) and in means ($p > 0.6$). Which further approves that there is similarity of the results obtained from both media and can be correlated from each other.

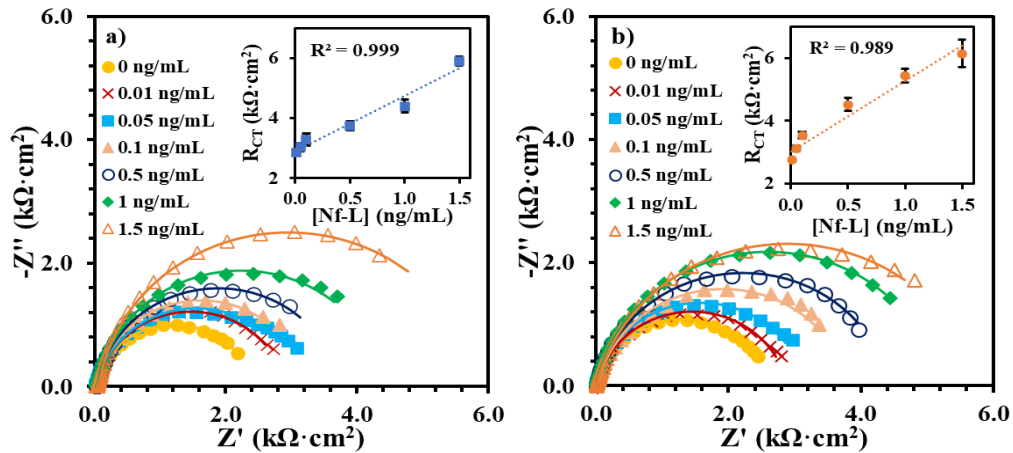


Figure 3.2. EIS signals of the synthetic Nf-L target captured at the immunoplatfrom from concentration range (0.01 to 1.5 ng/mL) in buffer medium PBS pH 7.4 **a)** and in serum **b)**. The insets in **a)** and **b)** show corresponding calibration plots of R_{CT} vs. concentration. Each error bar represents $n \geq 3$ replicates.

The correlation between the R_{CT} signals obtained from buffer and serum-based calibration curve (**Figure 3.3**) shows that both calibration models are reasonably correlated as indicated by the Pearson correlation coefficient $r = 0.952$. Since we use monoclonal anti-Nf-L

antibody therefore we assumed that there is no significant interference observed and due to the reason, the buffer and serum matrix results show high correlation. Due to the correlation, we used both regression models to calculate concentrations of Nf-L in the diluted sera samples from ALS patients.

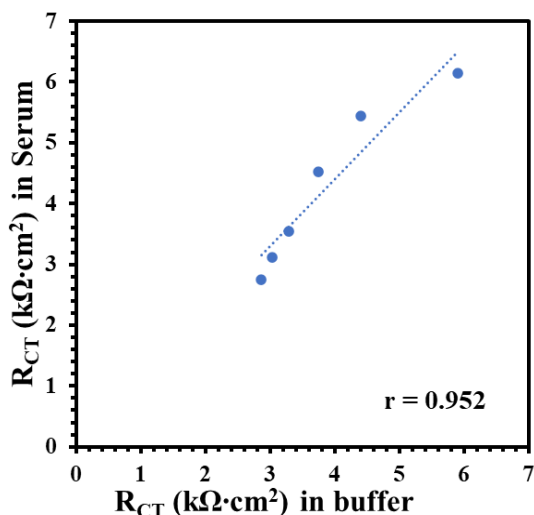


Figure 3.3. Correlation plot between R_{CT} of synthetic Nf-L targets in commercial human serum with the R_{CT} obtained in $1\times$ PBS buffer. Pearson correlation coefficient $r = 0.952$ shows high correlation between target signals obtained in these two

3.3.3. Target Nf-L determination in ALS patients' serum.

Finally, ALS sera samples were tested from male and female groups of varied ages to determine Nf-L concentration using the immunoplatfrom and the regression models. The samples were $10\times$ diluted in $1\times$ PBS buffer (pH 7.4) followed by exposure to immunosensing platform. After the brief exposure, the EIS measurements were performed preceded by washing as described above. **Table 3.1** shows the R_{CT} signals of the sera samples normalized by the electroactive area of the electrodes and corresponding concentration of Nf-L calculated from buffer- and serum-based regression equations. The concentrations obtained were multiplied with $10\times$ dilution factor to estimate the actual concentration in the sera.

Table 3.1. Charge transfer resistance (R_{CT} signals) of ALS serum samples and the concentration of Nf-L obtained in serum-based and PBS buffer-based calibration model. The data is divided into two groups based on gender and it represents varied ages. Actual concentration of Nf-L in the serum was calculated by multiplying the concentration obtained from the regression model with $10\times$ dilution factor. R_{CT} and concentration values of each sample show standard error for $n \geq 3$ replicates.

Sample ID	Gender	Age	R_{CT} ($k\Omega \cdot cm^2$)	Nf-L (ng/mL) Serum	Nf-L (ng/mL) Buffer
1	Male	40s	4.1 ± 0.17	4.4 ± 0.7	6.0 ± 0.9
2		50s	5.1 ± 0.37	8.9 ± 1.6	12 ± 2.0
3		60s	4.8 ± 0.52	7.4 ± 2.2	9.7 ± 2.7
4		70s	5.1 ± 0.43	8.9 ± 1.8	12 ± 2.3
5		80s	5.5 ± 0.31	10.3 ± 1.3	13 ± 1.6
6	Female	30s	3.9 ± 0.24	3.9 ± 1.0	5.3 ± 1.2
7		50s	4.2 ± 0.27	5.2 ± 1.1	7.0 ± 1.4
8		60s	4.1 ± 0.18	4.7 ± 0.8	6.3 ± 0.9
9		60s	4.3 ± 0.43	5.5 ± 1.8	7.3 ± 2.2
10		70s	4.9 ± 0.20	7.9 ± 0.8	10 ± 1.0

The serum dilution may be useful when target concentration in patient is expected to present at elevated level than the dynamic range of the regression model such as in case of late-stage ALS (4.2 ng/mL).²¹⁴ The concentrations of the Nf-L from patients were plotted in male and female groups in **Figure 3.4a**. Interestingly, we found that Nf-L concentration tends to increase with age in both male and female patients. It is important to note that there have been inconsistent reports on the correlation between Nf-L concentration and age of ALS patients, for instance, a report states no direct correlation,²¹⁵ while another report shows Nf-L concentration correlation with the age of healthy controls and other neurological diseases.²¹⁶ We also observed average Nf-L concentration higher in the male group than the female group, which is also not proven from previous studies. Since the work of the biomarker identification and their estimation in biological fluids is still in progress, therefore, more reports are expected in the future for conclusive evidence. **Figure 3.4b** shows the high correlation ($r = 1.00$) between the concentrations obtained from buffer-based calibration and serum-based calibration models,

which indicates that the correlation can be used as predictive model to find the concentration in one medium from other medium and vice versa.

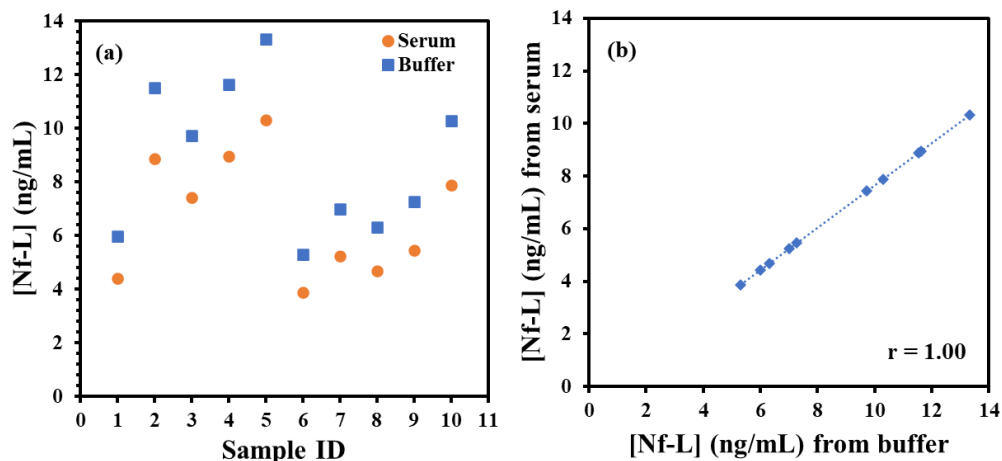


Figure 3.4. a) Plot of target Nf-L concentration in ALS serum samples. The concentrations calculated from serum-based calibration plot (orange circle) and buffer-based calibration plot (blue square). **b)** shows correlation plot between the concentration of Nf-L in real ALS samples calculated from serum-based calibration model versus buffer-based calibration model. Pearson correlation coefficient $r = 1.00$ shows very high correlation between these two media.

There have been several recent studies on electrochemical detection of Nf-L. However, these studies relied on complex biorecognition elements and label for signal amplification. One of such detection strategies involved sandwich type immunoassay complexes formed over magnetic microbead, which was conjugated with horse radish peroxidase (HRP) to generate electroactive product for amperometric detection²⁰⁹, In another work, electrochemical detection was based on ratio of glycosylated Nf-L (oNf-L) to total Nf-L (tNf-L) was determined.¹²⁸ Both targets were detected in buffer diluted serum where tNf-L detection involved sandwich type immunoassay bearing nanoparticles over gold electrode surface. Nanoparticles containing Cu^{2+} provides electrochemical reduction signal to quantify tNf-L. While, oNf-L detection involved horseradish peroxidase–wheat germ agglutinin (WGA–HRP) complex–specifically immobilized

on oNf-L, which then catalyzed reduction of O₂ from H₂O₂. Nf-L was also detected on metal organic framework-derived material (ZrO₂@La₂O₃) using a simple immunoassay for voltametric detection.¹²⁷ Nevertheless, such metal organic frameworks are expensive materials compared to graphene oxide which is simple to synthesize and modify through chemical and electrochemical methods as we described in this report. In our work, using the serum-based calibration we were able to achieve LOD as low as 0.087 ng/mL, which is sensitive enough to detect reported mean concentration of Nf-L in serum samples of neurodegenerative disease patients (0.65 ng/mL).²¹⁷

3.4. Conclusion

In this work, we demonstrated the effect of immunoassay medium on electrochemical detection of ALS-associated Nf-L protein biomarker. The immunoplatfrom was prepared on reduced graphene oxide screen-printed electrodes by immobilizing the anti-Nf-L antibody through electrografting method. The final biorecognition layer showed improved charge transfer resistance response when exposed to human serum and the relative standard error reduced from 10% to 3%. The regression models obtained in the serum medium showed higher sensitivity and better limit of detection (0.087 ng/mL) than the buffer medium (0.39 ng/mL). Both calibration models were found reasonably correlated ($r = 0.952$) and used to estimate Nf-L concentration in patient serum samples. The estimation of Nf-L from buffer-based regression was found slightly higher than the serum-based regression model but the concentrations were found highly correlated ($r = 1.00$), which can be used to predict a concentration in serum medium using the concentration from buffer medium and vice versa. Interestingly, we found increase in Nf-L level with age in both male and female groups of ALS patients. We also found an average higher concentration in the male group than the female group. The immunoplatfrom developed here is label-free, simple, and sensitive to detect Nf-L for ALS diagnosis through less-invasive method.

CHAPTER 4

ELECTROGRAFTED LASER INDUCED GRAPHENE: SENSITIVE DETECTION OF NEURODEGENERATIVE DISEASE BIOMARKER IN CEREBROSPINAL FLUID

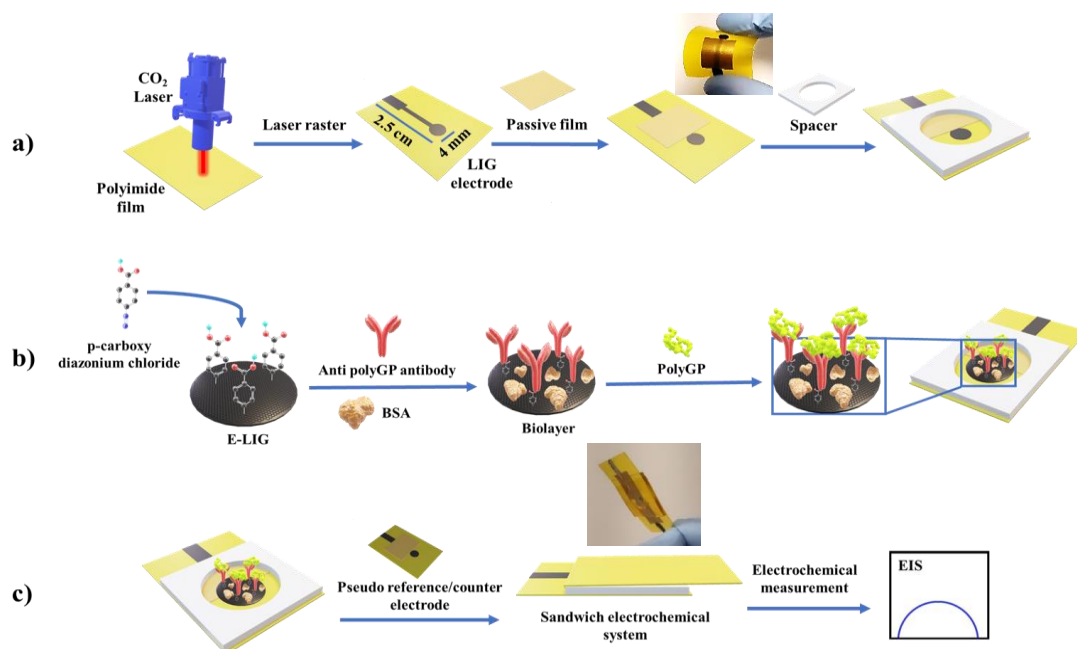
4.0. Abstract

There are more than 50 neurodegenerative disorders and amyotrophic lateral sclerosis (ALS) is one of the most common disorders that poses diagnostic and treatment challenges. Poly Glycine Proline (polyGP) dipeptide repeat is a toxic protein that has been recognized as pharmacodynamic biomarker of c9⁺ ALS, a sub type of ALS which originates from genetic mutation. An early detection of pharmacodynamic biomarkers like polyGP will help healthcare providers start timely gene therapy. Here, we developed a label-free electrochemical immunoassay for simple detection of polyGP in unprocessed CSF samples from ALS patients. We employed for the first time electrografting of Laser Induced Graphene (LIG) electrode system in a sandwich format to detect polyGP using label-free electrochemical impedance technique. The results show that E-LIG modified surface exhibited high sensitivity and selectivity in buffer with limit of detection (LOD) of 0.142 ng/mL and in CSF (LOD = 0.224 ng/mL). The precision of the calibration model in CSF was found better than buffer. The E-LIG immunosensor can easily select PolyGP target in presence of other dipeptide proteins translated from c9 gene. Further study with real CSF samples from ALS patients demonstrates that the E-LIG-based immunosensor not only quantifies polyGP in the complex CSF matrix but also distinguishes between c9⁺ and c9⁻ ALS patients. The results promise that the proposed sandwich-type E-LIG electrochemical system offers a sensitive and cost-effective tool to detect neurodegenerative biomarkers in complex biological matrices.

4.1. Introduction

Amyotrophic lateral sclerosis (ALS) is among 50 neurodegenerative disorders, which causes progressive degeneration of motor neurons that leads to death within 5 years of onset.¹⁰⁵ Length mutation—also known as repeat expansion—of G₄C₂ repeats in C9orf72 gene is the leading genetic cause of ALS.^{218, 219} If genetic biomarkers are detected sooner, then the life of the patient can be improved through gene therapy.^{106, 220} The G₄C₂ length mutation translates into the production of dipeptide toxic proteins, prevalently Poly Glycine Proline (PolyGP), which is an important pharmacodynamic biomarker. Thus, rapid and sensitive detection of polyGP may facilitate diagnosis in both symptomatic and asymptomatic patients but also offers insights into the treatment efficacy. Recently, polyGP was found in high quantities in cerebrospinal fluids (CSF),^{107, 108} which carries substantially low protein content, i.e. 0.2 – 0.4 mg/mL, in contrast to serum containing 60 – 80 mg/mL.^{221, 222} Therefore, detection of polyGP in CSF may simplify diagnosis through direct detection using patient CSF without sample preparation steps.

Various techniques are employed to discriminate between C9orf72 and non C9orf72-patients, such as polymerase chain reaction,^{223 224} immunohistochemistry,²²⁵ and neuroimaging techniques.²²⁶⁻²²⁸ However, these methods are time-consuming, involve sophisticated procedures and instrumentation, and well-trained personnel.^{229, 230} Electrochemical sensors can help by providing a sensitive, miniaturized, and cost-effective diagnostic tool for faster diagnosis.²³¹ One of the biggest advantage of the electrochemical tools is the low sample requirement down to nanoliters (nL) level,²³² which is desirable for the samples difficult to obtain, such as CSF.²²¹ The sensitivity of electrochemical platforms can be further enhanced using conductive 2D nanomaterials as a transducer surfaces such as graphene, MoS₂ etc.²³³⁻²³⁵



Scheme 4.1. a) A single step formation of LIG by rastering CO₂ laser over Polyimide film. A vinyl passive film was pasted to cover the wire connection followed by pasting 1.8 mm dual adhesive acrylic gel as spacer. **b)** Electrografting of LIG to functionalize surface with carboxyphenyl group to form E-LIG. Covalent immobilization of anti-polyGP antibody form biorecognition layer then filling remaining surface with BSA followed by polyGP target capture. **c)** Detection of polyGP on a sandwiched electrochemical system in presence of redox probe [Fe(CN)₆]³⁻/[Fe(CN)₆]⁴⁻ where the top bare LIG electrode serves as a pseudo reference/counter electrode.

We present here the direct detection of polyGP biomarker in CSF from patients on laser-induced graphene (LIG) electrodes. LIG is a wet-free method to create 3D porous graphene in single step using a CO₂ laser.²³⁶ The porous graphene produced by this method provides a large surface area and superior electronic conductivity, which is key to enhance detection sensitivity for complex biological samples, especially for label-free detection strategy.^{237, 238} **Scheme 4.1a** illustrates the fabrication of LIG sensors in a single-step by exposing a polyimide substrate to CO₂ laser. The LIG sensors were functionalized with carboxyphenyl groups via electrografting followed by the immobilization of anti-polyGP antibodies to prepare a biorecognition as shown in **Scheme 4.1b**. The sensor construct was assembled into a sandwich format, as depicted in

Scheme 4.1c, where the surface was filled with redox probe solution within the circular area defined by dual adhesive tape. Subsequently, an unmodified and freshly prepared LIG as pseudoreference/counter electrode was pasted over modified working electrode at a gap (1.8 mm) of the adhesive tape. Finally, EIS response of the immuno-surface was obtained, and results were simulated to extract R_{CT} values. Such assembly is desirable to enhance sensitivity by minimizing ohmic drop across the electrodes.^{239, 240} The label-free detection of polyGP on LIG was performed using electrochemical impedance where the sensitivity and selectivity were optimized in buffer and in commercially available human CSF media. Finally, LIG electrodes were applied to detect polyGP directly in CSF sample to discriminate C9orf72-positive and C9orf72-negative ALS.

4.2. Experimental

4.2.1. Material

Synthetic dipeptides repeat targets, i.e. Poly Glycine-Proline (Poly GP), Poly Glycine-Alanine (Poly GA), and Poly Glycine-Arginine (Poly GR), with eight peptide repeats were purchased from Life Technologies Corporation (CA, USA). Anti-Poly GP Polyclonal antibody was acquired from Millipore Sigma Corporation. Pooled Human Cerebrospinal Fluid (CSF), a product of Innovative Research Inc., was purchased from Fisher Scientific. Bovine serum albumin or BSA (lyophilized powder $\geq 96\%$), Sodium Nitrite (reagent plus $\geq 99.0\%$), and 4-Aminobenzoic acid (reagent plus $\geq 99\%$) were purchased from Sigma-Aldrich. 1-ethyl-3-(3-dimethylaminopropyl)carbodiimide (EDC) hydrochloride, *N*-hydroxysuccinimide (NHS) and [2-(*N*-morpholino)ethanesulfonic acid] (MES) 0.1 M (with 0.9% sodium chloride, pH 4.7 buffer) were purchased from Thermo Fisher Scientific. Hydrochloric acid (ACS grade) was purchased from Fisher Science Education. Potassium ferricyanide (99+%) and potassium ferrocyanide

trihydrate (99+%) were purchased from Acros Organic, while phosphate buffer saline 10× was obtained from Sigma life science. Polyimide film (Thickness 0.10 mm) on Polyethylene terephthalate (PET) substrate was obtained from Addicore (San Diego, CA). Laser printer 5th Generation Hobby Laser (20 × 12 inch) equipped with 40 W CO₂ (10.6 μm) standard laser tube, FSL100 laser fume extractor with HEPA filter and submersible water pump for laser assembly cooling was purchased from Full Spectrum Lasers (Las Vegas, NA). An optical microscope Motic 215 series with a Moticom tablet (BMW8) was purchased from Fisher Scientific. Sheet resistance was measured to confirm the formation of LIG using four-point probe, Jandel HM21 test unit purchased from Jandel Engineering Limited, England, UK. Scanning Electron Microscopy (SEM) with Energy Dispersive X-ray Spectroscopy (EDS), Quanta 450 FEG (FEI) was used to analyze LIG and E-LIG surfaces. Attenuated Total Reflectance Fourier Transform Infrared spectroscopy (ATR-FTIR) with Nicolet 6700 Spectrometer and Raman Spectroscopy with iHR 550 Horiba Scientific, wavelength 785 nm, Laser power 10 mW with objective lens X50 and 600 grooves/mm of grating have been used to characterize prepared LIG and E-LIG electrodes. Reduced graphene oxide modified screen printed carbon electrode (DRP-110RGPHOX-U50) were purchased from Metrohm USA. All electrochemical measurements were performed on Metrohm Autolab PGSTAT204 FRA32M (USA) electrochemical workstation within Metrohm Autolab Faraday cage.

4.2.2. Fabrication of laser-induced graphene electrodes.

Scheme 4.1a depicts the preparation of the LIG electrode. First, PI sheet was cut into small substrates of 3 cm × 4.5 cm dimension and then placed in laser cutter/engraver chamber in ambient condition. Then, LIG electrodes were fabricated by rastering a CO₂ laser head over polyimide film. Electrode was designed using vector graphic editor Inkscape software version

1.3. The total length of the electrode from connector to the sensing area is 2.5 cm where the working/sensing electrode is 4 mm in diameter. CO₂ laser of 10.6 μm wavelength was used for the formation of LIG electrodes using the computer-controlled laser cutting machine. A range of laser power and speed combination was used to optimize the fabrication condition. The spot size of the laser beam was ~50 μm diameter with 500 dpi setting. The laser instrument was operated using software RetinaEngrave 3D version 4.430 under raster engrave condition. The laser head rastered along the electrode length to form LIG. Then, a vinyl sheet was pasted on top of the connecting wire to passivate the connection. A square piece (3 cm × 3 cm) of dual adhesive acrylamide gel (1.8 mm thick) with a circular hole (1.5 cm dia.) was pasted over the LIG electrode as a spacer, which also holds liquid for the sandwich format. The prepared electrode was first observed by visual inspection of the whole electrode and then the working area of the electrode was observed under an optical microscope. A four-probe test unit was used to determine the sheet resistance of the prepared electrode by placing the probe on the surface of LIG. To minimize the error in measurement, three measurements were performed to determine an average value from a single electrode and at least three different electrodes were tested to obtain an average result at each condition.

4.2.3. Electrografting of LIG.

Scheme 4.1b illustrates the electrografting of the LIG electrode. The LIG working electrode was first modified with carboxyphenyl group using electrografting method. First, 2 mM solution of NaNO₂ was added into 2 mM 4-aminobenzoic acid made in 0.5 M HCl to generate a diazonium cation. After 5 min of reaction, 150 μL of the mixture was dropped onto the LIG surface. Covalent immobilization of 4-carboxyphenyl group on the LIG surface was achieved by electrografting using cyclic voltammetry (CV) from +0.6 to -0.6 V for 3 cycles at

100 mV/s scan rate. Scanning electron microscopy was performed to inspect the surface and cross-sectional morphology of the prepared LIG and E-LIG. To confirm the elemental composition of the LIG and E-LIG, electron dispersive x-ray spectroscopy (EDS) and Fourier transform infrared (FTIR) spectroscopy were performed. Surface modification of LIG and E-LIG was observed through Raman spectroscopy and cyclic voltammetry (CV).

4.2.4. Immobilization of antibody.

Scheme 4.1b also illustrates the preparation of immunosensor on the E-LIG electrode. For anti-polyGP antibody immobilization, 10 μL of 100 mM EDC and 20 mM NHS prepared in 100 mM MES buffer (pH 5) were dropped on carboxy phenyl modified LIG surface and the electrode was incubated around 8 $^{\circ}\text{C}$ for 1 h in humid condition. The surface was carefully washed with MES buffer followed by incubation of 10 μL of 20 ng/mL anti-polyGP antibodies, prepared in 1 \times PBS buffer (pH 7.4) for 3 h at 8 $^{\circ}\text{C}$ in humid condition. Then, the surface was washed with PBS buffer and exposed to 10 μL of 1% BSA as a blocking layer for 1 h followed by washing with PBS buffer. The biolayer was also exposed to 10 μL undiluted CSF for 15 min followed by washing with PBS buffer. Synthetic polyGP target in the range of 0.01 to 2 ng/mL concentration was prepared in 1 \times PBS and in CSF media separately and incubated on the biosensing platform for 15 min followed by a washing step.

4.2.5. PolyGP detection in buffer and CSF by EIS

Scheme 4.1c depicts the detection of the target on the E-LIG electrode in a sandwich format electrochemical cell. 1 mM $\text{K}_4[\text{Fe}(\text{CN})_6]/\text{K}_3[\text{Fe}(\text{CN})_6]$ (1:1) prepared in 1 \times PBS (pH 7.4) as a soluble redox probe solution ($\sim 250 \mu\text{L}$) was filled in the spacer area and then an unmodified LIG electrode as a pseudoreference/counter electrode was pasted over the modified working

electrode to form a sandwich assembly with a gap of spacer thickness. Each of the bilayer preparation steps and target immobilization steps were electrochemically characterized to confirm the modification. The EIS measurements were performed in frequency range of 100 kHz to 0.015 Hz with an applied DC potential (open circuit potential), and AC pulse of 5 mV amplitude. For simulations, Z-view version 3.5 h was used to fit the EIS data into a modified Randles equivalent circuit.

4.2.5. PolyGP detection in CSF of c9+ALS and c9-ALS patients.

Real CSF samples were collected by lumbar puncture from deceased ALS patients, received, and stored in -80 °C. Since polyGP is the biomarker of c9+ ALS patients and found absent in non c9+ ALS patients. We collected four CSF samples from c9+ and 6 samples from c9- ALS patients. 10 µL of each sample without dilution was incubated on E-LIG modified immuno surface for 15 min, washed with PBS buffer and tested using sandwich electrochemical cell as discussed above for standard samples spiked in commercial human CSF. The obtained R_{CT} signal was used to calculate concentration using equation evaluated from standard polyGP spiked concentrations in commercial human CSF. **Table 4.1** shows ALS patients' samples information, including sample ID, age range and detected concentration.

4.3. Results and Discussion

4.3.1. Fabrication of laser-induced graphene electrodes.

LIG offers sensitive and low-cost sensing platforms through an eco-friendly and all-dry method.²³⁶ Laser power and speed have a critical role in producing the sensors with mechanical durability and superior conductivity,²⁴¹⁻²⁴⁴ which might vary because of the substrate of interest and laser. To prepare durable and electrically sensitive LIG electrodes, we optimized the laser

power and speed followed by extensive characterization of the electrodes. **Figure 4.1a** shows the optical microscopic images of the part of the pristine LIG electrodes prepared by varying combination of the laser power and laser speed with the 10% increment in both directions. The optical images clearly show that low raster speed and high laser power produce brittle electrodes as well as burning of the surface, e.g. 10% speed and 90% laser power. While, low power and high speed cause incomplete carbonization, such as 20% and 30% power above 50% speed. One may notice stable LIG formation when observing diagonally between the laser power and speed as indicated by the red arrow in **Figure 4.1a**.

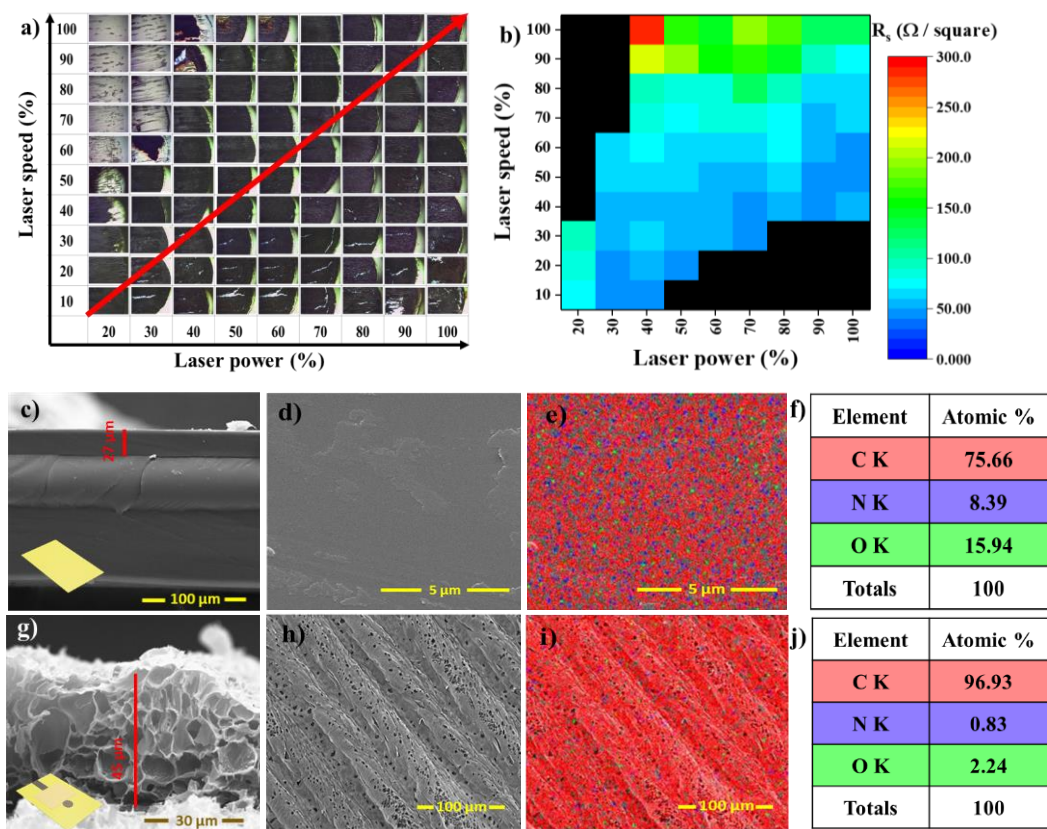


Figure 4.1. **a)** Optical images of the LIG electrodes made at different combinations of laser speed and power. **b)** Sheet resistance study of the LIG electrodes at different laser power and laser speed. **(c & g)** SEM images of PI and LIG cross section. **(d & h)** SEM of PI and LIG surface. **(e & i)** EDS of PI and LIG. **(f & j)** Elemental composition of PI and LIG, respectively. The color code given in table is to compare the false color images from EDS.

Then, electrical performance using a four-probe confirmed the graphitization of the PI after laser induction. The nonconductive nature of the PI sheet was confirmed through the resistivity $>10 \text{ M } \Omega$ per square. The resistivity of the LIG electrodes (R_s) was plotted as a heat map with respect to the combination of laser power and speed, see **Figure 4.1b**. Evidently, at any value of laser power the sheet resistance increased with the increase in laser speed. We found the best obtained sheet resistance = $43 \text{ } \Omega$ per square at 100% power – 60% speed and $44 \text{ } \Omega$ per square at 40% power – 10% speed combination. **Note:** The black area represents the brittle electrodes that peeled off once coming in contact with the probe. The scanning electron microscopy in **Figure 4.1c & 4.1d** show cross section and surface images of the PI substrate (thickness $\sim 27 \text{ } \mu\text{m}$), which confirms the smooth and featureless surface of the PI layer. While the LIG (thickness $\sim 45 \text{ } \mu\text{m}$) appears with porous morphology as observed in **Figure 4.1g & 4.1h**, where the cross-sectional area shows a sponge like structure resulting in high surface area, which may favor higher current density. The elemental composition through EDS (**Figure 4.1i & 4.1j**) clearly confirms $>20\%$ increase in carbon content and 8% loss of nitrogen and 13% loss of oxygen because of the formation of 3D network of graphitic material, as reported previously.²⁴⁵

The electrochemical performance of the LIG electrodes was confirmed using cyclic voltammetry against Ag/AgCl as reference electrode and Pt wire as counter electrode. The electrodes were tested in 1 mM $[\text{Fe}(\text{CN})_6]^{3-}/[\text{Fe}(\text{CN})_6]^{2-}$ (1:1) dissolved in $1\times$ PBS buffer. **Figure 4.2a** shows a heat map representing effect of laser power and laser speed toward the peak separation ' ΔE ' in cyclic voltammogram performed at 100 mV/s. Overall, the lowest peak separation was observed at 30% power vs. 50% speed and 30% power vs. 40% speed as highlighted in **Figure 4.2a**. **Figure 4.2b** shows CV at different scan rate from 5 - 100 mV/s on the optimized LIG (30% power vs. 50% speed).

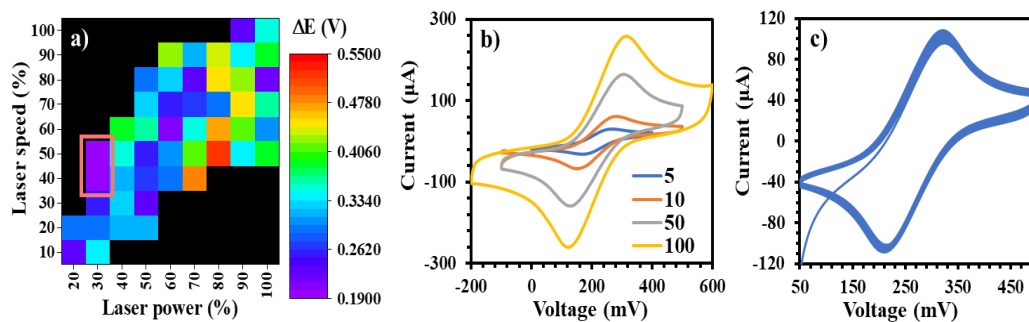


Figure 4.2. Electrochemical performance of prepared LIG electrode. **a)** Heat map showing peak separation ‘ ΔE ’ of CV performed at 100 mV/s for the electrodes prepared at different laser power and speed, orange box shows the optimal region for electrochemical performance. **b)** Cyclic voltamogram (100 cycles) of a LIG electrode obtained at 30% laser power and 50% laser speed at 10 mV/s. **c)** Cyclic voltamogram of LIG at 30% laser power and 50% laser speed performed at different scan rates 5-10 mV/s.

It is evident that ΔE increases with the scan rate, which entails that the electron transfer at LIG electrodes follow quasi-reversible system, a typical LIG behavior due to the presence of basal plane and edge defects.²⁴⁶ The electrochemical performance of the LIG electrodes, **Figure 4.2c**, shows no significant drift in the cyclic voltamogram even after 100 cycles confirming the fidelity of the LIG electrode prepared at 30% power vs. 50% speed.

4.3.2. Electrografting of LIG.

To prepare biorecognition layer for electrochemical immunosensing, some reports have adopted cross linking strategy to bind antibodies on LIG surface. In such method, AuNPs was deposited onto LIG surface followed by assembling sulfur link cross linker that binds to AuNPs at one end and covalently bind antibodies at other end via amide bond formation.^{247, 248} Another report anchored 1-pyrenebutyric acid via π -stacking and hydrophobic interactions to the laser scribed graphene (LSG) electrode followed by covalent attachment of antibodies via amide bond formation.²⁴⁹ Direct linking of antibody on LIG via amide bond formation using the native

carboxyl groups on graphitic surface has been reported.^{246, 250} However, the method may lack surface coverage of antibodies on graphitic surface, due to lack of active or functionalized sites to immobilize antibodies.²⁵¹ However, electrografting may robustly activate the graphene surface for antibody immobilization as reported previously.^{252, 253} We are reporting for the first-time electrografting of carboxyphenyl group on LIG surface to activate the surface for antibody immobilization. Electrografting allows covalent immobilization of biorecognition elements and enhances surface hydrophilicity.²⁵⁴ This process creates covalent bonds by forming aryl radicals that react with the substrate.²⁵⁵

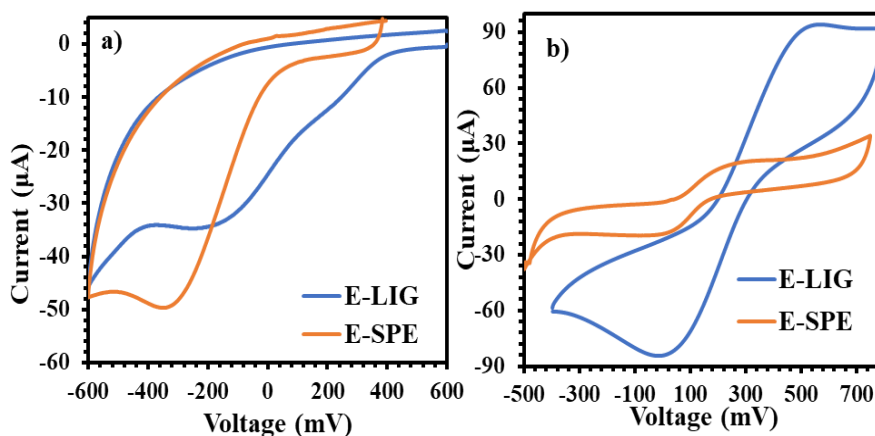


Figure 4.3. a) Electrografting of LIG and SPE b) CV response of E-LIG and E-SPE.

Figure 4.3a shows first cycle of CV of electrografting on LIG. The high current of the reduction peak at -200 mV shows successful electrografting of carboxyphenyl group on LIG surface. The FTIR spectra in **Figure 4.4a** shows LIG with no obvious peak as reported earlier.²⁵⁶ After electrografting, new peaks appeared at ~ 1200 , ~ 1700 and ~ 3500 cm^{-1} correspond to the C-O, C=O, and O-H respectively, confirming successful electrografting of the LIG surface. The formation of E-LIG was further confirmed using Raman spectroscopy, **Figure 4.4b**, where LIG

shows distinct peaks at $\sim 1300\text{ cm}^{-1}$, ~ 1550 and 2650 cm^{-1} corresponding to the D, G and 2D bands, respectively. The split in graphitic (G) peak observed after electrografting, which appears as D' band representing defects introduced in C=C basal plane confirming the covalent attachment of the organic modifiers.²⁵⁷ Electrochemical analyses of LIG and E-LIG surfaces show significant differences, **Figure 4.4c**, with high current response by LIG (i.e. $\Delta E = 189\text{ mV}$, $I_{pc} = 222\text{ }\mu\text{A}$) and five-fold decrease in current and two-fold increase in peak separation in case of E-LIG (i.e. $\Delta E = 472\text{ mV}$, $I_{pc} = 46\text{ }\mu\text{A}$), which is due to the formation of carboxyl anions on the E-LIG.

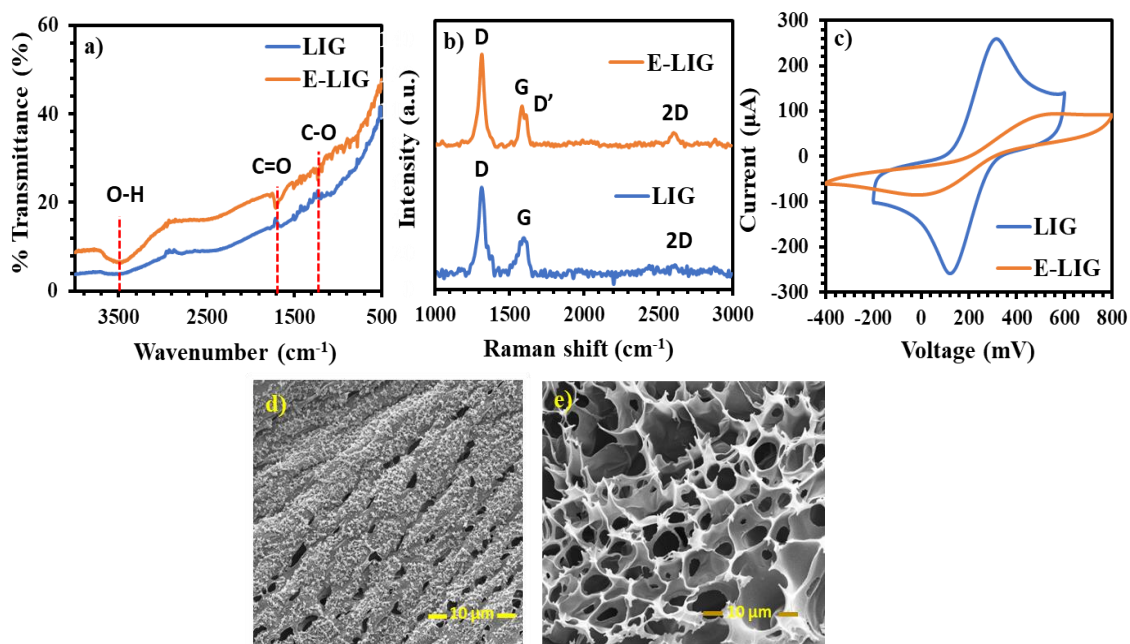


Figure 4.4. Comparison of LIG before and after electrografting. **a)** FTIR-ATR spectra, **b)** Raman spectra, **c)** Cyclic voltamograms, **d)** SEM image of LIG, and **e)** SEM image of E-LIG.

The surface morphology of LIG and E-LIG in the SEM images, **Figure 4.4d & 4.4e**, show that E-LIG surface furnishes high porosity compared to LIG, perhaps result of etching. However, such high porosity was not observed when commercial screen-printed electrodes were

treated with electrografting process (**Figure 4.5**), where we observed no obvious difference in morphology between SPE and E-SPE). Nevertheless, the high surface area of the E-LIG may improve sensitivity of the assay. It is interesting to note that the E-LIG current response is significantly higher than E-SPE as shown in **Figure 4.3b**. This is perhaps due to the higher surface area and porous network of E-LIG surface compared to E-SPE.

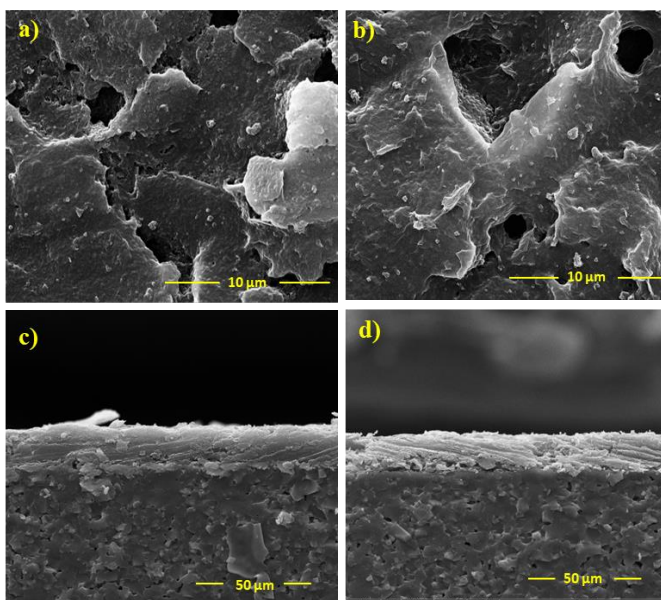


Figure 4.5. SEM micrographs of SPE before and after electrografting. **a&b)** Surface morphology and **c&d)** cross sections of SPE and E-SPE respectively.

4.3.3. Biorecognition layer on E-LIG

E-LIG surface was activated with EDC and NHS as coupling agent to covalently bind antibodies via amide linkage. Antibodies concentrations were optimized using 5, 10, 20, 50, and 75 $\mu\text{g/mL}$. The resistance to charge transfer (R_{CT}) from EIS measurements, shown in **Figure 4.6a**, were used to analyze the responses. The R_{CT} values were extracted from the Nyquist plot of EIS by fitting the data into Randles equivalent circuit as shown in **Figure 4.7**.

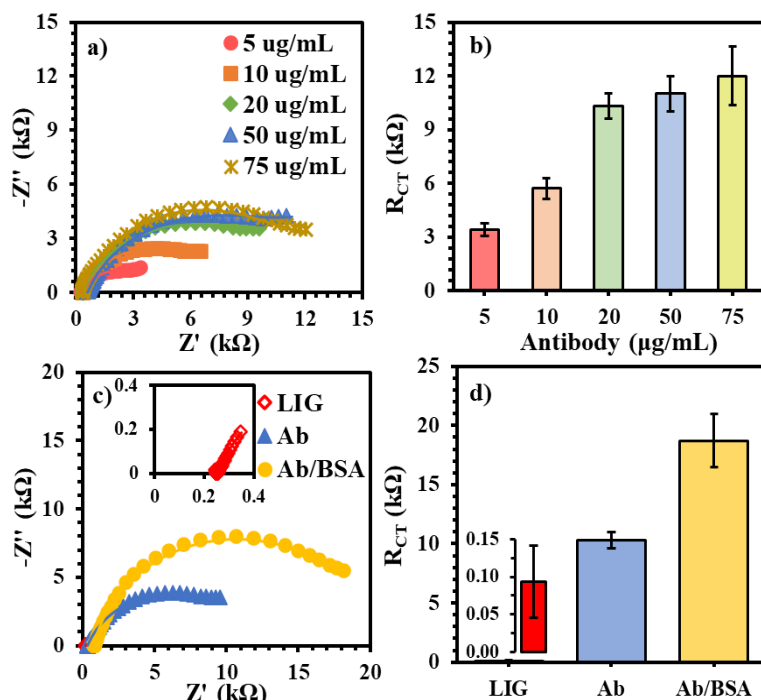


Figure 4.6. Response of biorecognition layer formation on E-LIG surface. **a)** Nyquist form of EIS plot of different concentration of anti-polyGP antibodies. **b)** Bar graph of R_{CT} versus anti-polyGP antibodies concentration. **c)** Nyquist form of EIS plots of step-by-step formation of biolayer LIG (inset), antibody and BSA after antibody to form final modification of biolayer. **d)** Shows bar graph of R_{CT} response of each layer of the biosensing interface.

The R_{CT} response increased with the antibody concentration, shown in **Figure 4.6b**, which is due to steric hindrance to diffusion of the soluble redox probe. Notably, the signal response at 10 $\mu\text{g/mL}$ was $5.7 \pm 0.6 \text{ k}\Omega$ that almost two-fold increased to $10.3 \pm 0.7 \text{ k}\Omega$ at 20 $\mu\text{g/mL}$ and did not significantly change at 50 and 75 $\mu\text{g/mL}$ concentrations given the standard error. Therefore, the optimized antibody concentration of 20 $\mu\text{g/mL}$ was used for biolayer formation in subsequent experiments. **Figure 4.6c** shows the EIS response of each layer of the biosensing interface, i.e. pristine E-LIG, after immobilization of antibody (Ab), and after the exposure of BSA to block non-specific adsorption. The R_{CT} of the biolayer (Ab/BSA) was found to be $18.7 \pm 2.2 \text{ k}\Omega$, **Figure 4.6d**. However, the R_{CT} signal of the biolayer on commercial SPE

was found to be $91.2 \pm 3.6 \text{ k}\Omega$ under same experimental conditions, see **Figure 4.8 c and d**. This can be due to the presence of high surface area and high electrochemical performance of LIG surface compared to SPE surface.

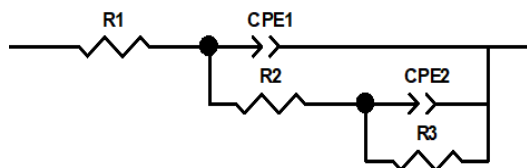


Figure 4.7. Modified Randle equivalent circuit to fit experimentally determined Nyquist form of EIS plot and to extract charge transfer resistance value R_{CT} which is determined by adding R_2 and R_3 values. $R_{CT} = R_2 + R_3$

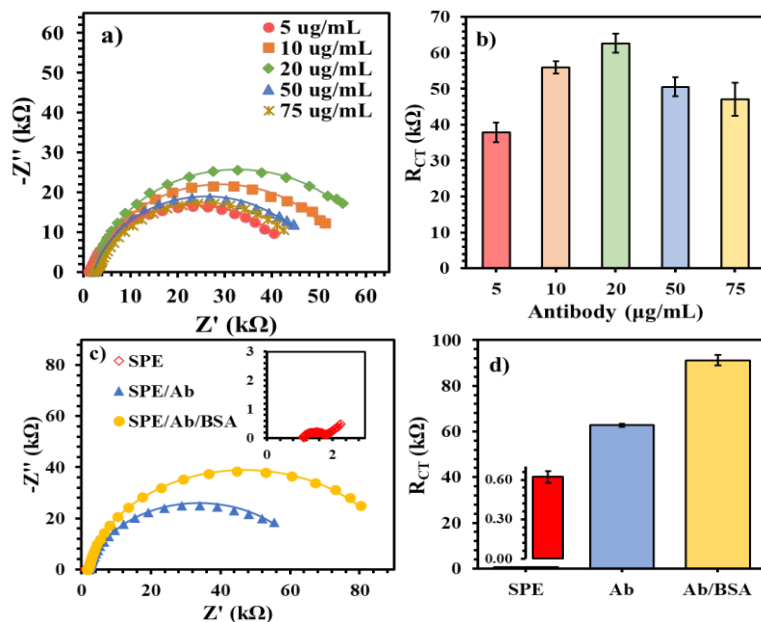


Figure 4.8. Response of biorecognition layer formation on E-SPE surface. **a)** Nyquist form of EIS plot of different concentration of anti-polyGP antibodies. **b)** Bar graph of R_{CT} versus anti-polyGP antibodies concentration. **c)** Nyquist form of EIS plots of step-by-step formation of biolayer SPE (inset), antibody and BSA after antibody to form final modification of biolayer. **d)** Shows bar graph of R_{CT} response of each layer of the biosensing interface.

4.3.4. Calibration of E-LIG sensor in buffer

The E-LIG sensor was calibrated in the range of 0.01–2 ng/mL polyGP in PBS buffer medium, as shown in **Figure 4.9a**. There, resistance increases with the increment in concentration, and the overall percent change between the lowest (0.01 ng/mL, $R_{CT} \sim 20 \pm 2.4$ k Ω) and highest concentration (2 ng/mL, $R_{CT} = 114 \pm 5.6$ k Ω) found $\sim 484\%$. The same experiment on SPE sensor, **Figure 4.9b**, shows lower amount of change between the lowest (0.01 ng/mL, $R_{CT} = 98 \pm 4.1$ k Ω) and highest concentration (2 ng/mL, $R_{CT} = 184 \pm 1.2$ k Ω) i.e., 87%, representing lower signal resolution on SPE compared with E-LIG. The calibration plots in **Figure 4.9c** evidently show lower background signal and higher sensitivity in case of E-LIG (slope = 45.601 k Ω mL/ng) compared to SPE (slope = 40.983 k Ω mL/ng) with correlation coefficients 0.995 and 0.927 respectively. The limit of detection (LOD = 3 \times Standard deviation of blank/ slope) obtained on E-LIG platform was 0.146 ng/mL, which was comparable with SPE LOD, i.e. 0.263 ng/mL. Overall, the results show E-LIG based platform has better correlation coefficient, sensitivity, and LOD.

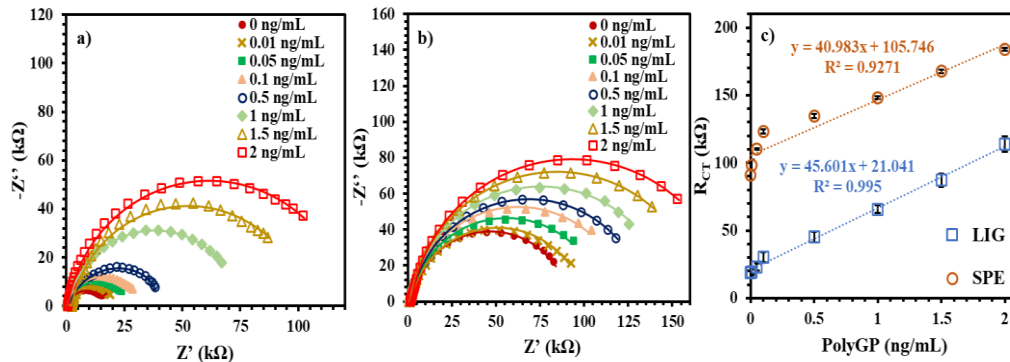


Figure 4.9. Synthetic polyGP target in buffer medium was prepared at different concentration and the response was tested through Nyquist form of EIS plot and simulation fit of the experimental results on **a)** E-LIG based platform and **b)** SPE based platform **c)** calibration plot of E-LIG based platform and SPE based platform. Error bars of each data points represents $N \geq 4$ replicates.

The specificity of the E-LIG immunoplatfrom was tested against non-specific dipeptide repeats (polyGA and polyGR) that are also present in CSF along with polyGP.^{225, 258} Specifically, polyGA and polyGR at 1 ng/mL were tested individually as shown in **Figure 4.10a**, where box and whisker plot compares R_{CT} signal against the specific and non-specific target. The results show that GA ($R_{CT} = 20 \pm 4 \text{ k}\Omega$) and GR ($R_{CT} = 20 \pm 4 \text{ k}\Omega$) respond very much like the blank with no statistical difference ($p > 0.05$). While polyGP alone and with non-specific targets shows similar response but substantially higher R_{CT} signal than blank and individual non-specific targets, i.e. GP ($R_{CT} = 66 \pm 3 \text{ k}\Omega$), GP + GA ($R_{CT} = 68 \pm 3 \text{ k}\Omega$), and GP + GR ($R_{CT} = 67 \pm 4 \text{ k}\Omega$). Single factor ANOVA finds that the response of GP is significantly not different compared to GP+GA ($p > 0.3$) and GP+GR ($p > 0.4$). Thus, the E-LIG immunoplatfrom is highly selective toward the target polyGP and essentially nonresponsive toward other interfering dipeptide repeats. While E-SPE immunoplatfrom fails T-test to distinguish between blank and GA ($p < 0.02$) and blank and GR ($p < 0.002$). Single factor ANOVA resulted that E-SPE furnishes no significant difference between GP and GP+GR ($p > 0.5$), but it shows significant difference between GP and GP+GA ($p < 0.04$). This suggested that E-SPE modified surface although distinguish the presence and absence of polyGP however the presence of interferents decrease the sensor performance by resulting high variability in the replicates. The results suggested that E-LIG based immunoplatfrom is a better alternative compared to E-SPE modified immunoplatfrom not only in terms of performance but also in terms of economy. A rough cost analysis revealed that a single A4-size PI sheet cost around \$22 which produces around 60 electrodes or 30 sandwich electrochemical systems, when including LIG production cost a single electrochemical system cost around below ~\$1, which is 10 time lower than the commercial SPE which a single unit cost around \$10.

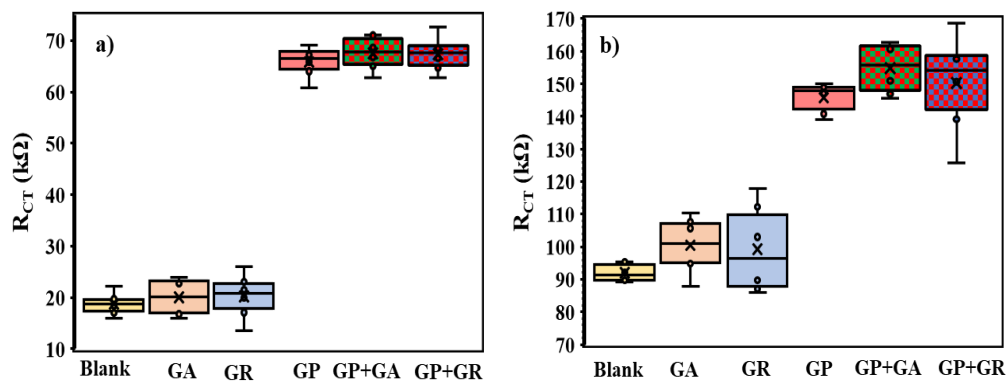


Figure 4.10. Selectivity of synthetic polyGP target in PBS buffer at 1 ng/mL in the presence and absence of interferent polyGA and polyGR each at concentration of 1 ng/mL. R_{CT} response of each EIS measurement was extracted and for each data set box and whisker plot has been plotted. **a)** Selectivity response of LIG based platform. **b)** Selectivity response of SPE based platform. (N = 6 independent replicates)

4.3.5. PolyGP detection in commercial CSF

To further evaluate the performance of the E-LIG immunosensor in complex matrix, we tested synthetic polyGP target (0.01–2 ng/mL) prepared in commercial human CSF (undiluted) and measured their EIS response as shown in **Figure 4.11a**. Preparing calibration plot in CSF matrix is useful to quantify target in more complex matrix relevant to real sample composition.^{253, 259, 260} Therefore, when testing real sample, the calibration plot must be the representative of the sample matrix. The calibration plot prepared in CSF matrix shown in **Figure 4.11b** has a correlation coefficient of 0.991, sensitivity of 40.725 kΩ mL/ng, and LOD 0.224 ng/mL. The calibration plot shows that E-LIG immunosensor is capable of quantifying polyGP in undiluted CSF sample. To test the specificity of the immunoplatfrom in CSF matrix, the same experiment was performed as shown in **Figure 4.10** above. **Figure 4.11c** shows box and whisker plot of blank exposed to CSF, 1 ng/mL polyGA and polyGR in CSF matrix. The results show that GA ($R_{CT} = 21 \pm 5$ kΩ) and GR ($R_{CT} = 22 \pm 5$ kΩ) respond similar to the blank with no statistical difference ($p > 0.1$). While polyGP with and without non-specific targets shows

considerably higher R_{CT} signal than blank and individual non-specific targets, i.e. GP ($R_{CT} = 62 \pm 6$ k Ω), GP + GA ($R_{CT} = 65 \pm 5$ k Ω), and GP + GR ($R_{CT} = 64 \pm 5$ k Ω). Single factor ANOVA suggested that GP response is not significantly different compared to GP+GA ($p > 0.3$) and GP+GR ($p > 0.5$). The E-LIG platform sustains the specificity and selectivity trend as in buffer with slightly higher standard error. The results confirm that the sensor can aptly perform in actual CSF medium obtained from ALS patient.

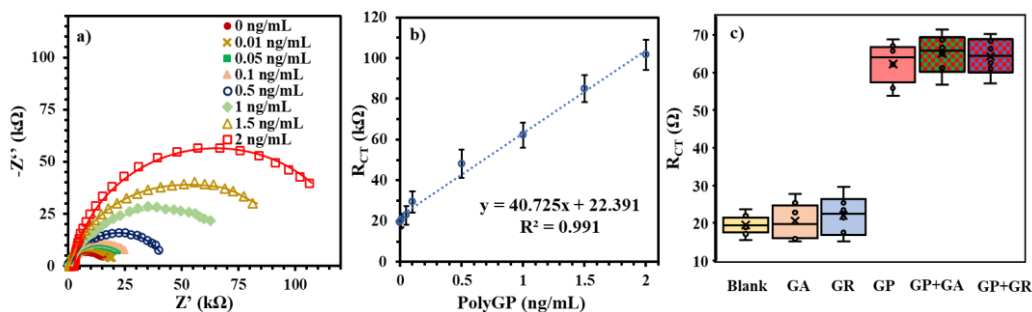


Figure 4.11. a) EIS response of polyGP target in undiluted commercial CSF. b) Calibration plot obtained in CSF matrix for concentration range of 0.01 - 2 ng/mL with $N \geq 4$ replicates. c) Box and whisker plot showing selectivity of the E-LIG platform in CSF matrix ($N = 6$).

4.3.6. PolyGP detection in ALS patient CSF.

Finally, the E-LIG immunoplatfrom was applied to test ALS patients CSF. A total of ten ALS samples were collected with four c9+ and six c9- samples. The EIS signals of c9+ samples show significantly high R_{CT} values 66.4 ± 0.4 , 75.6 ± 0.3 , 52.3 ± 6 , and 75.6 ± 5 k Ω . The R_{CT} values were used to calculate the polyGP concentration in CSF using the calibration equation obtained above (**Figure 4.11b**), which calculated the concentrations that are very close to reported values in the literature, i.e. 1.1 ± 0.1 , 1.3 ± 0.1 , 0.74 ± 0.2 , and 1.3 ± 0.1 ng/mL respectively.^{92, 225} The c9- signal is similar to the blank signal in **Figure 4.11b** and the negative concentration values in CSF in **Table 4.1** is due to the R_{CT} values of the interface slightly lower than the y-intercept of the calibration model. The results are consistent with the reported Meso Scale Discovery (MSD)

electrochemiluminescence detection technology which found presence of polyGP in c9+ ALS (median value in symptomatic 0.8 ng/mL and asymptomatic 0.5 ng/mL) and absence in c9- ALS (0.0 ng/mL) CSF samples.^{92, 225}

Table 4.1. Real ALS patients sample information with sample ID, gender, age range at the time of death, EIS signal and polyGP concentration calculated using CSF based calibration equation. In sample ID + and - signs represent c9+ ALS and c9- ALS respectively.

ID	Gender	Age range (years)	R _{ct} (kΩ)	Concentration (ng/mL)
1+	F	60-69	66.4±0.4	1.1±0.1
2+	M	70-79	75.6±0.3	1.3±0.1
3+	M	50-59	52.3±6.1	0.7±0.2
4+	M	50-59	74.9±4.9	1.3±0.1
5-	M	50-59	20.9±2.5	-0.04 ± 0.06
6-	M	60-69	20.4±2.9	-0.05±0.07
7-	F	70-79	20.9±2.7	-0.04±0.07
8-	M	70-79	22.5±3.6	0.003±0.009
9-	F	70-79	21.4±2.7	-0.03±0.07
10-	M	70-79	21.9±3.1	-0.012±0.08

4.5. Conclusion

We prepared electrografted-laser-induced graphene based electrochemical immunosensor for label free detection of c9+ neurodegenerative disease linked polyGP in c9+ ALS patients' CSF samples. An inexpensive in-house electrochemical detection system was formed by preparing and optimizing LIG electrode. LIG modified immunoplatfrom was built by first time electrografting of LIG to prepare carboxyl group functionalized E-LIG surface followed by exposing anti-polyGP antibodies to form biorecognition immunoplatfrom. The synthetic polyGP detection and selectivity in buffer shows that E-LIG based immunoplatfrom exhibits better performance compared to E-SPE which is 10 times more expensive than E-LIG. Calibration plot (LOD = 0.224 ng/mL) and specificity of polyGP spiked in commercial human CSF in the presence and absence of potentially coexisting other dipeptide proteins strongly promises that E-

LIG based immunoplatfrom can be used as tool to detect biomarkers in CSF samples without any dilution or pretreatment. On testing real ALS patients CSF samples, it was found that R_{CT} signal from c9+ ALS patients' samples was found as low as 0.74 ± 0.15 and as high as 1.31 ± 0.08 ng/mL which corresponds to the presence of polyGP in the given samples. While c9- ALS patients samples exhibit signals overlapping with the signals of commercial human CSF which represent absence of polyGP. These results show that E-LIG based platform not only quantifies polyGP in the complex CSF matrix but also distinguishes between c9+ and c9- ALS patients, which strongly suggest the potential use of the tool to use as diagnosis and gene therapy monitoring of c9+ patients. The results promise that the proposed sandwich-type E-LIG electrochemical system offers a sensitive and cost-effective tool to detect neurodegenerative biomarkers in complex biological matrices.

CHAPTER 5

CONCLUSION

The motivation of this dissertation is to develop a label-free detection method for neurodegenerative biomarkers through the utilization of highly sensitive electrochemical impedance spectroscopy technique. Since electrochemical detection may be affected by complex target and/or complex biological matrix, the research investigates the impact of complex targets on potential genosensing applications, as well as the influence of complex biomatrix on immunosensing applications. It is crucial to understand the detection capabilities of various nucleic acid microprobes towards complex secondary structures carrying target RNA, especially in the context of detecting neurodegenerative disease-linked long pathogenic tandem repeat sequence biomarkers. Additionally, there is a need to develop label free, sensitive, and cost-effective platforms for detecting biomarkers in complex biological samples to advance the development of biosensors for ND diagnosis.

Short tandem repeat sequences offer promising targets for label-free electrochemical detection of long expansions. However, their complex secondary structures, dependent on both length and sequence, can complicate interfacial charge transfer within detection platforms. Furthermore, the presence of sporadic repeats within the gene may lead to false-positive signals. We investigated the impact of secondary structures and sporadic repeats on label-free detection of short tandem repeat sequences. Three biosensing platforms were designed employing different nucleic acid microprobe backbones [deoxyribonucleic acid (DNA), peptide nucleic acid (PNA), and lock-nucleic acid (LNA)] to detect Huntington's CAG repeats in in vitro transcribed RNA sequences. Results revealed that pathogenic lengthy repeats exhibited lower signals compared to normal sequences, particularly on PNA and LNA platforms. LNA demonstrated superior

performance, distinguishing lengths at concentrations as low as 100 aM in the presence of Mg^{2+} , effectively addressing the challenge of secondary structures and sporadic repeats while specifically identifying tandem repeats. Furthermore, both PNA and LNA microprobes exhibited high specificity in detecting tandem CAG repeats, with LNA outperforming PNA in the presence of Mg^{2+} . Interestingly, LNA microprobes did not detect sporadic repeats, therefore it avoids the issue of false-positive signals. These findings suggest that LNA-based platforms hold promise for developing reliable biosensors for genetic neurodegenerative disorders.

Next, we investigated the impact of immunoassay media on the electrochemical detection of the ALS-associated neurofilament light chain (Nf-L) protein biomarker using an electrochemical impedance immunoassay. The immunoplatfrom was constructed on reduced graphene oxide screen-printed electrodes by immobilizing the anti-Nf-L antibody using the electrografting method. Two different media, buffer, and human serum were utilized to develop the immunoassay in order to compare their effects on the performance metrics and calibration models. The label-free charge transfer resistance (R_{CT}) of the immunoplatfrom served as the signal response for constructing the calibration models. Exposure of the biorecognition layer to human serum resulted in an enhanced impedance response of the biorecognition element with significantly reduced relative error. Furthermore, the calibration model developed in the serum environment demonstrated higher sensitivity and a better limit of detection (0.087 ng/mL) compared to the buffer medium (0.39 ng/mL). Both calibration models exhibited a strong correlation ($r = 0.952$) and were employed to estimate Nf-L concentration in patient serum samples. Analysis of the ALS patient samples revealed that concentrations obtained from the buffer-based regression model were higher than those from the serum-based model. However, a high Pearson correlation ($r = 1.00$) between the media suggests that concentrations in one

medium may be predictive of concentrations in the other medium. The developed immunoplatfrom offers a label-free, simple, and sensitive method for detecting Nf-L, facilitating ALS diagnosis.

Finally, we developed an in-house, inexpensive, and label-free electrochemical immunoassay for the straightforward detection of ALS linked biomarker Poly Glycine Proline (polyGP) in unprocessed cerebrospinal fluid (CSF) samples. We employed electrografting of the laser induced graphene (E-LIG) electrode system in a sandwich format for the first time to detect polyGP using label-free electrochemical impedance spectroscopy. Our findings from the synthetic polyGP detection and selectivity tests in buffer solution indicate that the E-LIG based immunoplatfrom outperforms the commercially available screen-printed electrode (E-SPE), which is ten times more expensive than E-LIG. The precision of the calibration model in CSF was superior to that in buffer solution. The calibration plot (LOD = 0.224 ng/mL) and specificity of polyGP spiked in commercial human CSF, in the presence and absence of potentially coexisting other dipeptide proteins, strongly suggest that the E-LIG based immunoplatfrom can effectively detect biomarkers in CSF samples without requiring any dilution or pretreatment. Analysis of real CSF samples from ALS patients revealed that the proposed sandwich-type E-LIG electrochemical system not only quantifies polyGP in the complex CSF matrix but also distinguishes between c9+ and c9- ALS patients, suggesting its potential utility in the diagnosis and gene therapy monitoring of c9+ patients.

Overall, this dissertation provides the development of new biosensing platforms for sensitive electrochemical detection of neurodegenerative disease. We propose that these platforms provide insight for the detection of complex biomolecule target and/or analyte in

complex biological matrix which will be applicable in detection of other biomarkers in complex biological matrices, environmental monitoring, and the development of lab on a chip devices.

REFERENCES

- (1) Wareham, L. K.; Liddelow, S. A.; Temple, S.; Benowitz, L. I.; Di Polo, A.; Wellington, C.; Goldberg, J. L.; He, Z.; Duan, X.; Bu, G.; et al. Solving neurodegeneration: common mechanisms and strategies for new treatments. *Mol Neurodegener* **2022**, *17* (1), 23. DOI: 10.1186/s13024-022-00524-0 From NLM Medline.
- (2) Wang, X.; Lu, D.; Liu, Y.; Wang, W.; Ren, R.; Li, M.; Liu, D.; Liu, Y.; Liu, Y.; Pang, G. Electrochemical Signal Amplification Strategies and Their Use in Olfactory and Taste Evaluation. *Biosensors (Basel)* **2022**, *12* (8). DOI: 10.3390/bios12080566.
- (3) Najeeb, M. A.; Ahmad, Z.; Shakoor, R. A.; Mohamed, A. M. A.; Kahraman, R. A novel classification of prostate specific antigen (PSA) biosensors based on transducing elements. *Talanta* **2017**, *168*, 52-61. DOI: 10.1016/j.talanta.2017.03.022 From NLM Medline.
- (4) Sanati, A.; Jalali, M.; Raeissi, K.; Karimzadeh, F.; Kharaziha, M.; Mahshid, S. S.; Mahshid, S. A review on recent advancements in electrochemical biosensing using carbonaceous nanomaterials. *Mikrochim Acta* **2019**, *186* (12), 773. DOI: 10.1007/s00604-019-3854-2 From NLM Medline.
- (5) Braems, E.; Swinnen, B.; Van Den Bosch, L. C9orf72 loss-of-function: a trivial, stand-alone or additive mechanism in C9 ALS/FTD? *Acta Neuropathol* **2020**, *140* (5), 625-643. DOI: 10.1007/s00401-020-02214-x.
- (6) *How CGM Works*. FreeStyle Libre by Abbott, <https://www.freestyleprovider.abbott/us-en/how-cgm-works.html> (accessed 2024 2/5/2024).
- (7) Yadav, S.; Saini, A.; Devi, R.; Lata, S. Transducers in Biosensors. In *Biomaterials-Based Sensors: Recent Advances and Applications*, Springer, 2023; pp 101-125.

- (8) Traynor, S. M.; Pandey, R.; Maclachlan, R.; Hosseini, A.; Didar, T. F.; Li, F.; Soleymani, L. Review—Recent Advances in Electrochemical Detection of Prostate Specific Antigen (PSA) in Clinically-Relevant Samples. *Journal of The Electrochemical Society* **2020**, *167* (3). DOI: 10.1149/1945-7111/ab69fd.
- (9) *StatStrip*® LAC/Hb/Hct. Nova Biomedical <https://novabiomedical.com/statstrip-lac-hb-hct/> (accessed 2024 2/5/2024).
- (10) Putzbach, W.; Ronkainen, N. J. Immobilization techniques in the fabrication of nanomaterial-based electrochemical biosensors: a review. *Sensors (Basel)* **2013**, *13* (4), 4811-4840. DOI: 10.3390/s130404811 From NLM Medline.
- (11) Ahmed, A.; Rushworth, J. V.; Hirst, N. A.; Millner, P. A. Biosensors for whole-cell bacterial detection. *Clin Microbiol Rev* **2014**, *27* (3), 631-646. DOI: 10.1128/CMR.00120-13.
- (12) Accu-Chek by Roche, <https://www.accu-chek.com/> (accessed 2024 2/4/2024).
- (13) Laidoudi, S.; Khelladi, M. R.; Lamiri, L.; Belgherbi, O.; Boudour, S.; Dehchar, C.; Boufnik, R. Non-enzymatic glucose detection based on cuprous oxide thin film synthesized via electrochemical deposition. *Applied Physics A* **2021**, *127* (3). DOI: 10.1007/s00339-021-04299-x.
- (14) Rhouati, A.; Catanante, G.; Nunes, G.; Hayat, A.; Marty, J. L. Label-Free Aptasensors for the Detection of Mycotoxins. *Sensors (Basel)* **2016**, *16* (12). DOI: 10.3390/s16122178 From NLM Medline.
- (15) IUPAC gold book. <https://goldbook.iupac.org/terms/view/B00663> (accessed 3/1/2024).
- (16) Eggins, B. R. *Biosensors: an introduction*; Springer-Verlag, 2013.
- (17) Koyun, A.; Ahlatcolu, E.; Koca, Y.; Kara, S. Biosensors and their principles. *A roadmap of biomedical engineers and milestones* **2012**, *5*, 42-117.

- (18) Bellan, L. M.; Wu, D.; Langer, R. S. Current trends in nanobiosensor technology. *Wiley Interdiscip Rev Nanomed Nanobiotechnol* **2011**, *3* (3), 229-246. DOI: 10.1002/wnan.136.
- (19) DOI: 10.1007/978-90-481-3606-3_2.
- (20) Senveli, S. U.; Tigli, O. Biosensors in the small scale: methods and technology trends. *IET Nanobiotechnol* **2013**, *7* (1), 7-21. DOI: 10.1049/iet-nbt.2012.0005.
- (21) Sang, S.; Wang, Y.; Feng, Q.; Wei, Y.; Ji, J.; Zhang, W. Progress of new label-free techniques for biosensors: a review. *Crit Rev Biotechnol* **2016**, *36* (3), 465-481. DOI: 10.3109/07388551.2014.991270.
- (22) Antiochia, R. Developments in biosensors for CoV detection and future trends. *Biosens Bioelectron* **2020**, *173*, 112777. DOI: 10.1016/j.bios.2020.112777.
- (23) Bollella, P.; Katz, E. Biosensors-Recent Advances and Future Challenges. *Sensors (Basel)* **2020**, *20* (22). DOI: 10.3390/s20226645.
- (24) Chadha, U.; Bhardwaj, P.; Agarwal, R.; Rawat, P.; Agarwal, R.; Gupta, I.; Panjwani, M.; Singh, S.; Ahuja, C.; Selvaraj, S. K.; et al. Recent progress and growth in biosensors technology: A critical review. *Journal of Industrial and Engineering Chemistry* **2022**, *109*, 21-51. DOI: 10.1016/j.jiec.2022.02.010.
- (25) Haleem, A.; Javaid, M.; Singh, R. P.; Suman, R.; Rab, S. Biosensors applications in medical field: A brief review. *Sensors International* **2021**, *2*. DOI: 10.1016/j.sintl.2021.100100.
- (26) Mehrotra, P. Biosensors and their applications - A review. *J Oral Biol Craniofac Res* **2016**, *6* (2), 153-159. DOI: 10.1016/j.jobcr.2015.12.002.
- (27) Turner, A. P. Biosensors: sense and sensibility. *Chem Soc Rev* **2013**, *42* (8), 3184-3196. DOI: 10.1039/c3cs35528d.

- (28) Fahmy, H. M.; Abu Serea, E. S.; Salah-Eldin, R. E.; Al-Hafiry, S. A.; Ali, M. K.; Shalan, A. E.; Lanceros-Mendez, S. Recent Progress in Graphene- and Related Carbon-Nanomaterial-based Electrochemical Biosensors for Early Disease Detection. *ACS Biomater Sci Eng* **2022**, *8* (3), 964-1000. DOI: 10.1021/acsbomaterials.1c00710.
- (29) Jain, S.; Nehra, M.; Kumar, R.; Dilbaghi, N.; Hu, T.; Kumar, S.; Kaushik, A.; Li, C. Z. Internet of medical things (IoMT)-integrated biosensors for point-of-care testing of infectious diseases. *Biosens Bioelectron* **2021**, *179*, 113074. DOI: 10.1016/j.bios.2021.113074.
- (30) Cui, F.; Yue, Y.; Zhang, Y.; Zhang, Z.; Zhou, H. S. Advancing Biosensors with Machine Learning. *ACS Sens* **2020**, *5* (11), 3346-3364. DOI: 10.1021/acssensors.0c01424.
- (31) Wang, C.; Liu, M.; Wang, Z.; Li, S.; Deng, Y.; He, N. Point-of-care diagnostics for infectious diseases: From methods to devices. *Nano Today* **2021**, *37*, 101092. DOI: 10.1016/j.nantod.2021.101092.
- (32) Liu, D.; Wang, J.; Wu, L.; Huang, Y.; Zhang, Y.; Zhu, M.; Wang, Y.; Zhu, Z.; Yang, C. Trends in miniaturized biosensors for point-of-care testing. *TrAC Trends in Analytical Chemistry* **2020**, *122*. DOI: 10.1016/j.trac.2019.115701.
- (33) Smith, A. A.; Li, R.; Tse, Z. T. H. Reshaping healthcare with wearable biosensors. *Sci Rep* **2023**, *13* (1), 4998. DOI: 10.1038/s41598-022-26951-z.
- (34) Asif, M.; Ajmal, M.; Ashraf, G.; Muhammad, N.; Aziz, A.; Iftikhar, T.; Wang, J.; Liu, H. The role of biosensors in coronavirus disease-2019 outbreak. *Curr Opin Electrochem* **2020**, *23*, 174-184. DOI: 10.1016/j.coelec.2020.08.011.
- (35) Ronkainen, N. J.; Halsall, H. B.; Heineman, W. R. Electrochemical biosensors. *Chem Soc Rev* **2010**, *39* (5), 1747-1763. DOI: 10.1039/b714449k.

- (36) Thevenot, D. R.; Toth, K.; Durst, R. A.; Wilson, G. S. Electrochemical biosensors: recommended definitions and classification. *Biosens Bioelectron* **2001**, *16* (1-2), 121-131. DOI: 10.1016/s0956-5663(01)00115-4.
- (37) Saxena, V.; Malhotra, B. Electrochemical biosensors. *Advances in Biosensors: Perspectives in Biosensor*. JAI Press, Stamford **2003**, 63-100.
- (38) Thakur, N.; Gupta, D.; Mandal, D.; Nagaiah, T. C. Ultrasensitive electrochemical biosensors for dopamine and cholesterol: recent advances, challenges and strategies. *Chem Commun (Camb)* **2021**, *57* (97), 13084-13113. DOI: 10.1039/d1cc05271c.
- (39) Kucherenko, I. S.; Soldatkin, O. O.; Kucherenko, D. Y.; Soldatkina, O. V.; Dzyadevych, S. V. Advances in nanomaterial application in enzyme-based electrochemical biosensors: a review. *Nanoscale Adv* **2019**, *1* (12), 4560-4577. DOI: 10.1039/c9na00491b.
- (40) Mehrvar, M.; Abdi, M. Recent developments, characteristics, and potential applications of electrochemical biosensors. *Anal Sci* **2004**, *20* (8), 1113-1126. DOI: 10.2116/analsci.20.1113.
- (41) Revathi, C. Enzymatic and nonenzymatic electrochemical biosensors. In *Fundamentals and sensing applications of 2D materials*, Elsevier, 2019; pp 259-300.
- (42) Farzin, L.; Shamsipur, M.; Samandari, L.; Sheibani, S. Advances in the design of nanomaterial-based electrochemical affinity and enzymatic biosensors for metabolic biomarkers: A review. *Mikrochim Acta* **2018**, *185* (5), 276. DOI: 10.1007/s00604-018-2820-8.
- (43) Koyappayil, A.; Lee, M. H. Ultrasensitive Materials for Electrochemical Biosensor Labels. *Sensors (Basel)* **2020**, *21* (1). DOI: 10.3390/s21010089.
- (44) Yu, C.-X.; Xiong, F.; Liu, L.-L. Electrochemical Biosensors with Silver Nanoparticles as Signal Labels. *International Journal of Electrochemical Science* **2020**, *15* (5), 3869-3890. DOI: 10.20964/2020.05.53.

- (45) Hai, X.; Li, Y.; Zhu, C.; Song, W.; Cao, J.; Bi, S. DNA-based label-free electrochemical biosensors: From principles to applications. *TrAC Trends in Analytical Chemistry* **2020**, *133*. DOI: 10.1016/j.trac.2020.116098.
- (46) Jin, B.; Wang, P.; Mao, H.; Hu, B.; Zhang, H.; Cheng, Z.; Wu, Z.; Bian, X.; Jia, C.; Jing, F.; et al. Multi-nanomaterial electrochemical biosensor based on label-free graphene for detecting cancer biomarkers. *Biosens Bioelectron* **2014**, *55*, 464-469. DOI: 10.1016/j.bios.2013.12.025.
- (47) Khanmohammadi, A.; Jalili Ghazizadeh, A.; Hashemi, P.; Afkhami, A.; Arduini, F.; Bagheri, H. An overview to electrochemical biosensors and sensors for the detection of environmental contaminants. *Journal of the Iranian Chemical Society* **2020**, *17* (10), 2429-2447. DOI: 10.1007/s13738-020-01940-z.
- (48) Negahdary, M. Electrochemical aptasensors based on the gold nanostructures. *Talanta* **2020**, *216*, 120999. DOI: 10.1016/j.talanta.2020.120999.
- (49) Yarman, A.; Scheller, F. W. How Reliable Is the Electrochemical Readout of MIP Sensors? *Sensors (Basel)* **2020**, *20* (9). DOI: 10.3390/s20092677.
- (50) Chakraborty, A.; Tibarewala, D. N.; Barui, A. Impedance-based biosensors. In *Bioelectronics and Medical Devices*, Elsevier, 2019; pp 97-122.
- (51) Magar, H. S.; Hassan, R. Y. A.; Mulchandani, A. Electrochemical Impedance Spectroscopy (EIS): Principles, Construction, and Biosensing Applications. *Sensors (Basel)* **2021**, *21* (19). DOI: 10.3390/s21196578.
- (52) Sivakumar, R.; Lee, N. Y. Recent advances in airborne pathogen detection using optical and electrochemical biosensors. *Anal Chim Acta* **2022**, *1234*, 340297. DOI: 10.1016/j.aca.2022.340297.
- (53) Chooto, P. Cyclic voltammetry and its applications. *Voltammetry. IntechOpen* **2019**, *1*.

- (54) Compton, R. G.; Banks, C. E. *Understanding voltammetry*; World Scientific, 2018.
- (55) Mirceski, V.; Skrzypek, S.; Stojanov, L. Square-wave voltammetry. *ChemTexts* **2018**, *4* (4). DOI: 10.1007/s40828-018-0073-0.
- (56) Amine, A.; Mohammadi, H. Amperometry. *Ref. Modul. Chem. Mol. Sci. Chem. Eng* **2018**, *10*.
- (57) Wang, S.; Zhang, J.; Gharbi, O.; Vivier, V.; Gao, M.; Orazem, M. E. Electrochemical impedance spectroscopy. *Nature Reviews Methods Primers* **2021**, *1* (1). DOI: 10.1038/s43586-021-00039-w.
- (58) Sezgintürk, M. K. Introduction to commercial biosensors. In *Commercial Biosensors and Their Applications*, Elsevier, 2020; pp 1-28.
- (59) Kumar, A.; Mahato, K.; Purohit, B.; Chandra, P. Commercial aspects and market pull of biosensors in diagnostic industries. In *Miniaturized Biosensing Devices: Fabrication and Applications*, Springer, 2022; pp 351-368.
- (60) Gitler, A. D.; Dhillon, P.; Shorter, J. Neurodegenerative disease: models, mechanisms, and a new hope. *Dis Model Mech* **2017**, *10* (5), 499-502. DOI: 10.1242/dmm.030205.
- (61) Ross, C. A.; Poirier, M. A. Protein aggregation and neurodegenerative disease. *Nat Med* **2004**, *10 Suppl*, S10-17. DOI: 10.1038/nm1066.
- (62) Sheinerman, K. S.; Umansky, S. R. Early detection of neurodegenerative diseases: circulating brain-enriched microRNA. *Cell Cycle* **2013**, *12* (1), 1-2. DOI: 10.4161/cc.23067.
- (63) Amyotrophic lateral sclerosis. Agency for toxic substances and disease registry. <https://www.cdc.gov/als/WhatisALS.html#:~:text=How%20many%20people%20have%20ALS, every%20year%20with%20this%20disease>. (accessed 2/17/2024).

- (64) Arthur, K. C.; Calvo, A.; Price, T. R.; Geiger, J. T.; Chio, A.; Traynor, B. J. Projected increase in amyotrophic lateral sclerosis from 2015 to 2040. *Nat Commun* **2016**, *7*, 12408. DOI: 10.1038/ncomms12408.
- (65) *WHAT IS HD*. Huntington's Disease Society of America, <https://hdsa.org/what-is-hd/overview-of-huntingtons-disease/#:~:text=HD%20is%20known%20as%20a,risk%20of%20inheriting%20the%20disease>. (accessed 2024 2/24/2024).
- (66) Medina, A.; Mahjoub, Y.; Shaver, L.; Pringsheim, T. Prevalence and Incidence of Huntington's Disease: An Updated Systematic Review and Meta-Analysis. *Mov Disord* **2022**, *37* (12), 2327-2335. DOI: 10.1002/mds.29228.
- (67) O'Leary, K. Viruses linked to neurodegenerative disease. *Nat Med* **2023**. DOI: 10.1038/d41591-023-00016-8.
- (68) Armstrong, R. What causes neurodegenerative disease? *Folia Neuropathol* **2020**, *58* (2), 93-112. DOI: 10.5114/fn.2020.96707.
- (69) Li, C.; Liu, J.; Lin, J.; Shang, H. COVID-19 and risk of neurodegenerative disorders: A Mendelian randomization study. *Transl Psychiatry* **2022**, *12* (1), 283. DOI: 10.1038/s41398-022-02052-3.
- (70) Levine, K. S.; Leonard, H. L.; Blauwendraat, C.; Iwaki, H.; Johnson, N.; Bandres-Ciga, S.; Ferrucci, L.; Faghri, F.; Singleton, A. B.; Nalls, M. A. Virus exposure and neurodegenerative disease risk across national biobanks. *Neuron* **2023**, *111* (7), 1086-1093 e1082. DOI: 10.1016/j.neuron.2022.12.029.
- (71) Hansson, O. Biomarkers for neurodegenerative diseases. *Nat Med* **2021**, *27* (6), 954-963. DOI: 10.1038/s41591-021-01382-x.

- (72) Rohilla, K. J.; Gagnon, K. T. RNA biology of disease-associated microsatellite repeat expansions. *Acta Neuropathol Commun* **2017**, *5* (1), 63. DOI: 10.1186/s40478-017-0468-y.
- (73) Schule, B.; McFarland, K. N.; Lee, K.; Tsai, Y. C.; Nguyen, K. D.; Sun, C.; Liu, M.; Byrne, C.; Gopi, R.; Huang, N.; et al. Parkinson's disease associated with pure ATXN10 repeat expansion. *NPJ Parkinsons Dis* **2017**, *3*, 27. DOI: 10.1038/s41531-017-0029-x.
- (74) DeJesus-Hernandez, M.; Mackenzie, I. R.; Boeve, B. F.; Boxer, A. L.; Baker, M.; Rutherford, N. J.; Nicholson, A. M.; Finch, N. A.; Flynn, H.; Adamson, J.; et al. Expanded GGGGCC hexanucleotide repeat in noncoding region of C9ORF72 causes chromosome 9p-linked FTD and ALS. *Neuron* **2011**, *72* (2), 245-256. DOI: 10.1016/j.neuron.2011.09.011.
- (75) MacDonald, M. E.; Barnes, G.; Srinidhi, J.; Duyao, M. P.; Ambrose, C. M.; Myers, R. H.; Gray, J.; Conneally, P. M.; Young, A.; Penney, J.; et al. Gametic but not somatic instability of CAG repeat length in Huntington's disease. *J Med Genet* **1993**, *30* (12), 982-986. DOI: 10.1136/jmg.30.12.982.
- (76) Heitz, D.; Rousseau, F.; Devys, D.; Saccone, S.; Abderrahim, H.; Le Paslier, D.; Cohen, D.; Vincent, A.; Toniolo, D.; Della Valle, G.; et al. Isolation of sequences that span the fragile X and identification of a fragile X-related CpG island. *Science* **1991**, *251* (4998), 1236-1239. DOI: 10.1126/science.2006411.
- (77) La Spada, A. R.; Wilson, E. M.; Lubahn, D. B.; Harding, A. E.; Fischbeck, K. H. Androgen receptor gene mutations in X-linked spinal and bulbar muscular atrophy. *Nature* **1991**, *352* (6330), 77-79. DOI: 10.1038/352077a0.
- (78) Orr, H. T.; Chung, M. Y.; Banfi, S.; Kwiatkowski, T. J., Jr.; Servadio, A.; Beaudet, A. L.; McCall, A. E.; Duvick, L. A.; Ranum, L. P.; Zoghbi, H. Y. Expansion of an unstable trinucleotide

CAG repeat in spinocerebellar ataxia type 1. *Nat Genet* **1993**, *4* (3), 221-226. DOI: 10.1038/ng0793-221.

(79) Knight, S. J.; Flannery, A. V.; Hirst, M. C.; Campbell, L.; Christodoulou, Z.; Phelps, S. R.; Pointon, J.; Middleton-Price, H. R.; Barnicoat, A.; Pembrey, M. E.; et al. Trinucleotide repeat amplification and hypermethylation of a CpG island in FRAXE mental retardation. *Cell* **1993**, *74* (1), 127-134. DOI: 10.1016/0092-8674(93)90300-f.

(80) Campuzano, V.; Montermini, L.; Molto, M. D.; Pianese, L.; Cossée, M.; Cavalcanti, F.; Monros, E.; Rodius, F.; Duclos, F.; Monticelli, A. Friedreich's ataxia: autosomal recessive disease caused by an intronic GAA triplet repeat expansion. *Science* **1996**, *271* (5254), 1423-1427.

(81) Kenneson, A.; Zhang, F.; Hagedorn, C. H.; Warren, S. T. Reduced FMRP and increased FMR1 transcription is proportionally associated with CGG repeat number in intermediate-length and premutation carriers. *Human molecular genetics* **2001**, *10* (14), 1449-1454.

(82) Gaetani, L.; Paolini Paoletti, F.; Bellomo, G.; Mancini, A.; Simoni, S.; Di Filippo, M.; Parnetti, L. CSF and Blood Biomarkers in Neuroinflammatory and Neurodegenerative Diseases: Implications for Treatment. *Trends Pharmacol Sci* **2020**, *41* (12), 1023-1037. DOI: 10.1016/j.tips.2020.09.011.

(83) Goldoni, R.; Dolci, C.; Boccalari, E.; Inchingolo, F.; Paghi, A.; Strambini, L.; Galimberti, D.; Tartaglia, G. M. Salivary biomarkers of neurodegenerative and demyelinating diseases and biosensors for their detection. *Ageing Res Rev* **2022**, *76*, 101587. DOI: 10.1016/j.arr.2022.101587.

(84) Brasier, N.; Eckstein, J. Sweat as a Source of Next-Generation Digital Biomarkers. *Digit Biomark* **2019**, *3* (3), 155-165. DOI: 10.1159/000504387.

- (85) Krol-Grzymala, A.; Sienkiewicz-Szlapka, E.; Fiedorowicz, E.; Rozmus, D.; Cieslinska, A.; Grzybowski, A. Tear Biomarkers in Alzheimer's and Parkinson's Diseases, and Multiple Sclerosis: Implications for Diagnosis (Systematic Review). *Int J Mol Sci* **2022**, *23* (17). DOI: 10.3390/ijms231710123.
- (86) Armenta-Castro, A.; Nunez-Soto, M. T.; Rodriguez-Aguillon, K. O.; Aguayo-Acosta, A.; Oyervides-Munoz, M. A.; Snyder, S. A.; Barcelo, D.; Saththasivam, J.; Lawler, J.; Sosa-Hernandez, J. E.; et al. Urine biomarkers for Alzheimer's disease: A new opportunity for wastewater-based epidemiology? *Environ Int* **2024**, *184*, 108462. DOI: 10.1016/j.envint.2024.108462.
- (87) Seol, W.; Kim, H.; Son, I. Urinary Biomarkers for Neurodegenerative Diseases. *Exp Neurol* **2020**, *29* (5), 325-333. DOI: 10.5607/en20042.
- (88) Robelin, L.; Gonzalez De Aguilar, J. L. Blood biomarkers for amyotrophic lateral sclerosis: myth or reality? *Biomed Res Int* **2014**, *2014*, 525097. DOI: 10.1155/2014/525097.
- (89) Jeromin, A.; Bowser, R. Biomarkers in Neurodegenerative Diseases. *Adv Neurol* **2017**, *15*, 491-528. DOI: 10.1007/978-3-319-57193-5_20.
- (90) Olsson, B.; Lautner, R.; Andreasson, U.; Öhrfelt, A.; Portelius, E.; Bjerke, M.; Hölttä, M.; Rosén, C.; Olsson, C.; Strobel, G.; et al. CSF and blood biomarkers for the diagnosis of Alzheimer's disease: a systematic review and meta-analysis. *The Lancet Neurology* **2016**, *15* (7), 673-684. DOI: 10.1016/s1474-4422(16)00070-3.
- (91) Nakamura, A.; Kaneko, N.; Villemagne, V. L.; Kato, T.; Doecke, J.; Dore, V.; Fowler, C.; Li, Q. X.; Martins, R.; Rowe, C.; et al. High performance plasma amyloid-beta biomarkers for Alzheimer's disease. *Nature* **2018**, *554* (7691), 249-254. DOI: 10.1038/nature25456.

- (92) Gendron, T. F.; Chew, J.; Stankowski, J. N.; Hayes, L. R.; Zhang, Y. J.; Prudencio, M.; Carlomagno, Y.; Daugherty, L. M.; Jansen-West, K.; Perkerson, E. A.; et al. Poly(GP) proteins are a useful pharmacodynamic marker for C9ORF72-associated amyotrophic lateral sclerosis. *Sci Transl Med* **2017**, *9* (383). DOI: 10.1126/scitranslmed.aai7866.
- (93) Gille, B.; De Schaepdryver, M.; Dedeene, L.; Goossens, J.; Claeys, K. G.; Van Den Bosch, L.; Tournoy, J.; Van Damme, P.; Poesen, K. Inflammatory markers in cerebrospinal fluid: independent prognostic biomarkers in amyotrophic lateral sclerosis? *J Neurol Neurosurg Psychiatry* **2019**, *90* (12), 1338-1346. DOI: 10.1136/jnnp-2018-319586.
- (94) Agnello, L.; Colletti, T.; Lo Sasso, B.; Vidali, M.; Spataro, R.; Gambino, C. M.; Giglio, R. V.; Piccoli, T.; Bivona, G.; La Bella, V.; et al. Tau protein as a diagnostic and prognostic biomarker in amyotrophic lateral sclerosis. *Eur J Neurol* **2021**, *28* (6), 1868-1875. DOI: 10.1111/ene.14789.
- (95) Rodrigues, F. B.; Byrne, L. M.; McColgan, P.; Robertson, N.; Tabrizi, S. J.; Zetterberg, H.; Wild, E. J. Cerebrospinal Fluid Inflammatory Biomarkers Reflect Clinical Severity in Huntington's Disease. *PLoS One* **2016**, *11* (9), e0163479. DOI: 10.1371/journal.pone.0163479.
- (96) Bjorkqvist, M.; Wild, E. J.; Thiele, J.; Silvestroni, A.; Andre, R.; Lahiri, N.; Raibon, E.; Lee, R. V.; Benn, C. L.; Soulet, D.; et al. A novel pathogenic pathway of immune activation detectable before clinical onset in Huntington's disease. *J Exp Med* **2008**, *205* (8), 1869-1877. DOI: 10.1084/jem.20080178.
- (97) Weiss, A.; Trager, U.; Wild, E. J.; Grueninger, S.; Farmer, R.; Landles, C.; Scahill, R. I.; Lahiri, N.; Haider, S.; Macdonald, D.; et al. Mutant huntingtin fragmentation in immune cells tracks Huntington's disease progression. *J Clin Invest* **2012**, *122* (10), 3731-3736. DOI: 10.1172/JCI64565.

- (98) Southwell, A. L.; Smith, S. E.; Davis, T. R.; Caron, N. S.; Villanueva, E. B.; Xie, Y.; Collins, J. A.; Ye, M. L.; Sturrock, A.; Leavitt, B. R.; et al. Ultrasensitive measurement of huntingtin protein in cerebrospinal fluid demonstrates increase with Huntington disease stage and decrease following brain huntingtin suppression. *Sci Rep* **2015**, *5*, 12166. DOI: 10.1038/srep12166.
- (99) Weiss, A.; Abramowski, D.; Bibel, M.; Bodner, R.; Chopra, V.; DiFiglia, M.; Fox, J.; Kegel, K.; Klein, C.; Grueninger, S.; et al. Single-step detection of mutant huntingtin in animal and human tissues: a bioassay for Huntington's disease. *Anal Biochem* **2009**, *395* (1), 8-15. DOI: 10.1016/j.ab.2009.08.001.
- (100) Sturmey, E.; Malaspina, A. Blood biomarkers in ALS: challenges, applications and novel frontiers. *Acta Neurol Scand* **2022**, *146* (4), 375-388. DOI: 10.1111/ane.13698.
- (101) Ayrignac, X.; Le Bars, E.; Duflos, C.; Hirtz, C.; Maleska Maceski, A.; Carra-Dalliere, C.; Charif, M.; Pinna, F.; Prin, P.; Menjot de Champfleury, N.; et al. Serum GFAP in multiple sclerosis: correlation with disease type and MRI markers of disease severity. *Sci Rep* **2020**, *10* (1), 10923. DOI: 10.1038/s41598-020-67934-2.
- (102) Heller, C.; Foiani, M. S.; Moore, K.; Convery, R.; Bocchetta, M.; Neason, M.; Cash, D. M.; Thomas, D.; Greaves, C. V.; Woollacott, I. O.; et al. Plasma glial fibrillary acidic protein is raised in progranulin-associated frontotemporal dementia. *J Neurol Neurosurg Psychiatry* **2020**, *91* (3), 263-270. DOI: 10.1136/jnnp-2019-321954.
- (103) Portelius, E.; Olsson, B.; Hoglund, K.; Cullen, N. C.; Kvartsberg, H.; Andreasson, U.; Zetterberg, H.; Sandelius, A.; Shaw, L. M.; Lee, V. M. Y.; et al. Cerebrospinal fluid neurogranin concentration in neurodegeneration: relation to clinical phenotypes and neuropathology. *Acta Neuropathol* **2018**, *136* (3), 363-376. DOI: 10.1007/s00401-018-1851-x.

- (104) Parnetti, L.; Gaetani, L.; Eusebi, P.; Paciotti, S.; Hansson, O.; El-Agnaf, O.; Mollenhauer, B.; Blennow, K.; Calabresi, P. CSF and blood biomarkers for Parkinson's disease. *Lancet Neurol* **2019**, *18* (6), 573-586. DOI: 10.1016/S1474-4422(19)30024-9.
- (105) Rowland, L. P.; Shneider, N. A. Amyotrophic lateral sclerosis. *New England Journal of Medicine* **2001**, *344* (22), 1688-1700.
- (106) Querin, G.; Biferi, M. G.; Pradat, P. F. Biomarkers for C9orf7-ALS in Symptomatic and Pre-symptomatic Patients: State-of-the-art in the New Era of Clinical Trials. *J Neuromuscul Dis* **2022**, *9* (1), 25-37. DOI: 10.3233/JND-210754.
- (107) Gendron, T. F.; van Blitterswijk, M.; Bieniek, K. F.; Daugherty, L. M.; Jiang, J.; Rush, B. K.; Pedraza, O.; Lucas, J. A.; Murray, M. E.; Desaro, P.; et al. Cerebellar c9RAN proteins associate with clinical and neuropathological characteristics of C9ORF72 repeat expansion carriers. *Acta Neuropathol* **2015**, *130* (4), 559-573. DOI: 10.1007/s00401-015-1474-4.
- (108) Su, Z.; Zhang, Y.; Gendron, T. F.; Bauer, P. O.; Chew, J.; Yang, W. Y.; Fostvedt, E.; Jansen-West, K.; Belzil, V. V.; Desaro, P.; et al. Discovery of a biomarker and lead small molecules to target r(GGGGCC)-associated defects in c9FTD/ALS. *Neuron* **2014**, *83* (5), 1043-1050. DOI: 10.1016/j.neuron.2014.07.041.
- (109) Roos, R. A. Huntington's disease: a clinical review. *Orphanet J Rare Dis* **2010**, *5*, 40. DOI: 10.1186/1750-1172-5-40.
- (110) McColgan, P.; Tabrizi, S. J. Huntington's disease: a clinical review. *Eur J Neurol* **2018**, *25* (1), 24-34. DOI: 10.1111/ene.13413.
- (111) Tabrizi, S. J.; Flower, M. D.; Ross, C. A.; Wild, E. J. Huntington disease: new insights into molecular pathogenesis and therapeutic opportunities. *Nat Rev Neurol* **2020**, *16* (10), 529-546. DOI: 10.1038/s41582-020-0389-4.

- (112) Pandey, M.; Rajamma, U. Huntington's disease: the coming of age. *Journal of Genetics* **2018**, *97* (3), 649-664. DOI: 10.1007/s12041-018-0957-1.
- (113) Rodrigues, F. B.; Byrne, L. M.; Wild, E. J. Biofluid Biomarkers in Huntington's Disease. *Methods Mol Biol* **2018**, *1780*, 329-396. DOI: 10.1007/978-1-4939-7825-0_17.
- (114) Cammack, A. J.; Atassi, N.; Hyman, T.; van den Berg, L. H.; Harms, M.; Baloh, R. H.; Brown, R. H.; van Es, M. A.; Veldink, J. H.; de Vries, B. S.; et al. Prospective natural history study of C9orf72 ALS clinical characteristics and biomarkers. *Neurology* **2019**, *93* (17), e1605-e1617. DOI: 10.1212/WNL.00000000000008359.
- (115) Freischmidt, A.; Muller, K.; Zondler, L.; Weydt, P.; Volk, A. E.; Bozic, A. L.; Walter, M.; Bonin, M.; Mayer, B.; von Arnim, C. A.; et al. Serum microRNAs in patients with genetic amyotrophic lateral sclerosis and pre-manifest mutation carriers. *Brain* **2014**, *137* (Pt 11), 2938-2950. DOI: 10.1093/brain/awu249.
- (116) Chen, X.; Ba, Y.; Ma, L.; Cai, X.; Yin, Y.; Wang, K.; Guo, J.; Zhang, Y.; Chen, J.; Guo, X.; et al. Characterization of microRNAs in serum: a novel class of biomarkers for diagnosis of cancer and other diseases. *Cell Res* **2008**, *18* (10), 997-1006. DOI: 10.1038/cr.2008.282.
- (117) De Felice, B.; Annunziata, A.; Fiorentino, G.; Borra, M.; Biffali, E.; Coppola, C.; Cotrufo, R.; Brettschneider, J.; Giordana, M. L.; Dalmay, T.; et al. miR-338-3p is over-expressed in blood, CFS, serum and spinal cord from sporadic amyotrophic lateral sclerosis patients. *Neurogenetics* **2014**, *15* (4), 243-253. DOI: 10.1007/s10048-014-0420-2.
- (118) Hishizawa, M.; Yamashita, H.; Akizuki, M.; Urushitani, M.; Takahashi, R. TDP-43 levels are higher in platelets from patients with sporadic amyotrophic lateral sclerosis than in healthy controls. *Neurochem Int* **2019**, *124*, 41-45. DOI: 10.1016/j.neuint.2018.12.009.

- (119) Welton, T.; Maller, J. J.; Lebel, R. M.; Tan, E. T.; Rowe, D. B.; Grieve, S. M. Diffusion kurtosis and quantitative susceptibility mapping MRI are sensitive to structural abnormalities in amyotrophic lateral sclerosis. *Neuroimage Clin* **2019**, *24*, 101953. DOI: 10.1016/j.nicl.2019.101953.
- (120) Bede, P.; Chipika, R. H.; Finegan, E.; Li Hi Shing, S.; Doherty, M. A.; Hengeveld, J. C.; Vajda, A.; Hutchinson, S.; Donaghy, C.; McLaughlin, R. L.; et al. Brainstem pathology in amyotrophic lateral sclerosis and primary lateral sclerosis: A longitudinal neuroimaging study. *Neuroimage Clin* **2019**, *24*, 102054. DOI: 10.1016/j.nicl.2019.102054.
- (121) Ikawa, M.; Okazawa, H.; Yoneda, M. [Positron Emission Tomography Imaging for Oxidative Stress in Mitochondrial and Neurodegenerative Diseases]. *Brain Nerve* **2019**, *71* (2), 161-166. DOI: 10.11477/mf.1416201236.
- (122) Ostachowicz, B.; Lankosz, M.; Tomik, B.; Adamek, D.; Wobrauschek, P.; Strelci, C.; Kregsamer, P. Analysis of some chosen elements of cerebrospinal fluid and serum in amyotrophic lateral sclerosis patients by total reflection X-ray fluorescence. *Spectrochimica Acta Part B: Atomic Spectroscopy* **2006**, *61* (10-11), 1210-1213. DOI: 10.1016/j.sab.2006.08.008.
- (123) Vielhaber, S.; Winkler, K.; Kirches, E.; Kunz, D.; Büchner, M.; Feistner, H.; Elger, C. E.; Ludolph, A. C.; Riepe, M. W.; Kunz, W. S. Visualization of defective mitochondrial function in skeletal muscle fibers of patients with sporadic amyotrophic lateral sclerosis. *Journal of the Neurological Sciences* **1999**, *169* (1-2), 133-139. DOI: 10.1016/s0022-510x(99)00236-1.
- (124) Abdolvahabi, A.; Shi, Y.; Chuprin, A.; Rasouli, S.; Shaw, B. F. Stochastic Formation of Fibrillar and Amorphous Superoxide Dismutase Oligomers Linked to Amyotrophic Lateral Sclerosis. *ACS Chem Neurosci* **2016**, *7* (6), 799-810. DOI: 10.1021/acchemneuro.6b00048.

- (125) Bellmann, J.; Goswami, R. Y.; Girardo, S.; Rein, N.; Hosseinzadeh, Z.; Hicks, M. R.; Busskamp, V.; Pyle, A. D.; Werner, C.; Sternecker, J. A customizable microfluidic platform for medium-throughput modeling of neuromuscular circuits. *Biomaterials* **2019**, *225*, 119537. DOI: 10.1016/j.biomaterials.2019.119537.
- (126) Taki, M.; Rohilla, K. J.; Barton, M.; Funneman, M.; Benzabeh, N.; Naphade, S.; Ellerby, L. M.; Gagnon, K. T.; Shamsi, M. H. Novel probes for label-free detection of neurodegenerative GGGGCC repeats associated with amyotrophic lateral sclerosis. *Anal Bioanal Chem* **2019**, *411* (26), 6995-7003. DOI: 10.1007/s00216-019-02075-8.
- (127) Li, W.-t.; Dong, S.-y.; Chen, H.; An, Y.-q.; Zhang, J.; Wang, L.-y.; Zhu, J.-J. A neurofilament-light chains electrochemical immunosensor expected to reveal the early stage of neurodegenerative diseases. *Chemical Engineering Journal* **2022**, *446*. DOI: 10.1016/j.cej.2022.136850.
- (128) Zhou, S.; Liu, D.; Chen, J.; Xiang, C.; Xiang, J.; Yang, M. Electrochemical Quantitation of the Glycosylation Level of Serum Neurofilament Light Chain for the Diagnosis of Neurodegeneration: An Interface-Solution Dual-Path Amplification Strategy. *Anal Chem* **2022**, *94* (32), 11433-11440. DOI: 10.1021/acs.analchem.2c02753.
- (129) Masud, M. K.; Mahmudunnabi, R. G.; Aziz, N. B.; Stevens, C. H.; Do-Ha, D.; Yang, S.; Blair, I. P.; Hossain, M. S. A.; Shim, Y. B.; Ooi, L.; et al. Sensitive Detection of Motor Neuron Disease Derived Exosomal miRNA Using Electrocatalytic Activity of Gold-Loaded Superparamagnetic Ferric Oxide Nanocubes. *ChemElectroChem* **2020**, *7* (16), 3459-3467. DOI: 10.1002/celec.202000828.
- (130) Muse, Q. Challenges of connecting to care for neurodegenerative conditions. *Penn Medicine News*, 12/8/2023, 2023. <https://www.pennmedicine.org/news/publications-and-special->

[projects/penn-medicine-magazine/fall-winter-2023/challenges-of-connecting-to-care-for-neurodegenerative-conditions#:~:text=There%20is%20no%20cure%20for,or%20control%20their%20body%20movements](https://www.pennmedicine.org/press-releases/2023/11/15/challenges-of-connecting-to-care-for-neurodegenerative-conditions#:~:text=There%20is%20no%20cure%20for,or%20control%20their%20body%20movements). (accessed 3/4/2024).

(131) Ghosh, R.; Tabrizi, S. J. Huntington disease. *Handb Clin Neurol* **2018**, *147*, 255-278. DOI: 10.1016/B978-0-444-63233-3.00017-8.

(132) Wijesekera, L. C.; Nigel Leigh, P. Amyotrophic lateral sclerosis. *Orphanet journal of rare diseases* **2009**, *4* (1), 1-22.

(133) Sin, M. L.; Mach, K. E.; Wong, P. K.; Liao, J. C. Advances and challenges in biosensor-based diagnosis of infectious diseases. *Expert Rev Mol Diagn* **2014**, *14* (2), 225-244. DOI: 10.1586/14737159.2014.888313.

(134) Wu, Y.; Tilley, R. D.; Gooding, J. J. Challenges and Solutions in Developing Ultrasensitive Biosensors. *J Am Chem Soc* **2019**, *141* (3), 1162-1170. DOI: 10.1021/jacs.8b09397.

(135) Masson, J. F. Consideration of Sample Matrix Effects and "Biological" Noise in Optimizing the Limit of Detection of Biosensors. *ACS Sens* **2020**, *5* (11), 3290-3292. DOI: 10.1021/acssensors.0c02254.

(136) Richards, D. A.; deMello, A. J. The Matrix Reiterated. *ACS Sens* **2023**, *8* (11), 3986-3987. DOI: 10.1021/acssensors.3c02303.

(137) Liu, G. Grand Challenges in Biosensors and Biomolecular Electronics. *Front Bioeng Biotechnol* **2021**, *9*, 707615. DOI: 10.3389/fbioe.2021.707615.

(138) Adil, O.; Shamsi, M. H. Electrochemical Impedance Immunoassay for ALS-Associated Neurofilament Protein: Matrix Effect on the Immunoplatfrom. *Biosensors (Basel)* **2023**, *13* (2). DOI: 10.3390/bios13020247 From NLM Medline.

- (139) Adil, O.; Eddington, S. B.; Gagnon, K. T.; Shamsi, M. H. Microprobes for Label-Free Detection of Short Tandem Repeats: An Insight into Alleviating Secondary Structure Effects. *Anal Chem* **2023**, *95* (36), 13528-13536. DOI: 10.1021/acs.analchem.3c01886 From NLM Medline.
- (140) Depienne, C.; Mandel, J. L. 30 years of repeat expansion disorders: What have we learned and what are the remaining challenges? *Am J Hum Genet* **2021**, *108* (5), 764-785. DOI: 10.1016/j.ajhg.2021.03.011 From NLM.
- (141) Rackus, D. G.; Shamsi, M. H.; Wheeler, A. R. Electrochemistry, biosensors and microfluidics: a convergence of fields. *Chem. Soc. Rev.* **2015**, *44*, 5320-5340.
- (142) Chen, S.; Shamsi, M. H. Biosensors-on-Chip: A Topical Review. *Journal of Micromechanics and Microengineering* **2017**, *27* (8), 083001-083015.
- (143) Asefifeyzabadi, N.; Alkhaldi, R.; Qamar, A. Z.; Pater, A. A.; Patwardhan, M.; Gagnon, K. T.; Talapatra, S.; Shamsi, M. H. Label-free Electrochemical Detection of CGG Repeats on Inkjet Printable 2D Layers of MoS₂. *ACS Applied Materials & Interfaces* **2020**, *12* (46), 52156-52165. DOI: 10.1021/acsami.0c14912.
- (144) Asefifeyzabadi, N.; Holland, T. E.; Sivakumar, P.; Talapatra, S.; Senanayake, I. M.; Goodson, B. M.; Shamsi, M. H. Sequence-Independent DNA Adsorption on Few-Layered Oxygen-Functionalized Graphene Electrodes: An Electrochemical Study for Biosensing Application. *Biosensors* **2021**, *11* (8), 273.
- (145) Liu, Y. L.; Li, J.; Chang, G.; Zhu, R. Z.; He, H. P.; Zhang, X. H.; Wang, S. F. A novel electrochemical method based on screen-printed electrodes and magnetic beads for detection of trinucleotide repeat sequence d(CAG)(n). *New J Chem* **2018**, *42* (12), 9757-9763. DOI: 10.1039/c8nj00443a.

- (146) Zhu, X. Q.; Li, J.; Lv, H. H.; He, H. P.; Liu, H.; Zhang, X. H.; Wang, S. F. Synthesis and characterization of a bifunctional nanoprobe for CGG trinucleotide repeat detection. *Rsc Advances* **2017**, *7* (57), 36124-36131. DOI: 10.1039/c7ra05268e.
- (147) Li, J.; Liu, Y.; Zhu, X.; Chang, G.; He, H.; Zhang, X.; Wang, S. A Novel Electrochemical Biosensor Based on a Double-Signal Technique for d(CAG)_n Trinucleotide Repeats. *ACS Appl Mater Interfaces* **2017**, *9* (50), 44231-44240. DOI: 10.1021/acsami.7b15014 From NLM.
- (148) Fojta, M.; Havran, L.; Vojtiskova, M.; Palecek, E. Electrochemical detection of DNA triplet repeat expansion. *J Am Chem Soc* **2004**, *126* (21), 6532-6533. DOI: 10.1021/ja048781h.
- (149) Miroslav, F.; Petra, B.; Kateřina, C.; Petr, P. A Single-Surface Electrochemical Biosensor for the Detection of DNA Triplet Repeat Expansion. *Electroanalysis* **2006**, *18* (2), 141-151. DOI: doi:10.1002/elan.200503379.
- (150) Yang, I. V.; Thorp, H. H. Modification of indium tin oxide electrodes with repeat polynucleotides: electrochemical detection of trinucleotide repeat expansion. *Anal Chem* **2001**, *73* (21), 5316-5322.
- (151) Asefifeyzabadi, N.; Durocher, G.; Tshilenge, K.-T.; Ellerby, L.; Shamsi, M. PNA microprobe for label-free detection of expanded trinucleotide repeats. *Rsc Advances* **2022**, *12*, 7757–7761.
- (152) Taki, M.; Rohilla, K. J.; Barton, M.; Funneman, M.; Benzabeh, N.; Naphade, S.; Ellerby, L. M.; Gagnon, K. T.; Shamsi, M. H. Novel probes for label-free detection of neurodegenerative GGGGCC repeats associated with amyotrophic lateral sclerosis. *Analytical and Bioanalytical Chemistry* **2019**, *411* (26), 6995-7003.
- (153) Kartje, Z. J.; Janis, H. I.; Mukhopadhyay, S.; Gagnon, K. T. Revisiting T7 RNA polymerase transcription in vitro with the Broccoli RNA aptamer as a simplified real-time

fluorescent reporter. *J Biol Chem* **2021**, *296*, 100175. DOI: 10.1074/jbc.RA120.014553 From NLM.

(154) Gagnon, K. T.; Pendergraft, H. M.; Deleavey, G. F.; Swayze, E. E.; Potier, P.; Randolph, J.; Roesch, E. B.; Chattopadhyaya, J.; Damha, M. J.; Bennett, C. F.; et al. Allele-selective inhibition of mutant huntingtin expression with antisense oligonucleotides targeting the expanded CAG repeat. *Biochemistry* **2010**, *49* (47), 10166-10178. DOI: 10.1021/bi101208k From NLM.

(155) Reuter, J.; Watson, R.; group, M. *RNA structure*.

<https://rna.urmc.rochester.edu/RNAstructureWeb/Servers/Predict1/Example.php> (accessed 2022 5/5/2022).

(156) RNAComposer: Automated RNA structure 3D modeling server.

<https://rnacomposer.cs.put.poznan.pl/> (accessed 7/6/2022).

(157) Kelley, S. O.; Jackson, N. M.; Hill, M. G.; Barton, J. K. Long-Range Electron Transfer through DNA Films. *Angewandte Chemie International Edition* **1999**, *38* (7), 941-945. DOI: [https://doi.org/10.1002/\(SICI\)1521-3773\(19990401\)38:7<941::AID-ANIE941>3.0.CO;2-7](https://doi.org/10.1002/(SICI)1521-3773(19990401)38:7<941::AID-ANIE941>3.0.CO;2-7).

(158) Paleček, E.; Fojta, M.; Tomschik, M.; Wang, J. Electrochemical biosensors for DNA hybridization and DNA damage. *Biosensors and Bioelectronics* **1998**, *13* (6), 621-628. DOI: [https://doi.org/10.1016/S0956-5663\(98\)00017-7](https://doi.org/10.1016/S0956-5663(98)00017-7).

(159) Xiao, Y.; Lai, R. Y.; Plaxco, K. W. Preparation of electrode-immobilized, redox-modified oligonucleotides for electrochemical DNA and aptamer-based sensing. *Nature Protocols* **2007**, *2* (11), 2875-2880. DOI: 10.1038/nprot.2007.413.

(160) Wong, E. L. S.; Gooding, J. J. Charge Transfer through DNA: A Selective Electrochemical DNA Biosensor. *Analytical Chemistry* **2006**, *78* (7), 2138-2144. DOI: 10.1021/ac0509096.

- (161) Long, Y.-T.; Li, C.-Z.; Sutherland, T. C.; Kraatz, H.-B.; Lee, J. S. Electrochemical Detection of Single-Nucleotide Mismatches: Application of M-DNA. *Analytical Chemistry* **2004**, *76* (14), 4059-4065. DOI: 10.1021/ac049482d.
- (162) Erdem, A.; Meric, B.; Kerman, K.; Dalbasti, T.; Ozsoz, M. Detection of Interaction Between Metal Complex Indicator and DNA by Using Electrochemical Biosensor. *Electroanalysis* **1999**, *11* (18), 1372-1376. DOI: [https://doi.org/10.1002/\(SICI\)1521-4109\(199912\)11:18<1372::AID-ELAN1372>3.0.CO;2-4](https://doi.org/10.1002/(SICI)1521-4109(199912)11:18<1372::AID-ELAN1372>3.0.CO;2-4).
- (163) Bizzotto, D.; Burgess, I. J.; Doneux, T.; Sagara, T.; Yu, H.-Z. Beyond Simple Cartoons: Challenges in Characterizing Electrochemical Biosensor Interfaces. *ACS Sensors* **2018**, *3* (1), 5-12. DOI: 10.1021/acssensors.7b00840.
- (164) Wang, J.; Palecek, E.; Nielsen, P. E.; Rivas, G.; Cai, X.; Shiraishi, H.; Dontha, N.; Luo, D.; Farias, P. A. M. Peptide Nucleic Acid Probes for Sequence-Specific DNA Biosensors. *Journal of the American Chemical Society* **1996**, *118* (33), 7667-7670. DOI: 10.1021/ja9608050.
- (165) Obika, S.; Nanbu, D.; Hari, Y.; Morio, K.-i.; In, Y.; Ishida, T.; Imanishi, T. Synthesis of 2'-O,4'-C-methyleneuridine and -cytidine. Novel bicyclic nucleosides having a fixed C3, -endo sugar pucker. *Tetrahedron Letters* **1997**, *38* (50), 8735-8738. DOI: [https://doi.org/10.1016/S0040-4039\(97\)10322-7](https://doi.org/10.1016/S0040-4039(97)10322-7).
- (166) Koshkin, A. A.; Rajwanshi, V. K.; Wengel, J. Novel convenient syntheses of LNA [2.2.1]bicyclo nucleosides. *Tetrahedron Letters* **1998**, *39* (24), 4381-4384. DOI: [https://doi.org/10.1016/S0040-4039\(98\)00706-0](https://doi.org/10.1016/S0040-4039(98)00706-0).
- (167) Briones, C.; Moreno, M. Applications of peptide nucleic acids (PNAs) and locked nucleic acids (LNAs) in biosensor development. *Analytical and Bioanalytical Chemistry* **2012**, *402* (10), 3071-3089. DOI: 10.1007/s00216-012-5742-z.

- (168) Shamsi, M. H.; Kraatz, H.-B. The effects of oligonucleotide overhangs on the surface hybridization in DNA films: an impedance study. *Analyst* **2011**, *136* (15), 3107-3112.
- (169) Bin, X.; Kraatz, H.-B. Interaction of metal ions and DNA films on gold surfaces: an electrochemical impedance study. *Analyst* **2009**, *134* (7), 1309-1313, 10.1039/B821670C. DOI: 10.1039/B821670C.
- (170) Gao, L.; Li, C.; Li, X.; Kraatz, H.-B. Electrochemical impedance study of the interaction of metal ions with unlabeled PNA. *Chemical Communications* **2010**, *46* (34), 6344. DOI: 10.1039/c0cc00986e.
- (171) Li, C.; Li, X.; Liu, X.; Kraatz, H.-B. Exploiting the Interaction of Metal Ions and Peptide Nucleic Acids–DNA Duplexes for the Detection of a Single Nucleotide Mismatch by Electrochemical Impedance Spectroscopy. *Analytical Chemistry* **2010**, *82* (3), 1166-1169. DOI: 10.1021/ac902813y.
- (172) Kerman, K.; Vestergaard, M. D.; Nagatani, N.; Takamura, Y.; Tamiya, E. Electrochemical Genosensor Based on Peptide Nucleic Acid-Mediated PCR and Asymmetric PCR Techniques: Electrostatic Interactions with a Metal Cation. *Analytical Chemistry* **2006**, *78* (7), 2182-2189. DOI: 10.1021/ac051526a.
- (173) Barluenga, S.; Winssinger, N. PNA as a Biosupramolecular Tag for Programmable Assemblies and Reactions. *Accounts of Chemical Research* **2015**, *48* (5), 1319-1331. DOI: 10.1021/acs.accounts.5b00109.
- (174) Raoof, J. B.; Ojani, R.; Golabi, S. M.; Hamidi-Asl, E.; Hejazi, M. S. Preparation of an electrochemical PNA biosensor for detection of target DNA sequence and single nucleotide mutation on p53 tumor suppressor gene corresponding oligonucleotide. *Sensors and Actuators B: Chemical* **2011**, *157* (1), 195-201. DOI: <https://doi.org/10.1016/j.snb.2011.03.049>.

- (175) Hejazi , M. S.; Pournaghi-Azar, M. H.; Alipour, E.; Abdolahinia, E. D.; Arami, S.; Navvah, H. Development of a Novel Electrochemical Biosensor for Detection and Discrimination of DNA Sequence and Single Base Mutation in dsDNA Samples Based on PNA-dsDNA Hybridization – a new Platform Technology. *Electroanalysis* **2011**, *23* (2), 503-511. DOI: <https://doi.org/10.1002/elan.201000413>.
- (176) Bartold, K.; Pietrzyk-Le, A.; Golebiewska, K.; Lisowski, W.; Caeteruccio, S.; Licandro, E.; D'Souza, F.; Kutner, W. Oligonucleotide Determination via Peptide Nucleic Acid Macromolecular Imprinting in an Electropolymerized CG-Rich Artificial Oligomer Analogue. *ACS Applied Materials & Interfaces* **2018**, *10* (33), 27562-27569. DOI: 10.1021/acsami.8b09296.
- (177) Mirkin, S. M. DNA structures, repeat expansions and human hereditary disorders. *Curr Opin Struct Biol* **2006**, *16* (3), 351-358. DOI: 10.1016/j.sbi.2006.05.004 From NLM.
- (178) Almeida, B.; Fernandes, S.; Abreu, I.; Macedo-Ribeiro, S. Trinucleotide Repeats: A Structural Perspective. *Frontiers in Neurology* **2013**, *4*, Review. DOI: 10.3389/fneur.2013.00076.
- (179) Pan, F.; Zhang, Y.; Xu, P.; Man, V. H.; Roland, C.; Weninger, K.; Sagui, C. Molecular conformations and dynamics of nucleotide repeats associated with neurodegenerative diseases: double helices and CAG hairpin loops. *Computational and Structural Biotechnology Journal* **2021**, *19*, 2819-2832. DOI: <https://doi.org/10.1016/j.csbj.2021.04.037>.
- (180) Krzyzosiak, W. J.; Sobczak, K.; Wojciechowska, M.; Fiszer, A.; Mykowska, A.; Kozlowski, P. Triplet repeat RNA structure and its role as pathogenic agent and therapeutic target. *Nucleic Acids Res* **2012**, *40* (1), 11-26. DOI: 10.1093/nar/gkr729 From NLM.
- (181) Kiliszek, A.; Rypniewski, W. Structural studies of CNG repeats. *Nucleic Acids Res* **2014**, *42* (13), 8189-8199. DOI: 10.1093/nar/gku536 From NLM.

- (182) Dodd, D. W.; Tomchick, D. R.; Corey, D. R.; Gagnon, K. T. Pathogenic C9ORF72 Antisense Repeat RNA Forms a Double Helix with Tandem C:C Mismatches. *Biochemistry* **2016**, *55* (9), 1283-1286. DOI: 10.1021/acs.biochem.6b00136 From NLM.
- (183) Manning, G. S. The molecular theory of polyelectrolyte solutions with applications to the electrostatic properties of polynucleotides. *Q Rev Biophys* **1978**, *11* (2), 179-246. DOI: 10.1017/s0033583500002031 From NLM.
- (184) Spiro, C.; Pelletier, R.; Rolfsmeier, M. L.; Dixon, M. J.; Lahue, R. S.; Gupta, G.; Park, M. S.; Chen, X.; Mariappan, S. S.; McMurray, C. T. Inhibition of FEN-1 processing by DNA secondary structure at trinucleotide repeats. *Molecular cell* **1999**, *4* (6), 1079-1085.
- (185) Richard, G.-F.; Kerrest, A.; Dujon, B. Comparative genomics and molecular dynamics of DNA repeats in eukaryotes. *Microbiology and molecular biology reviews* **2008**, *72* (4), 686-727.
- (186) *Amyotrophic Lateral Sclerosis (ALS) Fact Sheet*. National Institute of Health Office of Neuroscience Communications and Engagement
National Institute of Neurological Disorders and Stroke, <https://www.ninds.nih.gov/amyotrophic-lateral-sclerosis-als-fact-sheet#:~:text=There%20is%20no%20single%20test,to%20rule%20out%20other%20diseases> (accessed 2022 9/28/2022).
- (187) Staats, K. A.; Borchelt, D. R.; Tansey, M. G.; Wymer, J. Blood-based biomarkers of inflammation in amyotrophic lateral sclerosis. *Mol Neurodegener* **2022**, *17* (1), 11. DOI: 10.1186/s13024-022-00515-1.
- (188) Verde, F.; Silani, V.; Otto, M. Neurochemical biomarkers in amyotrophic lateral sclerosis. *Curr Opin Neurol* **2019**, *32* (5), 747-757. DOI: 10.1097/WCO.0000000000000744.

- (189) Taga, A.; Maragakis, N. J. Current and emerging ALS biomarkers: utility and potential in clinical trials. *Expert Rev Neurother* **2018**, *18* (11), 871-886. DOI: 10.1080/14737175.2018.1530987.
- (190) Koyappayil, A.; Yagati, A. K.; Lee, M. H. Recent Trends in Metal Nanoparticles Decorated 2D Materials for Electrochemical Biomarker Detection. *Biosensors (Basel)* **2023**, *13* (1). DOI: 10.3390/bios13010091.
- (191) Fan, Y.-J.; Hsu, Y.-C.; Gu, B.-C.; Wu, C.-C. Voltammetric measurement of Escherichia coli concentration through p-APG hydrolysis by endogenous β -galactosidase. *Microchem J* **2020**, *154*. DOI: 10.1016/j.microc.2020.104641.
- (192) Lin, C. Y.; Nhat Nguyen, U. T.; Hsieh, H. Y.; Tahara, H.; Chang, Y. S.; Wang, B. Y.; Gu, B. C.; Dai, Y. H.; Wu, C. C.; Tsai, I. J.; et al. Peptide-based electrochemical sensor with nanogold enhancement for detecting rheumatoid arthritis. *Talanta* **2022**, *236*, 122886. DOI: 10.1016/j.talanta.2021.122886.
- (193) Chen, Y. S.; Huang, C. H.; Pai, P. C.; Seo, J.; Lei, K. F. A Review on Microfluidics-Based Impedance Biosensors. *Biosensors (Basel)* **2023**, *13* (1). DOI: 10.3390/bios13010083.
- (194) Sheen, H. J.; Panigrahi, B.; Kuo, T. R.; Hsu, W. C.; Chung, P. S.; Xie, Q. Z.; Lin, C. Y.; Chang, Y. S.; Lin, C. T.; Fan, Y. J. Electrochemical biosensor with electrokinetics-assisted molecular trapping for enhancing C-reactive protein detection. *Biosens Bioelectron* **2022**, *210*, 114338. DOI: 10.1016/j.bios.2022.114338.
- (195) Dutta, P.; Lu, Y. J.; Hsieh, H. Y.; Lee, T. Y.; Lee, Y. T.; Cheng, C. M.; Fan, Y. J. Detection of Candida albicans Using a Manufactured Electrochemical Sensor. *Micromachines (Basel)* **2021**, *12* (2). DOI: 10.3390/mi12020166.

- (196) Wang, M.; Yang, Y.; Min, J.; Song, Y.; Tu, J.; Mukasa, D.; Ye, C.; Xu, C.; Heflin, N.; McCune, J. S.; et al. A wearable electrochemical biosensor for the monitoring of metabolites and nutrients. *Nat Biomed Eng* **2022**, *6* (11), 1225-1235. DOI: 10.1038/s41551-022-00916-z.
- (197) Stevenson, H.; Bacon, A.; Joseph, K. M.; Gwandaru, W. R. W.; Bhide, A.; Sankhala, D.; Dhamu, V. N.; Prasad, S. A Rapid Response Electrochemical Biosensor for Detecting The In Saliva. *Sci Rep* **2019**, *9* (1), 12701. DOI: 10.1038/s41598-019-49185-y.
- (198) Cho, I. H.; Kim, D. H.; Park, S. Electrochemical biosensors: perspective on functional nanomaterials for on-site analysis. *Biomater Res* **2020**, *24*, 6. DOI: 10.1186/s40824-019-0181-y.
- (199) Zhu, C.; Yang, G.; Li, H.; Du, D.; Lin, Y. Electrochemical sensors and biosensors based on nanomaterials and nanostructures. *Anal Chem* **2015**, *87* (1), 230-249. DOI: 10.1021/ac5039863.
- (200) Sethi, J.; Van Bulck, M.; Suhail, A.; Safarzadeh, M.; Perez-Castillo, A.; Pan, G. A label-free biosensor based on graphene and reduced graphene oxide dual-layer for electrochemical determination of beta-amyloid biomarkers. *Microchim Acta* **2020**, *187* (5), 288. DOI: 10.1007/s00604-020-04267-x.
- (201) Pena-Bahamonde, J.; Nguyen, H. N.; Fanourakis, S. K.; Rodrigues, D. F. Recent advances in graphene-based biosensor technology with applications in life sciences. *J Nanobiotechnology* **2018**, *16* (1), 75. DOI: 10.1186/s12951-018-0400-z.
- (202) Ryberg, H.; Bowser, R. Protein biomarkers for amyotrophic lateral sclerosis. *Expert Rev Proteomics* **2008**, *5* (2), 249-262. DOI: 10.1586/14789450.5.2.249.
- (203) Dreger, M.; Steinbach, R.; Otto, M.; Turner, M. R.; Grosskreutz, J. Cerebrospinal fluid biomarkers of disease activity and progression in amyotrophic lateral sclerosis. *J Neurol Neurosurg Psychiatry* **2022**, *93* (4), 422-435. DOI: 10.1136/jnnp-2021-327503.

- (204) Shi, J.; Qin, X.; Chang, X.; Wang, H.; Guo, J.; Zhang, W. Neurofilament markers in serum and cerebrospinal fluid of patients with amyotrophic lateral sclerosis. *J Cell Mol Med* **2022**, *26* (2), 583-587. DOI: 10.1111/jcmm.17100.
- (205) Verde, F.; Steinacker, P.; Weishaupt, J. H.; Kassubek, J.; Oeckl, P.; Halbgebauer, S.; Tumani, H.; von Arnim, C. A. F.; Dorst, J.; Feneberg, E.; et al. Neurofilament light chain in serum for the diagnosis of amyotrophic lateral sclerosis. *J Neurol Neurosurg Psychiatry* **2019**, *90* (2), 157-164. DOI: 10.1136/jnnp-2018-318704.
- (206) Gaiottino, J.; Norgren, N.; Dobson, R.; Topping, J.; Nissim, A.; Malaspina, A.; Bestwick, J. P.; Monsch, A. U.; Regeniter, A.; Lindberg, R. L.; et al. Increased neurofilament light chain blood levels in neurodegenerative neurological diseases. *PLoS One* **2013**, *8* (9), e75091. DOI: 10.1371/journal.pone.0075091.
- (207) Hayat, A.; Barthelmebs, L.; Marty, J.-L. Electrochemical impedimetric immunosensor for the detection of okadaic acid in mussel sample. *Sensors and Actuators B: Chemical* **2012**, *171-172*, 810-815. DOI: 10.1016/j.snb.2012.05.075.
- (208) Eissa, S.; Jimenez, G. C.; Mahvash, F.; Guermoune, A.; Tlili, C.; Szkopek, T.; Zourob, M.; Siaj, M. Functionalized CVD monolayer graphene for label-free impedimetric biosensing. *Nano Research* **2015**, *8* (5), 1698-1709. DOI: 10.1007/s12274-014-0671-0.
- (209) Valverde, A.; Montero-Calle, A.; Barderas, R.; Calero, M.; Yáñez-Sedeño, P.; Campuzano, S.; Pingarrón, J. M. Electrochemical immunoplatfrom to unravel neurodegeneration and Alzheimer's disease through the determination of neurofilament light protein. *Electrochim Acta* **2021**, *371*. DOI: 10.1016/j.electacta.2021.137815.

- (210) Ferapontova, E. E.; Gothelf, K. V. Effect of serum on an RNA aptamer-based electrochemical sensor for theophylline. *Langmuir* **2009**, *25* (8), 4279-4283. DOI: 10.1021/la804309j.
- (211) Verde, F.; Otto, M.; Silani, V. Neurofilament Light Chain as Biomarker for Amyotrophic Lateral Sclerosis and Frontotemporal Dementia. *Front Neurosci* **2021**, *15*, 679199. DOI: 10.3389/fnins.2021.679199.
- (212) Feneberg, E.; Oeckl, P.; Steinacker, P.; Verde, F.; Barro, C.; Van Damme, P.; Gray, E.; Grosskreutz, J.; Jardel, C.; Kuhle, J.; et al. Multicenter evaluation of neurofilaments in early symptom onset amyotrophic lateral sclerosis. *Neurology* **2018**, *90* (1), e22-e30. DOI: 10.1212/WNL.0000000000004761.
- (213) Lee, P. Y.; Osman, J.; Low, T. Y.; Jamal, R. Plasma/serum proteomics: depletion strategies for reducing high-abundance proteins for biomarker discovery. *Bioanalysis* **2019**, *11* (19), 1799-1812. DOI: 10.4155/bio-2019-0145.
- (214) Halbgebauer, S.; Steinacker, P.; Verde, F.; Weishaupt, J.; Oeckl, P.; von Arnim, C.; Dorst, J.; Feneberg, E.; Mayer, B.; Rosenbohm, A.; et al. Comparison of CSF and serum neurofilament light and heavy chain as differential diagnostic biomarkers for ALS. *J Neurol Neurosurg Psychiatry* **2022**, *93* (1), 68-74. DOI: 10.1136/jnnp-2021-327129.
- (215) De Schaepdryver, M.; Lunetta, C.; Tarlarini, C.; Mosca, L.; Chio, A.; Van Damme, P.; Poesen, K. Neurofilament light chain and C reactive protein explored as predictors of survival in amyotrophic lateral sclerosis. *J Neurol Neurosurg Psychiatry* **2020**, *91* (4), 436-437. DOI: 10.1136/jnnp-2019-322309.

- (216) Benatar, M.; Wu, J.; Lombardi, V.; Jeromin, A.; Bowser, R.; Andersen, P. M.; Malaspina, A. Neurofilaments in pre-symptomatic ALS and the impact of genotype. *Amyotroph Lateral Scler Frontotemporal Degener* **2019**, *20* (7-8), 538-548. DOI: 10.1080/21678421.2019.1646769.
- (217) Swindell, W. R.; Kruse, C. P. S.; List, E. O.; Berryman, D. E.; Kopchick, J. J. ALS blood expression profiling identifies new biomarkers, patient subgroups, and evidence for neutrophilia and hypoxia. *J Transl Med* **2019**, *17* (1), 170. DOI: 10.1186/s12967-019-1909-0.
- (218) Breevoort, S.; Gibson, S.; Figueroa, K.; Bromberg, M.; Pulst, S. Expanding Clinical Spectrum of C9ORF72-Related Disorders and Promising Therapeutic Strategies: A Review. *Neurol Genet* **2022**, *8* (3), e670. DOI: 10.1212/NXG.0000000000000670.
- (219) Byrne, S.; Heverin, M.; Elamin, M.; Bede, P.; Lynch, C.; Kenna, K.; MacLaughlin, R.; Walsh, C.; Al Chalabi, A.; Hardiman, O. Aggregation of neurologic and neuropsychiatric disease in amyotrophic lateral sclerosis kindreds: a population-based case-control cohort study of familial and sporadic amyotrophic lateral sclerosis. *Ann Neurol* **2013**, *74* (5), 699-708. DOI: 10.1002/ana.23969.
- (220) Floeter, M. K.; Gendron, T. F. Biomarkers for Amyotrophic Lateral Sclerosis and Frontotemporal Dementia Associated With Hexanucleotide Expansion Mutations in C9orf72. *Front Neurol* **2018**, *9*, 1063. DOI: 10.3389/fneur.2018.01063.
- (221) Hrish, A. P.; Sethuraman, M. Cerebrospinal Fluid (CSF) Analysis and Interpretation in Neurocritical Care for Acute Neurological Conditions. *Indian J Crit Care Med* **2019**, *23* (Suppl 2), S115-S119. DOI: 10.5005/jp-journals-10071-23187.
- (222) Leeman, M.; Choi, J.; Hansson, S.; Storm, M. U.; Nilsson, L. Proteins and antibodies in serum, plasma, and whole blood-size characterization using asymmetrical flow field-flow

fractionation (AF4). *Anal Bioanal Chem* **2018**, *410* (20), 4867-4873. DOI: 10.1007/s00216-018-1127-2.

(223) Cooper-Knock, J.; Hewitt, C.; Highley, J. R.; Brockington, A.; Milano, A.; Man, S.; Martindale, J.; Hartley, J.; Walsh, T.; Gelsthorpe, C.; et al. Clinico-pathological features in amyotrophic lateral sclerosis with expansions in C9ORF72. *Brain* **2012**, *135* (Pt 3), 751-764. DOI: 10.1093/brain/awr365.

(224) Shi, Y.; Hung, S. T.; Rocha, G.; Lin, S.; Linares, G. R.; Staats, K. A.; Seah, C.; Wang, Y.; Chickering, M.; Lai, J.; et al. Identification and therapeutic rescue of autophagosome and glutamate receptor defects in C9ORF72 and sporadic ALS neurons. *JCI Insight* **2019**, *5* (15). DOI: 10.1172/jci.insight.127736.

(225) Lehmer, C.; Oeckl, P.; Weishaupt, J. H.; Volk, A. E.; Diehl-Schmid, J.; Schroeter, M. L.; Lauer, M.; Kornhuber, J.; Levin, J.; Fassbender, K.; et al. Poly-GP in cerebrospinal fluid links C9orf72-associated dipeptide repeat expression to the asymptomatic phase of ALS/FTD. *EMBO Mol Med* **2017**, *9* (7), 859-868. DOI: 10.15252/emmm.201607486.

(226) Bede, P.; Bokde, A. L.; Byrne, S.; Elamin, M.; McLaughlin, R. L.; Kenna, K.; Fagan, A. J.; Pender, N.; Bradley, D. G.; Hardiman, O. Multiparametric MRI study of ALS stratified for the C9orf72 genotype. *Neurology* **2013**, *81* (4), 361-369. DOI: 10.1212/WNL.0b013e31829c5eee.

(227) Agosta, F.; Ferraro, P. M.; Riva, N.; Spinelli, E. G.; Domi, T.; Carrera, P.; Copetti, M.; Falzone, Y.; Ferrari, M.; Lunetta, C.; et al. Structural and functional brain signatures of C9orf72 in motor neuron disease. *Neurobiol Aging* **2017**, *57*, 206-219. DOI: 10.1016/j.neurobiolaging.2017.05.024.

(228) Cistaro, A.; Pagani, M.; Montuschi, A.; Calvo, A.; Moglia, C.; Canosa, A.; Restagno, G.; Brunetti, M.; Traynor, B. J.; Nobili, F.; et al. The metabolic signature of C9ORF72-related ALS:

FDG PET comparison with nonmutated patients. *Eur J Nucl Med Mol Imaging* **2014**, *41* (5), 844-852. DOI: 10.1007/s00259-013-2667-5.

(229) Lim, R. R. X.; Bonanni, A. The potential of electrochemistry for the detection of coronavirus-induced infections. *Trends Analyt Chem* **2020**, *133*, 116081. DOI: 10.1016/j.trac.2020.116081.

(230) Peteni, S.; Ozoemena, O. C.; Khawula, T.; Haruna, A. B.; Rawson, F. J.; Shai, L. J.; Ola, O.; Ozoemena, K. I. Electrochemical Immunosensor for Ultra-Low Detection of Human Papillomavirus Biomarker for Cervical Cancer. *ACS Sens* **2023**, *8* (7), 2761-2770. DOI: 10.1021/acssensors.3c00677.

(231) Campuzano, S.; Pedrero, M.; Yáñez-Sedeño, P.; Pingarrón, J. M. New challenges in point of care electrochemical detection of clinical biomarkers. *Sensors and Actuators B: Chemical* **2021**, *345*. DOI: 10.1016/j.snb.2021.130349.

(232) Das, P. K.; Adil, O.; Shamsi, M. H. First multiplexed electrochemical wax-on-plastic chip: PNA/GO interface integration for DNA detection. *Journal of Micromechanics and Microengineering* **2023**, *33* (9). DOI: 10.1088/1361-6439/ace6b1.

(233) Zribi, B.; Castro-Arias, J. M.; Decanini, D.; Gogneau, N.; Dragoe, D.; Cattoni, A.; Ouerghi, A.; Korri-Youssoufi, H.; Haghiri-Gosnet, A. M. Large area graphene nanomesh: an artificial platform for edge-electrochemical biosensing at the sub-attomolar level. *Nanoscale* **2016**, *8* (34), 15479-15485. DOI: 10.1039/c6nr04289a.

(234) Asefifeyzabadi, N.; Alkhaldi, R.; Qamar, A. Z.; Pater, A. A.; Patwardhan, M.; Gagnon, K. T.; Talapatra, S.; Shamsi, M. H. Label-free Electrochemical Detection of CGG Repeats on Inkjet Printable 2D Layers of MoS₂. *ACS Appl Mater Interfaces* **2020**, *12* (46), 52156-52165. DOI: 10.1021/acsaami.0c14912.

- (235) Asefifeyzabadi, N.; Holland, T. E.; Sivakumar, P.; Talapatra, S.; Senanayake, I. M.; Goodson, B. M.; Shamsi, M. H. Sequence-Independent DNA Adsorption on Few-Layered Oxygen-Functionalized Graphene Electrodes: An Electrochemical Study for Biosensing Application. *Biosensors (Basel)* **2021**, *11* (8). DOI: 10.3390/bios11080273.
- (236) Ye, R.; James, D. K.; Tour, J. M. Laser-Induced Graphene: From Discovery to Translation. *Adv Mater* **2019**, *31* (1), e1803621. DOI: 10.1002/adma.201803621.
- (237) Zhu, J.; Huang, X.; Song, W. Physical and Chemical Sensors on the Basis of Laser-Induced Graphene: Mechanisms, Applications, and Perspectives. *ACS Nano* **2021**, *15* (12), 18708-18741. DOI: 10.1021/acsnano.1c05806.
- (238) Huang, L.; Su, J.; Song, Y.; Ye, R. Laser-Induced Graphene: En Route to Smart Sensing. *Nanomicro Lett* **2020**, *12* (1), 157. DOI: 10.1007/s40820-020-00496-0.
- (239) Honda, H.; Kusaka, Y.; Wu, H.; Endo, H.; Tsuya, D.; Ohnuki, H. Toward a Practical Impedimetric Biosensor: A Micro-Gap Parallel Plate Electrode Structure That Suppresses Unexpected Device-to-Device Variations. *ACS Omega* **2022**, *7* (13), 11017-11022. DOI: 10.1021/acsomega.1c06942.
- (240) Chmayssem, A.; Tanase, C. E.; Verplanck, N.; Gougis, M.; Mourier, V.; Zebda, A.; Ghaemmaghami, A. M.; Mailley, P. New Microfluidic System for Electrochemical Impedance Spectroscopy Assessment of Cell Culture Performance: Design and Development of New Electrode Material. *Biosensors (Basel)* **2022**, *12* (7). DOI: 10.3390/bios12070452.
- (241) Velasco, A.; Ryu, Y. K.; Hamada, A.; de Andres, A.; Calle, F.; Martinez, J. Laser-Induced Graphene Microsupercapacitors: Structure, Quality, and Performance. *Nanomaterials (Basel)* **2023**, *13* (5). DOI: 10.3390/nano13050788.

- (242) Lamberti, A.; Perrucci, F.; Caprioli, M.; Serrapede, M.; Fontana, M.; Bianco, S.; Ferrero, S.; Tresso, E. New insights on laser-induced graphene electrodes for flexible supercapacitors: tunable morphology and physical properties. *Nanotechnology* **2017**, *28* (17), 174002. DOI: 10.1088/1361-6528/aa6615.
- (243) Lin, J.; Peng, Z.; Liu, Y.; Ruiz-Zepeda, F.; Ye, R.; Samuel, E. L.; Yacaman, M. J.; Yakobson, B. I.; Tour, J. M. Laser-induced porous graphene films from commercial polymers. *Nat Commun* **2014**, *5*, 5714. DOI: 10.1038/ncomms6714.
- (244) Han, T.; Nag, A.; Simorangkir, R.; Afsarimanesh, N.; Liu, H.; Mukhopadhyay, S. C.; Xu, Y.; Zhadobov, M.; Sauleau, R. Multifunctional Flexible Sensor Based on Laser-Induced Graphene. *Sensors (Basel)* **2019**, *19* (16). DOI: 10.3390/s19163477.
- (245) Vicentic, T.; Rasljic Rafajilovic, M.; Ilic, S. D.; Koteska, B.; Madevska Bogdanova, A.; Pasti, I. A.; Lehocki, F.; Spasenovic, M. Laser-Induced Graphene for Heartbeat Monitoring with HeartPy Analysis. *Sensors (Basel)* **2022**, *22* (17). DOI: 10.3390/s22176326.
- (246) Soares, R. R. A.; Hjort, R. G.; Pola, C. C.; Parate, K.; Reis, E. L.; Soares, N. F. F.; McLamore, E. S.; Claussen, J. C.; Gomes, C. L. Laser-Induced Graphene Electrochemical Immunosensors for Rapid and Label-Free Monitoring of *Salmonella enterica* in Chicken Broth. *ACS Sens* **2020**, *5* (7), 1900-1911. DOI: 10.1021/acssensors.9b02345.
- (247) Wang, G.; Chen, J.; Huang, L.; Chen, Y.; Li, Y. A laser-induced graphene electrochemical immunosensor for label-free CEA monitoring in serum. *Analyst* **2021**, *146* (21), 6631-6642. DOI: 10.1039/d1an01011e.
- (248) Beduk, T.; Beduk, D.; de Oliveira Filho, J. I.; Zihnioglu, F.; Cicek, C.; Serto, R.; Arda, B.; Goksel, T.; Turhan, K.; Salama, K. N.; et al. Rapid Point-of-Care COVID-19 Diagnosis with a

Gold-Nanoarchitecture-Assisted Laser-Scribed Graphene Biosensor. *Anal Chem* **2021**, *93* (24), 8585-8594. DOI: 10.1021/acs.analchem.1c01444.

(249) Fenzl, C.; Nayak, P.; Hirsch, T.; Wolfbeis, O. S.; Alshareef, H. N.; Baeumner, A. J. Laser-Scribed Graphene Electrodes for Aptamer-Based Biosensing. *ACS Sens* **2017**, *2* (5), 616-620. DOI: 10.1021/acssensors.7b00066.

(250) Barman, S. C.; Zahed, M. A.; Sharifuzzaman, M.; Ko, S. G.; Yoon, H.; Nah, J. S.; Xuan, X.; Park, J. Y. A Polyallylamine Anchored Amine-Rich Laser-Ablated Graphene Platform for Facile and Highly Selective Electrochemical IgG Biomarker Detection. *Advanced Functional Materials* **2020**, *30* (14). DOI: 10.1002/adfm.201907297.

(251) Gooding, J. J. Advances in Interfacial Design for Electrochemical Biosensors and Sensors: Aryl Diazonium Salts for Modifying Carbon and Metal Electrodes. *Electroanalysis* **2008**, *20* (6), 573-582. DOI: 10.1002/elan.200704124.

(252) Fortgang, P.; Tite, T.; Barnier, V.; Zehani, N.; Maddi, C.; Lagarde, F.; Loir, A. S.; Jaffrezic-Renault, N.; Donnet, C.; Garrelie, F.; et al. Robust Electrografting on Self-Organized 3D Graphene Electrodes. *ACS Appl Mater Interfaces* **2016**, *8* (2), 1424-1433. DOI: 10.1021/acsami.5b10647.

(253) Adil, O.; Shamsi, M. H. Electrochemical Impedance Immunoassay for ALS-Associated Neurofilament Protein: Matrix Effect on the Immunoplatfrom. *Biosensors* **2023**, *13* (2), 247.

(254) Yanez-Sedeno, P.; Campuzano, S.; Pingarron, J. M. Integrated Affinity Biosensing Platforms on Screen-Printed Electrodes Electrografted with Diazonium Salts. *Sensors (Basel)* **2018**, *18* (2). DOI: 10.3390/s18020675.

- (255) Jiang, C.; Wang, G.; Hein, R.; Liu, N.; Luo, X.; Davis, J. J. Antifouling Strategies for Selective In Vitro and In Vivo Sensing. *Chem Rev* **2020**, *120* (8), 3852-3889. DOI: 10.1021/acs.chemrev.9b00739.
- (256) Lamberti, A.; Clerici, F.; Fontana, M.; Scaltrito, L. A Highly Stretchable Supercapacitor Using Laser-Induced Graphene Electrodes onto Elastomeric Substrate. *Advanced Energy Materials* **2016**, *6* (10). DOI: 10.1002/aenm.201600050.
- (257) Macedo, L. J. A.; Lima, F.; Amorim, R. G.; Freitas, R. O.; Yadav, A.; Iost, R. M.; Balasubramanian, K.; Crespilho, F. N. Interplay of non-uniform charge distribution on the electrochemical modification of graphene. *Nanoscale* **2018**, *10* (31), 15048-15057. DOI: 10.1039/c8nr03893g.
- (258) Schmitz, A.; Pinheiro Marques, J.; Oertig, I.; Maharjan, N.; Saxena, S. Emerging Perspectives on Dipeptide Repeat Proteins in C9ORF72 ALS/FTD. *Front Cell Neurosci* **2021**, *15*, 637548. DOI: 10.3389/fncel.2021.637548.
- (259) Xu, M.; Luo, X.; Davis, J. J. The label free picomolar detection of insulin in blood serum. *Biosens Bioelectron* **2013**, *39* (1), 21-25. DOI: 10.1016/j.bios.2012.06.014.
- (260) Chen, Y.; Li, Y.; Sun, D.; Tian, D.; Zhang, J.; Zhu, J.-J. Fabrication of gold nanoparticles on bilayer graphene for glucose electrochemical biosensing. *Journal of Materials Chemistry* **2011**, *21* (21). DOI: 10.1039/c1jm10293a.

APPENDIX A

FIGURE PERMISSIONS

License Details

This Agreement between southern illinois university carbondale – omair adil ("You") and Springer Nature ("Springer Nature") consists of your license details and the terms and conditions provided by Springer Nature and Copyright Clearance Center.

[Print](#) [Copy](#)

License Number	5766290541599
License date	Apr 12, 2024
Licensed Content Publisher	Springer Nature
Licensed Content Publication	Springer eBook
Licensed Content Title	Transducers in Biosensors
Licensed Content Author	Sandeep Yadav, Ashok Saini, Rooma Devi et al
Licensed Content Date	Jan 1, 2023
Type of Use	Thesis/Dissertation
Requestor type	non-commercial (non-profit)
Format	print and electronic
Portion	figures/tables/illustrations
Number of figures/tables/illustrations	1
Will you be translating?	no
Circulation/distribution	1 - 29
Author of this Springer Nature content	no
Title of new work	NEW ELECTROCHEMICAL PLATFORMS FOR THE DETECTION OF NEURODEGENERATIVE DISEASE BIOMARKERS
Institution name	southern illinois university, Carbondale
Expected presentation date	May 2024
Portions	1
Requestor Location	southern illinois university carbondale Neckers Building, 1245 Lincoln Dr #4409
	CARBONDALE, IL 62901 United States Attn: southern illinois university carbondale
Total	0.00 USD

Permission for Figure 1.1. Adapted from 1 with the permission from Springer Nature.

License Details

This Agreement between southern illinois university carbondale -- omair adil ("You") and Elsevier ("Elsevier") consists of your license details and the terms and conditions provided by Elsevier and Copyright Clearance Center.

Print Copy

License Number	5766300118296
License date	Apr 12, 2024
Licensed Content Publisher	Elsevier
Licensed Content Publication	Talanta
Licensed Content Title	A novel classification of prostate specific antigen (PSA) biosensors based on transducing elements
Licensed Content Author	Mansoor Ani Najeeb,Zubair Ahmad,R.A. Shakoor,A.M.A. Mohamed,Ramazan Kahraman
Licensed Content Date	Jun 1, 2017
Licensed Content Volume	168
Licensed Content Issue	n/a
Licensed Content Pages	10
Type of Use	reuse in a thesis/dissertation
Portion	figures/tables/illustrations
Number of figures/tables/illustrations	1
Format	both print and electronic
Are you the author of this Elsevier article?	No
Will you be translating?	No
Title of new work	NEW ELECTROCHEMICAL PLATFORMS FOR THE DETECTION OF NEURODEGENERATIVE DISEASE BIOMARKERS
Institution name	southern Illinois university, Carbondale
Expected presentation date	May 2024
Portions	1
Requestor Location	southern illinois university carbondale Neckers Building, 1245 Lincoln Dr #4409 CARBONDALE, IL 62901 United States Attn: southern illinois university carbondale
Publisher Tax ID	98-0397604
Total	0.00 USD

Permission for Figure 1.2. Adapted from 6 with the permission from Talanta.



CC BY 4.0 DEED

Attribution 4.0 International

Canonical URL : <https://creativecommons.org/licenses/by/4.0/>

[See the legal code](#)

You are free to:

Share — copy and redistribute the material in any medium or format for any purpose, even commercially.

Adapt — remix, transform, and build upon the material for any purpose, even commercially.

The licensor cannot revoke these freedoms as long as you follow the license terms.

Under the following terms:

 **Attribution** — You must give [appropriate credit](#), provide a link to the license, and [indicate if changes were made](#). You may do so in any reasonable manner, but not in any way that suggests the licensor endorses you or your use.

No additional restrictions — You may not apply legal terms or [technological measures](#) that legally restrict others from doing anything the license permits.

Permission for Figure 1.3. Adapted from 2 with the Creative Commons Attribution (CC BY 4.0 DEED) from Biosensors.

License Details

This Agreement between southern illinois university carbondale -- omair adil ("You") and Springer Nature ("Springer Nature") consists of your license details and the terms and conditions provided by Springer Nature and Copyright Clearance Center.

[Print](#) [Copy](#)

License Number	5766310974150
License date	Apr 12, 2024
Licensed Content Publisher	Springer Nature
Licensed Content Publication	Microchimica Acta
Licensed Content Title	A review on recent advancements in electrochemical biosensing using carbonaceous nanomaterials
Licensed Content Author	Alireza Sanati et al
Licensed Content Date	Nov 13, 2019
Type of Use	Thesis/Dissertation
Requestor type	non-commercial (non-profit)
Format	print and electronic
Portion	figures/tables/illustrations
Number of figures/tables/illustrations	1
Will you be translating?	no
Circulation/distribution	1 - 29
Author of this Springer Nature content	no
Title of new work	NEW ELECTROCHEMICAL PLATFORMS FOR THE DETECTION OF NEURODEGENERATIVE DISEASE BIOMARKERS
Institution name	southern illinois university, Carbondale
Expected presentation date	May 2024
Portions	figure 4
Requestor Location	southern illinois university carbondale Neckers Building, 1245 Lincoln Dr #4409
	CARBONDALE, IL 62901 United States Attn: southern illinois university carbondale
Total	0.00 USD

Permission for Figure 1.4 A and B. Adapted from 6 with the permission from Microchimica Acta.



CC BY 3.0 DEED

Attribution 3.0 Unported

Notice

This is an older version of this license. Compared to previous versions, the 4.0 versions of all CC licenses are [more user-friendly and more internationally robust](#). If you are [licensing your own work](#), we strongly recommend the use of the 4.0 license instead: [CC BY 4.0 Deed](#) | [Attribution 4.0 International](#)

Canonical URL : <https://creativecommons.org/licenses/by/3.0/>

[See the legal code](#)

You are free to:

Share — copy and redistribute the material in any medium or format for any purpose, even commercially.

Adapt — remix, transform, and build upon the material for any purpose, even commercially.

The licensor cannot revoke these freedoms as long as you follow the license terms.

Under the following terms:

 **Attribution** — You must give [appropriate credit](#), provide a link to the license, and [indicate if changes were made](#). You may do so in any reasonable manner, but not in any way that suggests the licensor endorses you or your use.

No additional restrictions — You may not apply legal terms or [technological measures](#) that legally restrict others from doing anything the license permits.

Permission for Figure 1.4 C. Adapted from 4812 with the Creative Commons Attribution (CC BY 3.0 DEED) from Sensors.

License Details

This Agreement between southern illinois university carbondale -- omar adil ("You") and Springer Nature ("Springer Nature") consists of your license details and the terms and conditions provided by Springer Nature and Copyright Clearance Center.

Print

Copy

License Number	5766560822527
License date	Apr 12, 2024
Licensed Content Publisher	Springer Nature
Licensed Content Publication	Applied Physics A: Materials Science & Processing
Licensed Content Title	Non-enzymatic glucose detection based on cuprous oxide thin film synthesized via electrochemical deposition
Licensed Content Author	Samih Laidoudi et al
Licensed Content Date	Feb 3, 2021
Type of Use	Thesis/Dissertation
Requestor type	non-commercial (non-profit)
Format	print and electronic
Portion	figures/tables/illustrations
Number of figures/tables/illustrations	1
Will you be translating?	no
Circulation/distribution	1 - 29
Author of this Springer Nature content	no
Title of new work	NEW ELECTROCHEMICAL PLATFORMS FOR THE DETECTION OF NEURODEGENERATIVE DISEASE BIOMARKERS
Institution name	southern illinois university, Carbondale
Expected presentation date	May 2024
Portions	scheme 1
Requestor Location	southern illinois university carbondale Neckers Building, 1245 Lincoln Dr #4409 CARBONDALE, IL 62901 United States Attn: southern illinois university carbondale
Total	0.00 USD

Permission for Figure 1.4 D. Adapted from 6 with the permission from Applied Physics A.



CC BY 4.0 DEED

Attribution 4.0 International

Canonical URL: <https://creativecommons.org/licenses/by/4.0/>

[See the legal code](#)

You are free to:

Share — copy and redistribute the material in any medium or format for any purpose, even commercially.

Adapt — remix, transform, and build upon the material for any purpose, even commercially.

The licensor cannot revoke these freedoms as long as you follow the license terms.

Under the following terms:

 **Attribution** — You must give [appropriate credit](#), provide a link to the license, and [indicate if changes were made](#). You may do so in any reasonable manner, but not in any way that suggests the licensor endorses you or your use.

No additional restrictions — You may not apply legal terms or [technological measures](#) that legally restrict others from doing anything the license permits.

Notices:

You do not have to comply with the license for elements of the material in the public domain or where your use is permitted by an applicable [exception or limitation](#).

No warranties are given. The license may not give you all of the permissions necessary for your intended use. For example, other rights such as [publicity, privacy, or moral rights](#) may limit how you use the material.

Permission for Figure 1.4 E and F. Adapted from 2 with the Creative Commons Attribution (CC BY 4.0 DEED) from Sensors.



CC BY 4.0 DEED

Attribution 4.0 International

Canonical URL: <https://creativecommons.org/licenses/by/4.0/>

[See the legal code](#)

You are free to:

Share — copy and redistribute the material in any medium or format for any purpose, even commercially.

Adapt — remix, transform, and build upon the material for any purpose, even commercially.

The licensor cannot revoke these freedoms as long as you follow the license terms.

Under the following terms:



Attribution — You must give [appropriate credit](#), provide a link to the license, and [indicate if changes were made](#). You may do so in any reasonable manner, but not in any way that suggests the licensor endorses you or your use.

No additional restrictions — You may not apply legal terms or [technological measures](#) that legally restrict others from doing anything the license permits.

Notices:

You do not have to comply with the license for elements of the material in the public domain or where your use is permitted by an applicable [exception or limitation](#).

No warranties are given. The license may not give you all of the permissions necessary for your intended use. For example, other rights such as [publicity, privacy, or moral rights](#) may limit how you use the material.

Permission for Figure 1.5. Adapted from 167 with the Creative Commons Attribution (CC BY 4.0 DEED) from Journal of The Electrochemical Society.



CC BY 4.0 DEED

Attribution 4.0 International

Canonical URL: <https://creativecommons.org/licenses/by/4.0/>

[See the legal code](#)

You are free to:

Share — copy and redistribute the material in any medium or format for any purpose, even commercially.

Adapt — remix, transform, and build upon the material for any purpose, even commercially.

The licensor cannot revoke these freedoms as long as you follow the license terms.

Under the following terms:

 **Attribution** — You must give appropriate credit, provide a link to the license, and indicate if changes were made. You may do so in any reasonable manner, but not in any way that suggests the licensor endorses you or your use.

No additional restrictions — You may not apply legal terms or technological measures that legally restrict others from doing anything the license permits.

Notices:

You do not have to comply with the license for elements of the material in the public domain or where your use is permitted by an applicable exception or limitation.

No warranties are given. The license may not give you all of the permissions necessary for your intended use. For example, other rights such as publicity, privacy, or moral rights may limit how you use the material.

Permission for Figure 1.7. Adapted from 4 with the Creative Commons Attribution (CC BY 4.0 DEED) from Molecular Neurodegeneration.

C9orf72 loss-of-function: a trivial, stand-alone or additive mechanism in C9 ALS/FTD?

Author: Elke Braems et al

Publication: Acta Neuropathologica

SPRINGER NATURE

Publisher: Springer Nature

Date: Sep 2, 2020

Copyright © 2020, The Author(s)

Creative Commons

This is an open access article distributed under the terms of the [Creative Commons CC BY](#) license, which permits unrestricted use, distribution, and reproduction in any medium, provided the original work is properly cited.

You are not required to obtain permission to reuse this article.

To request permission for a type of use not listed, please contact Springer Nature

Permission for Figure 1.8. Adopted from Creative Commons Attribution (CC DEED) from Acta Neuropathologica.

This is a License Agreement between omair adil, southern illinois university carbondale ("User") and Copyright Clearance Center, Inc. ("CCC") on behalf of the Rightsholder identified in the order details below. The license consists of the order details, the Marketplace Permissions General Terms and Conditions below, and any Rightsholder Terms and Conditions which are included below.

All payments must be made in full to CCC in accordance with the Marketplace Permissions General Terms and Conditions below.

Order Date	12-Apr-2024	Type of Use	Republish in a thesis/dissertation
Order License ID	1472815-1	Publisher	AMERICAN SOCIETY FOR MICROBIOLOGY,
ISSN	0893-8512	Portion	Image/photo/illustration

LICENSED CONTENT

Publication Title	Clinical microbiology reviews	Publication Type	Journal
Article Title	Biosensors for whole-cell bacterial detection.	Start Page	631
Author/Editor	AMERICAN SOCIETY FOR MICROBIOLOGY.	End Page	646
Date	01/01/1988	Issue	3
Language	English	Volume	27
Country	United States of America	URL	https://journals.asm.org/journal/cmr
Rightsholder	American Society for Microbiology - Journals		

REQUEST DETAILS

Portion Type	Image/photo/illustration	Distribution	Worldwide
Number of Images / Photos / Illustrations	1	Translation	Original language of publication
Format (select all that apply)	Print, Electronic	Copies for the Disabled?	No
Who Will Republish the Content?	Not-for-profit entity	Minor Editing Privileges?	No
Duration of Use	Current edition and up to 5 years	Incidental Promotional Use?	No
Lifetime Unit Quantity	Up to 499	Currency	USD
Rights Requested	Main product		

NEW WORK DETAILS

Title	NEW ELECTROCHEMICAL PLATFORMS FOR THE DETECTION OF NEURODEGENERATIVE DISEASE BIOMARKERS	Institution Name	southern illinois university carbondale
Instructor Name	omair adil	Expected Presentation Date	2024-05-11

Permission for Figure 1.9. Adapted from 638 with the permission from Clinical Microbiology Reviews.

VITA

Graduate School

Southern Illinois University Carbondale

Omaisr Adil

omair.adil@siu.edu, omairadilchem@gmail.com

Federal Urdu University of Arts, Sciences and Technology, Karachi, Pakistan

Master of Science (undergrad), Chemistry, December 2010

National University of Science and Technology, Islamabad, Pakistan

Master of Science, Chemistry, September 2017

Special Honors and Awards:

1. Dissertation Research Award, 2023-2024
2. Graduate and Professional Student Council (GPSC) Travel Award for PITTCON Spring, San Diego, 2024
3. Graduate Student Professional Development Monetary Support for PITTCON Spring, San Diego, 2024
4. Southern Illinois ACS Local Section Travel Support for PITTCON Spring, San Diego, 2024
5. Gower's Summer Research Fellowship, 2023
6. Graduate and Professional Student Council (GPSC) Student Creative Activity and Research Funding Award 2023
7. Gold Medal, First Position in M.Sc. (undergrad) Department of Chemistry, Federal Urdu University of Arts, Science and Technology, Karachi, Pakistan. 2010

Dissertation Paper Title:

New Electrochemical Platforms for the Detection of Neurodegenerative Disease Biomarkers

Major Professor: Dr. Mohtashim Hassan Shamsi

Publications:

1. Das, P.; **Adil, O.**; DeGregorio, A.; Sumita, M.; Shamsi, M., Pseudouridine-modified RNA probe for label-free electrochemical detection of nucleic acids on 2D MoS₂ nanosheets. *Analyst*, **2024**. (<https://doi.org/10.1039/D3AN01832F>)
2. Das, P.; **Adil, O.**; Shamsi, M., First multiplexed electrochemical wax-on-plastic chip: PNA/GO interface integration for DNA detection. IOP Science, Journal of Micromechanics and Microengineering, **2023**.(<https://doi.org/10.1149/1945-7111/ab8ce0>)
3. **Adil, O.**; Eddington, S.; Gagnon, K., Shamsi, M., Microprobes for Label-Free Detection of Neurodegenerative Genetic Repeats: Can Probe Backbone Alleviate Secondary Structure Effects and Discriminate Tandem from Sporadic Repeats? *ACS, Analytical Chemistry*. **2023**.([10.1021/acs.analchem.3c01886](https://doi.org/10.1021/acs.analchem.3c01886))
4. **Adil, O.**; and Shamsi, M., Electrochemical Impedance Immunoassay for ALS-associated Neurofilament Protein: Matrix Effect on the Immunoplatfrom. *Biosensors*. **2023**, *13*(2), 247. (<https://doi.org/10.3390/bios13020247>)
5. Giang, H.; **Adil, O.**; and Suni, I., Electrodeposition of Ni-doped MoS₂ Thin Films. *Journal of The Electrochemical Society* **2020**, *167*(08), 082512. (<https://doi.org/10.1149/1945-7111/ab8ce0>)